

DEPARTMENT OF PHYSICS  
UNIVERSITY OF JYVÄSKYLÄ  
RESEARCH REPORT No. 15/2009

**ELECTRONIC, STRUCTURAL AND CHEMICAL PROPERTIES OF  
GOLD CLUSTERS ON ULTRA-THIN OXIDE FILMS**

**BY  
PENTTI FRONDELIUS**

Academic Dissertation  
for the Degree of  
Doctor of Philosophy

*To be presented, by permission of the  
Faculty of Mathematics and Natural Sciences  
of the University of Jyväskylä,  
for public examination in Auditorium FYS-1 of the  
University of Jyväskylä on December 19, 2009  
at 12 o'clock noon*



Jyväskylä, Finland  
December 2009



# Preface

This work has been done at the Nanoscience Center (NSC) of the University of Jyväskylä during the years 2006-2009.

I would like to thank my supervisors Dr. Karoliina Honkala and professor Hannu Häkkinen, for invaluable guidance and collaboration during the past four years. I also would like to thank Dr. Michael Walter for inspiring collaboration. Furthermore, I have had good time working with Dr. Henrik Grönbeck and Dr. Anders Hellman from the Competence Centre for Catalysis and Department of Applied Physics in the Chalmers Technical University, Gothenburg, Sweden. I'm also grateful for Dr. Xiao Lin, Dr. Niklas Nilius and professor H. J. Freund from the Department of Chemical Physics in Fritz-Haber-Institut der Max-Planck-Gesellschaft in Berlin, Germany, for collaboration and carrying out outstanding scanning tunneling microscopy experiments. I have also had fruitful discussions, related to research, and to science in general, with professor Matti Manninen, professor Robert van Leeuwen, Dr. Pekka Koskinen and MSc. Jenni Andersin. Dr. Vesa Apaja has been always available for helping with computer related technical problems.

I acknowledge the Academy of Finland for the financial support through the project 118532, the Finnish IT Center for Science (CSC) and the NSC for the computational resources in the super computers Sepeli, Murska, Louhi and Joker. I also acknowledge the Vilho, Yrjö and Kalle Väisälä foundation for funding my two week course trip to Technical University of Denmark (DTU). I'm also grateful for COST (European Cooperation in the field of Scientific and Technical Research) for providing me a possibility to take part in excellent scientist meetings in Germany, France and Sweden.

Finally, I want to thank my lovely wife Anna, my parents Erkki and Kaarina, my parents-in-law, Osmo and Erja and brother-in-law, Olli, and all my friends and colleagues for supporting me during this work.

Jyväskylä, December 2009

Pentti Frondelius



# Abstract

Two decades ago, it was found that gold is catalytically active as clusters although it is known to be inert as bulk material. In the work presented in this thesis, density functional theory calculations have been applied to show that the properties of gold clusters and small molecules, namely  $O_2$  and  $NO_2$ , are different on oxide thin films supported by metal carriers than on single crystal oxide surfaces. Collectively, these differences are called thin-film effects. The effects and the mechanisms behind them have been studied with atomistic calculations and rationalized with simple physical models. The significance of the thin-film effects for heterogeneous catalysis is discussed.

It has been found that on MgO/Mo thin film, the adsorption of gold clusters is strong, whereas on single crystal MgO, the adsorption is weak. On MgO/Mo and MgO/Ag, the clusters are charged and tend to maximize their surface contact whereas on single crystal MgO, they are essentially neutral and the smallest clusters have only few atoms in contact with the surface. As the clusters are charged, their adsorption energy correlates to the electron affinity of gas-phase clusters. The tiniest  $Au_{2-6}$  favor chain-like structures on MgO/Mo. The larger clusters of around 7-20 atoms are two dimensional and planar on MgO/Ag. These structures are not favored by the clusters adsorbed on single crystal MgO. Furthermore, also  $O_2$  and  $NO_2$  become charged on the studied thin-films.

In addition to electron affinity of the adsorbate, the strength of the thin-film effects seem to depend on oxide film thickness and the work function of the substrate. The long-ranged character of the effect can be addressed to image charge and polarization interaction. It has been predicted that the thin-film effects are significant when the film thickness is less than 1-2 nm.

The electronic states of the chain and planar clusters can be rationalized in the light of one or two dimensional harmonic oscillator model depending on the cluster size. Effectively, a cluster can be seen as a harmonic potential to which the 6s valence electrons of gold atoms and the charge transferred from the substrate are confined. By applying these ideas, it has been possible to identify experimentally observed clusters in a combined scanning tunneling microscopy and density functional theory study. This is an important step in characterizing thin-film based cluster catalytic model systems.

Calculations of  $O_2$  adsorption on  $Au_{1-6}$ /MgO/Mo show that  $O_2$  tends to stick at the ends of the chains. However, adsorption to bare MgO/Mo terrace is slightly more favorable. Based on these results, one can suggest a CO oxidation scheme in which Au traps CO molecules whereas  $O_2$  sticks on the terraces. As the surface diffusion barrier of  $O_2$  is low, the molecules occasionally reach Au clusters with CO and the  $CO_2$  is released on the cluster boundary. It should be noted, however, that also other

reaction pathways can be possible and they may depend on the carrier metal and the cluster size.

<b>Author's address</b>	Pentti Frondelius Department of Physics University of Jyväskylä Finland
<b>Supervisors</b>	Docent Karoliina Honkala Department of Chemistry University of Jyväskylä Finland  Professor Hannu Häkkinen Departments of Physics and Chemistry University of Jyväskylä Finland
<b>Reviewers</b>	Professor Matti Alatalo Department of Mathematics and Physics Lappeenranta University of Technology Finland  Doctor Sami Paavilainen Department of Physics Tampere University of Technology Finland
<b>Opponent</b>	Doctor Núria López Institute of Chemical Research of Catalonia (ICIQ) Tarragona Spain





# List of publications

- I P. Frondelius, H. Häkkinen and K. Honkala. *Adsorption of small Au clusters on MgO and MgO/Mo: the role of oxygen vacancies and the Mo-support*. New J. Phys. **9**, 339 (2007).
- II P. Frondelius, H. Häkkinen and K. Honkala. *Adsorption of gold clusters on metal-supported MgO: Correlation to electron affinity of gold*. Phys. Rev. B **76**, 073406 (2007).
- III M. Walter, P. Frondelius, K. Honkala and H. Häkkinen. *Electronic structure of MgO-Supported Au clusters: Quantum dots probed by scanning tunneling microscopy*. Phys. Rev. Lett. **99**, 096102 (2007).
- IV P. Frondelius, A. Hellman, K. Honkala, H. Häkkinen and H. Grönbeck. *Charging of atoms, clusters and molecules on metal supported oxides: a general and long-ranged phenomenon*. Phys. Rev. B **78**, 085426 (2008).
- V X. Lin, N. Nilius, H.-J. Freund, M. Walter, P. Frondelius, K. Honkala and H. Häkkinen. *Quantum well states in two-dimensional gold clusters on MgO thin films*. Phys. Rev. Lett. **102**, 206801 (2009).
- VI P. Frondelius, H. Häkkinen and K. Honkala. *Adsorption and activation of O<sub>2</sub> at Au chains on MgO/Mo thin films*. Phys. Chem. Chem. Phys., DOI:10.1039/B917723J (2010).

The author has done all the numerical work in the publications I, II and VI, and part of it in III, IV and V by using the density functional theory codes Dacapo and GPAW. He has written the first drafts of I, II and VI and participated actively in the writing of IV and V. The author has written the scanning tunneling microscopy simulation code used with the Dacapo calculations in III and the scanning tunneling spectroscopy code used with the GPAW calculations in V. Furthermore, the author has contributed to the paper J. S. Hummelshøj *et al.*, *DFT based screening of ternary alkali-transition metal borohydrides - a computational materials design project* J. Chem. Phys. **131**, 014101 (2009), which is excluded from the thesis.



# Contents

<b>1</b>	<b>Introduction</b>	<b>3</b>
1.1	Metal clusters . . . . .	3
1.2	Gold, gold clusters and catalysis . . . . .	4
1.3	Thin films and thin-film supported adsorbates . . . . .	5
1.4	The Nobel prize methods: DFT and STM . . . . .	7
1.5	About this thesis . . . . .	8
<b>2</b>	<b>Density functional theory</b>	<b>11</b>
2.1	The many-body Hamiltonian of interacting electrons and nuclei . . . . .	11
2.2	The Born-Oppenheimer approximation . . . . .	12
2.3	The Hohenberg-Kohn theorems . . . . .	13
2.4	The Kohn-Sham ansatz . . . . .	15
2.5	The exchange and correlation energies . . . . .	19
2.6	The local density approximation . . . . .	21
2.7	Gradient expansion approximations . . . . .	21
<b>3</b>	<b>Issues in practical implementations of density functional theory</b>	<b>27</b>
3.1	Periodic systems . . . . .	27
3.2	Basis sets and grids . . . . .	28
3.2.1	Plane-wave basis . . . . .	29
3.2.2	Real space grids . . . . .	30
3.3	Towards smoother valence states . . . . .	32
3.3.1	Pseudopotentials . . . . .	32
3.3.2	Projector augmented wave method . . . . .	35
<b>4</b>	<b>The methods of analysis</b>	<b>39</b>
4.1	Changes in the total energy . . . . .	39
4.2	Density difference due to adsorption . . . . .	41
4.3	Bader charge analysis . . . . .	41
4.4	Kohn-Sham states and their density . . . . .	42
<b>5</b>	<b>Simulating STM</b>	<b>45</b>
5.1	The Tersoff-Hamann approach . . . . .	45
5.2	Connecting the density and the current . . . . .	46
5.3	Constant-current mode . . . . .	47
5.4	Applying to periodic DFT calculations . . . . .	48
5.5	Applying to USPP and PAW formalisms . . . . .	48

---

5.6	Scanning tunneling spectroscopy . . . . .	49
<b>6</b>	<b>Results</b>	<b>51</b>
6.1	Thin-film effects on atoms and small molecules . . . . .	51
6.1.1	Early results . . . . .	51
6.1.2	A systematic study . . . . .	53
6.2	Thin-film effects on metallic clusters . . . . .	62
6.2.1	Thin-film effects on the Au clusters of 2-6 atoms . . . . .	62
6.2.2	Thin-film effects on the Au clusters of 6-20 atoms . . . . .	67
6.3	Towards chemistry of Au clusters . . . . .	76
6.3.1	The O <sub>2</sub> /Au <sub>1-6</sub> /MgO(3L)/Mo structures and their energetics . .	76
6.3.2	The charging of the optimal geometries . . . . .	78
6.3.3	The projected density of states analysis of the bonding . . . . .	79
6.3.4	One possible scenario of cluster catalysis . . . . .	82
<b>7</b>	<b>Summary and outlook</b>	<b>83</b>

# Abbreviations

<b>1D HO</b>	One dimensional harmonic oscillator
<b>2D HO</b>	Two dimensional harmonic oscillator
<b>AFM</b>	Atomic force microscopy or atomic force microscope
<b>BO</b>	Born-Oppenheimer (approximation)
<b>BZ</b>	Brillouin zone
<b>C</b>	Correlation
<b>DFT</b>	Density functional theory
<b>DOS</b>	Density of states
<b>EELS</b>	Electron energy loss spectroscopy
<b>EPR</b>	Electron paramagnetic resonance (spectroscopy)
<b>ESP</b>	Electrostatic potential
<b>FTIR</b>	Fourier transform infrared (spectroscopy)
<b>GEA</b>	Gradient expansion approximation
<b>GGA</b>	Generalized gradient expansion approximation
<b>GPAW</b>	Grid projector augmented wave (formalism). Also a name of a DFT code using the GPAW formalism.
<b>HF</b>	Hartree-Fock (method)
<b>HK1</b>	The first Hohenberg-Kohn theorem
<b>HK2</b>	The second Hohenberg-Kohn theorem
<b>HOMO</b>	Highest occupied molecular orbital
<b>IUPAC</b>	International union of pure and applied chemistry
<b>KS</b>	Kohn-Sham
<b>LDA</b>	Local density approximation (energy functional)
<b>LDOS</b>	Local density of states
<b>LUMO</b>	Lowest unoccupied molecular orbital
<b>ML</b>	Monolayer
<b>PAW</b>	Projector augmented wave (formalism)
<b>PBE</b>	Perdew-Burke-Ernzerhof (energy functional)
<b>PDOS</b>	Projected density of states
<b>PES</b>	Photo-electron spectrum
<b>PP</b>	Pseudopotential
<b>PW</b>	Plane wave
<b>PW91</b>	Perdew-Wang 1991 (energy functional)
<b>revPBE</b>	A revised Perdew-Burke-Ernzerhof (energy functional)
<b>RPBE</b>	A revised Perdew-Burke-Ernzerhof (energy functional)
<b>ST</b>	Stoneham-Tasker
<b>STM</b>	Scanning tunneling microscopy or scanning tunneling microscope
<b>STS</b>	Scanning tunneling spectroscopy
<b>UHV</b>	Ultra-high vacuum
<b>USPP</b>	Ultra-soft pseudopotential
<b>X</b>	Exchange
<b>XC</b>	Exchange and correlation



# 1 Introduction

## 1.1 Metal clusters

According to International Union of Pure and Applied Chemistry (IUPAC), a metal cluster is "a number of metal centres grouped close together which can have direct metal bonding interactions or interactions through a bridging ligand, but are not necessarily held together by these interactions." This is not a very strict definition, and the viewpoint of this thesis is more inherent from the history of cluster physics [1, 2]. In cluster physics, a metal cluster is typically considered as an aggregate of metal atoms whose size can range from a dimer consisting of two single atoms to a particle of tens of thousands of atoms [1, 2]. Already in the 1960's and 1970's, it was found that the properties of such particles differ from bulk material. This was not surprising as the ratio of surface atoms to bulk atoms is large in a small particle and the surface atoms have different properties than the bulk atoms. On the other hand, also molecules can be seen as aggregates of small number of atoms and they can have very different properties depending on the number of atoms. Thus, every individual cluster size could be seen as an individual molecule having its characteristic chemical properties.

However, it was not until the 1980's when it was found that there exists systematic behavior as a function of metal cluster size. The peaks in the Na cluster abundance spectrum corresponded to shell closing numbers for valence electrons predicted by the jellium model [1, 2]. In this model, the sodium cluster is described as a positively charged sphere to which its atomic 3s electrons are confined. In such a system, electrons have bound states and shell structure in analogy to atoms. Thus, the physical and chemical properties of metal clusters are to large extent determined by the valence electron states which are not localized to single cluster atoms but to the metal particle as a whole. This has led to the concept of superatom, which is an object having atom like states and shell structure but consisting of numerous atoms. On the other hand, the size of a cluster can be seen as a third dimension added perpendicularly to the rows and columns of the periodic system of the elements. In an ordinary periodic table, the properties of elements change when moving along rows and columns of the table. Now, they change also when moving along the third axis perpendicular to the traditional two.

Often, an additional line is drawn between the size scales of sub-nano-sized-clusters

and nano-sized-clusters. The latter ones are often called nanoparticles. On sub-nano-size regime, every atom counts. This means that the physical and chemical properties of a cluster can totally change when its size is changed by one atom or the charge state by one electron. This is mainly due to drastic size dependent changes in their discrete electronic states. On the contrary, the properties of nanoparticles can be scaled down from the properties of the bulk metal [2]. The difference between the large nanoparticles and bulk materials comes mainly from the local or global differences in their band structures. In this thesis, mainly the properties of the sub-nano-sized clusters are discussed.

## 1.2 Gold, gold clusters and catalysis

Bulk gold is shiny yellow soft chemically inert metal. It has been used for decoration and jewelery for ages as it is easy to reshape and it retains its shine also in the long run. However, the modern use of bulk gold includes also electronics, in which the excellent conduction properties and resistance to corrosion via oxidation are taken advantage of [3].

Like other small metal aggregates, also gold clusters have size dependent properties which differ from the bulk material. In the case of gold clusters, the atomic 6s states delocalize over the cluster atoms creating a superatom with shell structure [4]. Thus, for example, the electron affinity of gold depends on cluster size [5]. However, gold clusters also have interesting properties that differ from other metal clusters. For example, as Au is heavy metal with high nuclear charge, the kinetic energies of its core electrons are so high that the relativistic effects are significant. These effects lead to contraction of 6s valence orbitals whereas 5d valence orbitals are expanded. The energy difference between s and d states is decreased and leads to s-d hybridized states. These states are crucial in the bonding between Au atoms and the d character makes the bonds highly directional. Due to this, gas-phase gold clusters favor two dimensional (2D) planar structures also in larger particles than the other metals [6]. In addition, interesting cage-like structures have been reported [4].

However, possibly the most important reason for the modern gold rush in the research during the last two decades has been the discovery that although gold is an inert noble metal as a bulk material, it is catalytically active in cluster form. In the early 80's, Graham Hutchings predicted [7] that gold does not only be a catalyst, but it is actually the best one for acetylene hydrochlorination reaction on a carbon support. Hutchings found that, in such a system, the catalytic activity correlates to the standard electrode potential of the catalyst and actually the cationic gold,  $\text{Au}^{3+}$ , has a very optimal value. Soon, this was experimentally confirmed [8, 9, 10]. Around the same time, Haruta *et al.* found independently that Au nanoparticles of 2-4 nm in diameter supported



by larger  $\text{Fe}_2\text{O}_3$ ,  $\text{Co}_3\text{O}_4$  and  $\text{NiO}$  particles catalyze the  $\text{CO}$  oxidation to  $\text{CO}_2$  [11]. Since then, considerable amount of research has been done to explain the catalytic properties of gold clusters. In addition to the reactions mentioned above, gold has been found to catalyze propylene epoxidation [12],  $\text{NO}$  reduction [13], hydrogenation of unsaturated hydrocarbons [14] and nitro compounds [15], water-gas shift reaction [16] and oxidation of diols [17], to mention some.

To unravel the special activity of gold, both, gas-phase and supported cluster have been studied extensively. In the gas-phase studies [18, 19, 20, 21], charge state and the size of the clusters can be controlled accurately. This provides a possibility to study the catalytic properties of the clusters as a function of their size and charge. However, the drawback is that the possible support effects are completely excluded. The research of the supported clusters have divided into studies of ultra-high vacuum (UHV) model systems [22, 23, 24, 25, 26, 27] and more industry like catalytic reactors [7, 9, 11, 12, 14, 15, 17]. The systems of the first group try to mimic the more realistic catalysts of the latter group, but are set up in highly controllable manner and are typically possible to analyze with higher number of tools, such as scanning tunneling microscopy (STM), atomic force microscopy (AFM), electron paramagnetic resonance (EPR), Fourier transform infrared spectroscopy (FTIR) or electron energy loss spectroscopy (EELS), to name a few. The aim is to catch the essential physics and chemistry of the real systems in a more easily investigated model system. During the last two decades, also the computational modeling of gas-phase [21, 28, 29, 30, 31] and surface systems [24, 26] have become possible. This provides atomic level understanding of catalytic phenomena. Catalysis in general is very important for the society. For example, it has been estimated that over 20 % of the gross national product of industrial countries is directly or indirectly connected to catalysis [32].

In a large number of experimental and computational studies, the Au cluster catalysis has been found to depend on the following factors: i) Au particle size [22, 32], ii) low-coordinated sites on the particles [32, 33, 34, 35], iii) sites on the particle-support interface [36], iv) quantum-size effects of tiny Au clusters [21, 24, 25, 26, 29, 30, 31, 37], v) charge or oxidation state of the cluster [7, 24, 25], vi) support induced strain on the particle [38], vii) insulator-to-metal-transition [22], viii) dynamic structural fluxionality of the small particles [26] and ix) reducibility of the support [39]. It is likely that the factors governing the catalysis are not the same in all the systems, and possibly several of them are active on the same time.

## 1.3 Thin films and thin-film supported adsorbates

In the UHV model systems, the catalytically active metal particles are often studied on an oxide surface. The oxide supports are typically made by growing the oxide film on

a metal carrier. The clusters are either mass-selected in gas-phase and soft-landed to the surface with low kinetic energies, or grown via vapor deposition leading to cluster formation on the surface. For example, if scanning tunneling microscopy is used to probe the adsorbates, the insulating oxide film must be very thin as the tunneling current must pass through the whole system. The thickness of the oxide film can be controlled via the time of its growing.

Thin films are not novel systems, and it has been known for a long time that, for example, the oxidation velocity of the film depends on its thickness [40]. However, it has been realized only quite recently that the properties of variety of adsorbates can be very different on thin metal supported oxide films compared to single crystal surfaces. This discovery has two important consequences: i) One should realize that the experiments carried out with thin-film based model systems may have their own features different from the single crystal systems, and ii) one cannot computationally model a thin-film system without including the carrier metal explicitly in the calculations. During the last half a decade, this has raised the experimental and computational studies of thin-film effects as a hot topic among the community studying UHV model systems of heterogeneous catalysis.

The first computational density functional theory (DFT) results, known already before the work presented in this thesis had begun, show that Au atom and NO<sub>2</sub> molecule adsorb strongly on a MgO thin film supported by Mo metal and become negatively charged [41, 42, 43, 44], whereas on a single crystal film the adsorption is weak and they are neutral [41, 42, 43, 44, 45, 46, 47, 48, 49, 50, 51]. Also the favored adsorption site can be different on a thin film as on a single crystal surface [42, 44]. Recent STM experiments support these predictions [52, 53]. These results are discussed in more detail in section 6.1.1 of chapter 6. The work presented in this thesis [I-VI] as well as other recent studies expand the scope of investigation to variety of adsorbates such as transition metal [54] and alkali [55] atoms, molecules like O<sub>2</sub> [VI], NO<sub>2</sub> [III] [56] and CO [57], and Au clusters up to tens of atoms [I-VI] [52, 57, 58, 59, 60]. The literature also covers a variety of thin-film substrates: MgO/(Ag, Pd, Pt, Au) [III], Al<sub>2</sub>O<sub>3</sub>/Ag [61], Al<sub>2</sub>O<sub>3</sub>/NiAl [59], BaO/Pt [56], SiO<sub>2</sub>/Mo [55, 62, 63], TiO<sub>2</sub>/Pt [55], NiO/Ag [54] and FeO/Pt [64] among others [65, 66]. In many of these thin-film systems, the electronic, energetic and structural properties of adsorbates differ from those on single crystal as discussed in the light of papers [I-VI] in chapter 6. For example, on MgO/Mo, gold clusters favor chain or planar structures which wet the surface and become spontaneously charged, whereas on single crystal MgO, the clusters have less surface contact and are essentially neutral. Note that cluster charge has been suggested as an important factor for catalysis, especially in the case of the non-scalable size regime. Furthermore, the geometry dependence on the MgO film thickness might tune the number of low-coordinated sites on the cluster or the active sites on the cluster boundaries. This scenario is discussed in chapter 7

In the section 1.2 above, a list of factors (i)-(ix) governing cluster catalysis is given. The recent studies on thin-film effects suggest that one should add an item more to the list, namely: x) Thin-film effects on adsorbates. This is discussed in chapters 6 and 7 in more detail.

## 1.4 The Nobel prize methods: DFT and STM

During the last two decades, DFT and STM have become very popular and useful tools in the research of surface and nanoscience. Whereas DFT is the state of the art method for computational modeling of surface science systems, STM is the number one tool for experimental spatial characterization of the surfaces and the adsorbates on them. The developments of both methods have led to Nobel prizes. The first working STM was build in the early 1980s by Gerd Binnig and Heinrich Rohrer [67] and, due to this, the Nobel prize in physics was shared by them already in 1986 [68]. The DFT was developed already in the early 1960s by Walter Kohn in collaboration with Pierre Hohenberg and Lu J. Sham [69, 70]. For this, Walter Kohn was awarded the Nobel prize in chemistry in 1998 [71].

The development of DFT could be considered as the first important step towards computational modeling of surface science systems. DFT is an *ab initio* method, which means that the only input parameters are the names of the elements and their coordinates. The output is the ground state electron density and the energy of the system. The power of DFT relies on the fact that the ground state of a system is determined solely by its density, which is conceptually simpler and computationally easier quantity than a many-body wave function. DFT is the only quantum physical method which can be practically used for extensive screening of surface system properties in a reasonable time and accuracy. The second important step has been the development of massively parallelized implementations of DFT for supercomputers, whereas the third step has been the fast development of the supercomputers themselves. The DFT is discussed in more detail in chapters 2 and 3.

The development of STM has provided a possibility to image surfaces in molecular, or even in atomic resolution. In STM, the surface is scanned with a tip which interacts with the surface via tunneling phenomena. Depending on the bias voltage between the tip and the sample, the electrons tunnel either from the surface states to the tip states or *vice versa*. This corresponds to probing of the occupied or unoccupied states of the surface, respectively. If the distance between the tip and the sample is adjusted so that the tunneling current stays constant, a contour can be plotted, which shows the shapes of the surface states. Importantly, surface can be examined locally in real space, and thus, properties of single adsorbates can be investigated. In many non-local methods, such as FTIR and EPR, only the ensemble properties of adsorbates can be

measured. If the surface has, for example, a wide distribution of different sized metal clusters, only their average properties can be observed. In STM, one cluster can be selected for investigations, and it is even possible to modify its structure and charge state [72, 73, 74].

These days, the power of STM and DFT can be combined for characterizing surface systems. For example, in ref. [73], a bond formation between a gold atom and a pentacene molecule have been observed and rationalized in a combined DFT/STM study. In paper [V], gold clusters and their charge states have been identified with the help of DFT and STM. The computational work related to study [V] has been carried out in Jyväskylä whereas the STM experiments have been done in Berlin. The STM, and especially, STM simulations based on DFT calculations, are discussed in more detail in chapter 5. The results of the combined study of paper [V] are discussed in chapter 6.

## 1.5 About this thesis

In this thesis, I will focus on density functional theory characterization of one type of a heterogeneous catalytic UHV model system, namely gold clusters deposited on metal supported thin oxide films. The special catalytic activity of gold as a whole would be far too general topic for one thesis. Thus, the emphasis is on the properties of Au clusters on one irreducible oxide, MgO, which is supported either by Mo or Ag. However, to get more general picture, some results of O<sub>2</sub> and NO<sub>2</sub> adsorption on thin-films are given and also Mo supported Al<sub>2</sub>O<sub>3</sub> oxide film as well as Pd, Pt and Au supported MgO films have been considered in selected cases. To get a glimpse to the chemistry, O<sub>2</sub> adsorption properties have been calculated for Au<sub>1</sub>-Au<sub>6</sub> on Mo supported MgO. Knowledge of O<sub>2</sub> adsorption is crucial if oxidation catalytic activity of these small species will be examined further. However, detailed investigation of actual catalytic reactions is out of the scope of this thesis.

The thesis is arranged as follows. First, the basics of density functional theory are discussed: Chapter 2 presents the theory itself whereas chapter 3 is about the issues related to practical computational implementations of the theory, such as pseudopotentials and basis sets. The focus is in the solutions used in the DFT packages Dacapo [75] and GPAW [76], which are the codes applied in the studies [I-VI]. Second, in chapter 4, the analysis methods for DFT output data are discussed. The important energy related quantities, like adsorption and formation energies are defined, and density and eigenstate based analysis methods applied in this thesis will be explained. The whole chapter 5 is devoted to the simulation of STM. Finally, in chapter 6, the results obtained in the papers [I-VI] will be presented. I will begin by discussing the thin-film effects on atoms and small molecules and the generality of the phenomenon. After this,

---

the special properties of thin-film supported Au clusters are presented in comparison to Au clusters on bulk-like oxide surfaces. For selected clusters, their characterization and identification with combined STM/DFT-approach is discussed. Furthermore, O<sub>2</sub> adsorption properties on thin-film supported Au clusters are presented and the possible consequences for catalysis discussed. Finally, a summary and outlook is given in chapter 7.



## 2 Density functional theory

In general, all the problems of solid-state physics and chemistry reduce to a quantum mechanical many-body problem of electrons and nuclei. In the following sections, the nature of the problem and the essential approximations needed to make it practically solvable are investigated. Especially, the basics of the density functional theory are discussed. I will introduce only the general ideas relevant for understanding the theoretical background of this thesis. The quantum mechanical many-body problem is a topic in numerous text books, such as [77, 78], and also DFT is discussed in several books [78, 79, 80], review articles [81, 82, 83] and lecture notes of the researchers in the field [84, 85, 86].

### 2.1 The many-body Hamiltonian of interacting electrons and nuclei

The time independent Schrödinger equation is of the form

$$\hat{H}\Psi = E\Psi, \quad (2.1)$$

in which  $\hat{H}$  is the Hamiltonian operator,  $\Psi$  is the many-body wave function with all the particle coordinates as variables and  $E$  the total energy of the system. The Hamiltonian for the system of  $N$  electrons and  $M$  nuclei can be written in the form

$$\begin{aligned} \hat{H} = & -\frac{\hbar^2}{2m_e} \sum_{i=1}^N \nabla_i^2 - \sum_{i=1}^N \sum_{I=1}^M \frac{Z_I e^2}{|\mathbf{r}_i - \mathbf{R}_I|} + \sum_{i=1}^N \sum_{j>i}^N \frac{e^2}{|\mathbf{r}_i - \mathbf{r}_j|} \\ & - \sum_{I=1}^M \frac{\hbar^2}{2M_I} \nabla_I^2 + \sum_{I=1}^M \sum_{J>I}^M \frac{Z_I Z_J e^2}{|\mathbf{R}_I - \mathbf{R}_J|}, \end{aligned} \quad (2.2)$$

in which  $\hbar$  is the Planck constant,  $m_e$  the mass of an electron,  $e$  the elementary charge,  $Z_I$  is the atomic number and  $M_I$  the mass of nucleus  $I$ . The coordinates of electrons and nuclei are denoted with vectors  $\mathbf{r}_i$  and  $\mathbf{R}_I$ , respectively.

In the Hamiltonian, the terms with the operators  $\nabla_i^2$  and  $\nabla_I^2$  give the kinetic energies of the electrons and nuclei, respectively. The rest of the terms describe the Coulomb interactions between the charged particles: The second term between the nuclei and electrons, third term between the electrons and the last term between the nuclei.

The eigenfunctions of (2.1) are the possible many-body states of the system and the corresponding eigenvalues give the state energies. According to the variational principle, the eigenstates give the extrema of the energy functional

$$E[\Psi] = \langle \Psi | \hat{H} | \Psi \rangle = \int \Psi \hat{H} \Psi d\mathbf{r} \quad (2.3)$$

with the constraint that  $\langle \Psi | \Psi \rangle = 1$ . The lowest possible energy is given by the ground state. In principle, it could be solved by minimizing  $E[\Psi]$  respect to all allowed many-body states.

In principle, all the chemistry can be described with this one equation, or at least, with its relativistic counterpart. However, unfortunately the exact solving of the Schrödinger equation (2.1) with the Hamiltonian (2.2) is practically impossible for the system sizes relevant for solid-state physics and chemistry. Thus, several approximations are needed.

## 2.2 The Born-Oppenheimer approximation

The Born-Oppenheimer (BO) approximation [78] is usually applied regardless of whatever additional simplifications are done. This approximation is based on the fact that the masses of the nuclei are large compared to the masses of electrons, *i.e.*, in the Hamiltonian (2.2)  $M_I \sim 1000m_e$ . Consequently, the nuclei move considerably slower than the electrons. Thus, the electronic system can be separately solved in the Coulomb potential of the fixed nuclei. The electronic Schrödinger equation is then

$$\hat{H}_{\text{elec}} \Psi = E_{\text{elec}} \Psi \quad (2.4)$$

with the Hamiltonian of the form

$$\hat{H}_{\text{elec}} = -\frac{\hbar^2}{2m_e} \sum_{i=1}^N \nabla_i^2 - \sum_{i=1}^N \sum_{I=1}^M \frac{Z_I e^2}{|\mathbf{r}_i - \mathbf{R}_I|} + \sum_{i=1}^N \sum_{j>i}^N \frac{e^2}{|\mathbf{r}_i - \mathbf{r}_j|}, \quad (2.5)$$



in which the electron coordinates  $\mathbf{r}_i$  are variables and the nucleus coordinates  $\mathbf{R}_I$  are fixed parameters determining the form of the Hamiltonian. Now, the total energy of the system can be evaluated as a sum of the electronic energy and the classical Coulomb energy of the nuclei as follows

$$E = E_{\text{elec}} + \sum_{I=1}^M \sum_{J>I}^M \frac{Z_I Z_J e^2}{|\mathbf{R}_I - \mathbf{R}_J|}. \quad (2.6)$$

## 2.3 The Hohenberg-Kohn theorems

Density functional theory [69, 70, 78, 81, 82, 83] is the method which best compromises between the accuracy and the applicable system size when solving the ground state of an electronic many-body problem. The success of the DFT is due to the fact that any property of a many-body system can be solved with an appropriate functional of the ground-state density  $n_0(\mathbf{r})$ . In solid-state physics, the problem of  $N$  interacting electrons in the potential of nuclei can be thus described with the help of a function of three coordinates,  $n_0(\mathbf{r})$ , instead of a many-body wave function  $\Psi(\mathbf{r}_1, \mathbf{r}_2, \dots, \mathbf{r}_N)$ , a function of  $3N$  variables.

Let's now consider an electronic Hamiltonian of the form

$$\hat{H}_{\text{elec}} = -\frac{1}{2} \sum_{i=1}^N \nabla_i^2 + \sum_{i=1}^N V_{\text{ext}}(\mathbf{r}_i) + \sum_{i=1}^N \sum_{j>i}^N \frac{1}{|\mathbf{r}_i - \mathbf{r}_j|}, \quad (2.7)$$

in which  $V_{\text{ext}}(\mathbf{r}_i)$  is an external potential which, for example, can include the potential of the nuclei in the Born-Oppenheimer approximation. To reduce the notation, atomic units ( $e = a_0 = m_e = \hbar = 1$ ) have been applied. In 1964, Hohenberg and Kohn published two theorems with remarkable corollaries [69]. The first theorem (HK1) states that the potential  $V_{\text{ext}}(\mathbf{r}_i)$  is uniquely determined by the ground state electron density  $n_0(\mathbf{r})$ , except for a constant. From this it follows that the Hamiltonian above is fully determined except for an irrelevant constant shift. The Hamiltonian determines all the ground and excited electronic states of the system. Thus all the properties of the system can be deduced from the ground state electron density.

The second theorem (HK2) states that there exists an universal functional  $E[n]$  that gives the total energy of the system in terms of the electron density  $n(\mathbf{r})$ . For a given  $V_{\text{ext}}(\mathbf{r}_i)$ , the ground state energy is the global minimum of the functional  $E[n]$  and it is given by the ground state density  $n_0(\mathbf{r})$ .

The HK1 is easy to prove for a system with non-degenerate energy levels. The generalization for degenerate case is not shown here. Consider two external potentials,  $V_{\text{ext}}(\mathbf{r}_i)$  and  $V'_{\text{ext}}(\mathbf{r}_i)$ . Let's assume that these potentials differ from each other by more than a constant, but still lead to same ground state density  $n_0(\mathbf{r})$ . These potentials define two different Hamiltonians,  $\hat{H}$  and  $\hat{H}'$ , which are of the form (2.7). These two Hamiltonians give two different ground state wave functions  $\Psi$  and  $\Psi'$ , which we now assume to give the same density  $n_0(\mathbf{r})$ . Now

$$E = \langle \Psi | \hat{H} | \Psi \rangle < \langle \Psi' | \hat{H} | \Psi' \rangle \quad (2.8)$$

as  $\Psi$  is the ground state of  $\hat{H}$  whereas  $\Psi'$  is not. By addition of a zero, the second term can be written in the form

$$\langle \Psi' | \hat{H} | \Psi' \rangle = \langle \Psi' | \hat{H}' | \Psi' \rangle + \langle \Psi' | \hat{H} - \hat{H}' | \Psi' \rangle = E' + \int [V_{\text{ext}}(\mathbf{r}_i) - V'_{\text{ext}}(\mathbf{r}_i)] n_0(\mathbf{r}) d\mathbf{r}. \quad (2.9)$$

Thus one gets

$$E < E' + \int [V_{\text{ext}}(\mathbf{r}_i) - V'_{\text{ext}}(\mathbf{r}_i)] n_0(\mathbf{r}) d\mathbf{r}. \quad (2.10)$$

However, by interchanging the primed and non-primed quantities, one can carry out exactly the same deductions and arrive to

$$E' < E + \int [V'_{\text{ext}}(\mathbf{r}_i) - V_{\text{ext}}(\mathbf{r}_i)] n_0(\mathbf{r}) d\mathbf{r}. \quad (2.11)$$

By adding the two equations together, one will have

$$E + E' < E + E', \quad (2.12)$$

which is a contradiction. Thus, the assumption that two external potentials differing more than by a constant could lead to the same ground state density, was wrong.

The total energy functional of the DFT can be written in the form

$$E[n] = T[n] + W[n] + V_{\text{ext}}[n], \quad (2.13)$$

in which  $T[n]$  is the kinetic energy functional,  $W[n]$  is the functional of the Coulomb energy of the electron-electron interactions and  $V_{\text{ext}}[n]$  is the functional of the potential energy of the electrons in the external potential. All of these are functionals of the electron density  $n$ . This can be also written as

$$E[n] = F_{\text{HK}}[n] + V_{\text{ext}}[n], \quad (2.14)$$

in which the functional

$$F_{\text{HK}}[n] = T[n] + W[n] \quad (2.15)$$

is universal for all the Coulomb systems and the differences are caused solely by the external potential via the functional  $V_{\text{ext}}[n]$ .

The ground state density is the density giving the lowest energy, *i.e.*, the minimum value for the functional (2.13). Thus, the functional derivative of (2.13) must be zero for the minimum density. This leads to

$$\frac{\delta E[n]}{\delta n(\mathbf{r})} = \frac{\delta F_{\text{HK}}}{\delta n(\mathbf{r})} + \frac{\delta V_{\text{ext}}[n]}{\delta n(\mathbf{r})} = 0, \quad (2.16)$$

which in turn gives

$$\frac{\delta F_{\text{HK}}}{\delta n(\mathbf{r})} = -V_{\text{ext}}(\mathbf{r}). \quad (2.17)$$

This means that we know the functional derivative of  $F_{\text{HK}}[n]$  as soon as the external potential  $V_{\text{ext}}(\mathbf{r})$  defining the investigated system is given. If we find the density  $n(\mathbf{r})$  so, that the condition (2.17) is fulfilled, we find the ground state density.

## 2.4 The Kohn-Sham ansatz

The problem with the Hohenberg-Kohn theorems is the fact that the functional  $F_{\text{HK}}[n]$  is unknown and the derivation of the theorems do not offer any help to construct the functional. Kohn and Sham approached [70] this problem by writing the universal functional  $F_{\text{HK}}$  with the help of non-interacting single particles in the form

$$F_{\text{HK}}[n] = T_{\text{s}}[n] + V_{\text{H}}[n] + E_{\text{XC}}[n], \quad (2.18)$$

in which  $T_{\text{s}}[n]$  is the kinetic energy of non-interacting particles described by the wave functions  $\phi_i(\mathbf{r})$ ,

$$T_{\text{s}}[n] = -\frac{1}{2} \sum_{i=1}^N \int d\mathbf{r} \phi_i^*(\mathbf{r}) \nabla_i^2 \phi_i(\mathbf{r}), \quad (2.19)$$

$V_{\text{H}}[n]$  is the classical Coulomb energy of the electron cloud,

$$V_{\text{H}}[n] = \frac{1}{2} \int \int d\mathbf{r} d\mathbf{r}' \frac{n(\mathbf{r})n(\mathbf{r}')}{|\mathbf{r} - \mathbf{r}'|}, \quad (2.20)$$

and  $E_{\text{XC}}[n]$  is the so-called exchange and correlation (XC) energy functional - including all the many-body effects excluded by the first two terms. The last term still remains unknown, but it can be approximated as discussed in section 2.5.

The single-particle scheme of the Kohn-Sham (KS) approach - or ansatz as which it is often called - can be constructed as follows: One will have a single particle Hamiltonian

$$\hat{H}_{\text{s}} = \hat{T}_{\text{s}} + \hat{V}_{\text{s}}[n], \quad (2.21)$$

in which  $\hat{T}_{\text{s}}$  is the kinetic energy operator and  $\hat{V}_{\text{s}}$  is the potential energy operator of which form depends on the density as discussed later. The eigenstates of

$$\hat{H}_{\text{s}} \Phi_{\text{s}}[n] = E_{\text{s}} \Phi_{\text{s}}[n] \quad (2.22)$$

are anti-symmetrized as in the Hartree-Fock (HF) approximation as a Slater determinant of the non-interacting single particles

$$\Phi_{\text{s}}[n] = \frac{1}{\sqrt{N!}} \begin{vmatrix} \phi_1(\mathbf{x}_1) & \phi_2(\mathbf{x}_1) & \dots & \phi_N(\mathbf{x}_1) \\ \phi_1(\mathbf{x}_2) & \phi_2(\mathbf{x}_2) & \dots & \phi_N(\mathbf{x}_2) \\ \vdots & \vdots & \ddots & \vdots \\ \phi_1(\mathbf{x}_N) & \phi_2(\mathbf{x}_N) & \dots & \phi_N(\mathbf{x}_N) \end{vmatrix}, \quad (2.23)$$

in which the coordinates  $\mathbf{x}_i$  consist of the spatial and spin coordinates  $\mathbf{r}_i$  and  $\sigma_i$ , respectively. The density is given by

$$n(\mathbf{r}) = \langle \Phi_s[n] | \hat{n}(\mathbf{r}) | \Phi_s[n] \rangle, \quad (2.24)$$

in which

$$\hat{n}(\mathbf{r}) = \sum_{i=1}^N \delta(\mathbf{r} - \mathbf{r}_i) \quad (2.25)$$

is the density operator. By using the operators

$$\hat{T}_s = \sum_{i=1}^N -\frac{1}{2} \nabla_i^2 \quad (2.26)$$

and

$$\hat{V}_s = \sum_{i=1}^N -\frac{1}{2} V_s(\mathbf{r}_i) \quad (2.27)$$

and combining the equations (2.22) and (2.23) one notices that the energy  $E_s$  in (2.22) can be written as

$$E_s = \sum_{i=1}^N \varepsilon_i, \quad (2.28)$$

in which the  $\varepsilon_i$  are the eigenvalues of the single particle Schrödinger equation

$$\left(-\frac{1}{2} \nabla^2 + V_s[n](\mathbf{r})\right) \phi_i(\mathbf{x}) = \varepsilon_i \phi_i(\mathbf{x}). \quad (2.29)$$

In the Kohn-Sham ansatz, the density  $n$  we are searching for, is the ground state density of the interacting system. Thus, the potential  $V_s[n](\mathbf{r})$  experienced by the single particles is not the external potential of the true system but an effective potential in which the single particles reproduce the density of the interacting system. In the following sections, I will describe how the potential can be found.

Now, in the Kohn-Sham ansatz, substitution of eq. (2.18) to eq. (2.17) will lead to

$$\frac{\delta T_s[n]}{\delta n(\mathbf{r})} + \frac{\delta V_H[n]}{\delta n(\mathbf{r})} + \frac{\delta E_{XC}[n]}{\delta n(\mathbf{r})} = -V_{\text{ext}}(\mathbf{r}). \quad (2.30)$$

For the known functionals, the derivatives can be calculated to be

$$\frac{\delta T_s[n]}{\delta n(\mathbf{r})} = -V_s(\mathbf{r}), \quad (2.31)$$

in which  $V_s(\mathbf{r})$  is the single particle potential of the Kohn-Sham system, and

$$\frac{\delta V_H[n]}{\delta n(\mathbf{r})} = \int d\mathbf{r}' \frac{n(\mathbf{r}')}{|\mathbf{r} - \mathbf{r}'|} =: V_H[n](\mathbf{r}). \quad (2.32)$$

The functional derivative of the exchange and correlation energy, called the exchange and correlation potential

$$V_{XC}[n](\mathbf{r}) := \frac{\delta E_{XC}[n]}{\delta n(\mathbf{r})}, \quad (2.33)$$

is still unknown. The approximations for this quantity are discussed in section 2.5.

Combining the equations (2.30), (2.31), (2.32) and (2.33) gives an expression for the single particle potential of the Kohn-Sham system

$$V_s[n](\mathbf{r}) = V_{\text{ext}}[n](\mathbf{r}) + V_H[n](\mathbf{r}) + V_{XC}[n](\mathbf{r}). \quad (2.34)$$

This is the effective single particle potential needed for the Kohn-Sham system to reproduce the density of the interacting system as a density of the non-interacting particles.

By substituting (2.34) to (2.29) yields

$$\left(-\frac{1}{2}\nabla^2 + V_{\text{ext}}(\mathbf{r}) + V_H(\mathbf{r}) + V_{XC}(\mathbf{r})\right)\phi_i(\mathbf{x}) = \varepsilon_i\phi_i(\mathbf{x}), \quad (2.35)$$

in which the density can be written using the single particle states

$$n(\mathbf{r}) = \sum_{\sigma} \sum_{i=1}^N |\phi_i(\mathbf{x})|^2. \quad (2.36)$$

Clearly, the potentials  $V_H[n](\mathbf{r})$  and  $V_{XC}[n](\mathbf{r})$  are functionals of density  $n(\mathbf{r})$  and thus not explicitly given. However, the set of equations (2.35) with (2.36), called the Kohn-Sham equations, holds for the minimum of  $E[n]$  and it can be solved numerically. In practice, one starts from some educated guess for the initial density  $n_i(\mathbf{r})$ . This can be substituted to the equation (2.34) which gives an initial guess for the effective single-particle potential  $V_s[n]$ , as far as we have an approximation for  $V_{XC}[n]$ . Then the Kohn-Sham equations (2.35) are solved with this potential. From the eigenstates  $\phi_i(\mathbf{x})$  one can calculate a new density via (2.36). This density gives a new potential which is again fed to the Kohn-Sham equations, which in turn, give again new eigenstates and thus a new density. This procedure is iterated until the self-consistency is reached, *i.e.*, the density does not change anymore in the procedure.

## 2.5 The exchange and correlation energies

In the chemistry literature, the exchange and correlation energies are often defined in the picture of the Hartree-Fock approximation [78, 83, 87]. In the HF, the total energy includes the Coulomb interaction calculated for each electron in the mean-field of the other electrons and fixed nuclei, and the exchange term which guarantees the antisymmetry of the wave function. However, in a Coulomb system, there is also more correlation between the electrons, than the one arising solely from the statistics and mean-field interaction of the electrons. This is not included in the Hartree-Fock, and thus, correlation energy can be defined as the difference between the true energy and the Hartree-Fock energy. Thus, the more sophisticated methods, like the configuration interaction, bring in more correlation [78, 87]. In DFT, the intuitive meaning of the concepts is similar in the sense that the exchange is related to fermion statistics whereas the correlation is related to Coulomb interactions. However, the exact definitions are different.

Within the DFT formalism, the exchange and correlation energies can be separated to their own terms [78, 80, 83, 85, 86]

$$E_{XC}[n] = E_X[n] + E_C[n], \quad (2.37)$$

in which the exchange (X) energy can be written rigorously as follows

$$E_X[n] = \frac{1}{2} \int d\mathbf{r} \int d\mathbf{r}' \frac{n(\mathbf{r})n_X(\mathbf{r}'|\mathbf{r})}{|\mathbf{r} - \mathbf{r}'|} \quad (2.38)$$

with the help of the exchange hole  $n_X(\mathbf{r}'|\mathbf{r})$ , which can be interpreted as the missing

charge density at  $\mathbf{r}$  due to electron at  $\mathbf{r}'$  in a non-interacting system with the ground state density of an interacting system. As the system is non-interacting, the hole is entirely created by the fermion statistics, *i.e.*, it exists due to Pauli exclusion principle. The exchange energy can be interpreted as an interaction energy between the electron and hole densities. Note that a similar presentation for the hole can also be constructed in the HF formalism. However, there, the density is calculated from the HF orbitals and is never the exact density as it is in the ideal DFT. This is a clear source for difference in HF and DFT exchange energies.

The DFT correlation (C) energy can be written, in a similar way,

$$E_C[n] = \frac{1}{2} \int d\mathbf{r} \int d\mathbf{r}' \frac{n(\mathbf{r})\bar{n}_C(\mathbf{r}'|\mathbf{r})}{|\mathbf{r} - \mathbf{r}'|} \quad (2.39)$$

by using the coupling constant averaged correlation hole  $\bar{n}_C(\mathbf{r}'|\mathbf{r})$ . A correlation hole can be interpreted as the missing density at  $\mathbf{r}$  due to electron at  $\mathbf{r}'$  due to many-body interactions beyond the exchange effect. Again, the energy can be rationalized as the interaction energy between the electron and hole densities. Note, however, that the coupling constant averaged correlation hole needed here is an averaged hole of the holes calculated for scaled Coulomb interactions (from non-interacting to fully interacting) the system having always the ground state density of the fully interacting system. Where the DFT correlation energy brings in the contribution of the electron-electron interactions beyond the exchange and the correlation correction to the kinetic energy term, in the HF picture, the correlation energy must compensate all the errors made in the single Slater-determinant approximation for the many-body wave function. This does not include only corrections to the electron-electron interactions, but also to the interactions between the nuclei and the electrons. Thus, the correlation energy of DFT is different than the one defined in the HF picture.

The exchange and correlation holes are well defined within the many-body quantum mechanics [83] and can be calculated accurately for systems solvable for example with Quantum Monte-Carlo methods. Furthermore, many general properties of the exact exchange and correlation holes are known. For example, they have to obey the sum rules

$$\int d\mathbf{r}' n_X(\mathbf{r}'|\mathbf{r}) = -1 \quad (2.40)$$

and

$$\int d\mathbf{r}' \bar{n}_C(\mathbf{r}'|\mathbf{r}) = 0 \quad (2.41)$$



as well as the negativity condition

$$n_X(\mathbf{r}'|\mathbf{r}) \leq 0. \quad (2.42)$$

These facts provide a way to improve the approximations to the DFT exchange and correlation functionals by approximating the exchange and correlation holes.

## 2.6 The local density approximation

In the local density approximation (LDA) [78, 88, 89, 90], the exchange and correlation energy functional is of the form

$$E_{XC}^{LDA}[n] = \int d\mathbf{r} n(\mathbf{r}) \epsilon_{XC}(n(\mathbf{r})), \quad (2.43)$$

where  $\epsilon_{XC}(n(\mathbf{r}))$  is the exchange-correlation energy density of the homogeneous electron gas, *i.e.*, the sum of the exchange and correlation energy densities ( $\epsilon_{XC} = \epsilon_X + \epsilon_C$ ). One thus approximates that the exchange and correlation energy densities of inhomogeneous electron gas  $n(\mathbf{r})$  are locally equal to the corresponding energies of entirely homogeneous electron gas. The first guess would be that LDA performs well only in the systems having slowly varying densities. However, it has been found that it performs surprisingly well also with the atoms and molecules having strong density variations. This success has been addressed to the fact that the exchange-correlation hole of LDA is exact for one system - the homogeneous electron gas - and the spherical average of the hole seems to be near to the one of the exact hole also for inhomogeneous systems [91]. Comparison to experiments have shown that the mean absolute error of LDA in molecular atomization energies is around 32 kcal/mol [92] and comparison to experimental microcalorimetric adsorption energies of O, CO and NO on Ni, Pd and Rh surfaces reveals that the LDA overbinds the adsorbates about by 1.5 eV [93].

## 2.7 Gradient expansion approximations

In the gradient expansion approximation (GEA) [84, 86, 94], the inhomogeneity of the density is taken into account by carrying out a functional Taylor expansion of the exchange-correlation functional relative to density variation. This introduces gradient operators to the energy functional. However, the XC-hole of GEA violates the

conditions (2.40) and (2.42) and does not perform well in atoms and molecules. In the generalized gradient expansion approximations (GGA) [84, 86, 94], the exchange-correlation hole is expanded as a gradient approximation with physical constraints. The GEA X-hole can be replaced with a new GGA X-hole, which fulfills the conditions (2.40) and (2.42). The GEA hole density is replaced by zero for all  $\mathbf{r}'$  where  $n_X^{GEA}(\mathbf{r}'|\mathbf{r})$  is positive or  $|\mathbf{r}' - \mathbf{r}| < R_c(\mathbf{r})$ . For each  $\mathbf{r}$ , the cut-off radius  $R_c(\mathbf{r})$  is determined by the constraint (2.40). In the case of GGA C-hole, the derivation is based on the similar ideas. However, the constraint (2.41) is required instead of (2.40).

In general, the functionals based on this idea, can be expressed in the form

$$E_{XC}^{GGA}[n_\uparrow, n_\downarrow] = \int d\mathbf{r} n(\mathbf{r}) \epsilon_{XC} F_{XC}(r_s, \zeta, s), \quad (2.44)$$

in which the  $F_{XC}(r_s, \zeta, s)$  is the so-called exchange-correlation enhancement factor, which can be divided to exchange and correlation parts. The variable  $r_s$  is the local Wigner-Seitz radius. It is related to density by  $n = 3/4\pi r_s^3$ . The quantity  $\zeta$  is the relative spin-polarization and is defined as  $\zeta = (n_\uparrow - n_\downarrow)/n$ . It can have values from 0 to  $\pm 1$ . The last variable,  $s$ , is a reduced density gradient

$$s = \frac{|\nabla n|}{2(3\pi^2)^{1/3} n^{4/3}}, \quad (2.45)$$

which is a measure of the inhomogeneity of the system. The derivation of the  $F_{XC}(r_s, \zeta, s)$  from the properties of the X and C holes, and from the many-body quantum mechanics in general, is a rather involved process and a research field of its own. Thus, the details are not discussed here.

In this thesis work, Perdew-Wang 1991 (PW91) [95], Perdew-Burke-Ernzerhof (PBE) [96] and Revised-PBE (RPBE) [93] functionals have been applied. The PW91 functional [95] is constructed so that it fulfills as many as possible known properties of the exact functional, including the sum rules of the XC-hole. However, few years after PW91, Perdew, Burke and Ernzerhof created the PBE functional [96], which mimics the PW91, but with simpler derivation and lighter parametrization. Only the energetically significant physical constraints of PW91 are included in PBE. Furthermore, PBE describes the linear response of uniform electron gas accurately and scales correctly to the high-density limit whereas PW91 fails in those. In addition, the  $V_{XC}$  of PBE is smoother than the one of PW91. In ref. [93], it has been shown that PBE and PW91 overbind the O, CO and NO adsorbates on Ni, Pd and Rh surfaces by around 0.6 eV. The  $F_{XC}(r_s, \zeta, s)$  function of PBE is shown in figs. 2.1 and 2.2 for relative spin polarizations  $\zeta = 0$  and  $\zeta = 1$  and for several densities.

In 1998, Zhang and Yang came up with revPBE [97] functional, in which they improved the exchange functional of PBE by tuning one parameter by fitting the DFT results to the exchange only total atomic energies (from He to Ar) obtained with an exact numerical method. For selected test systems, the revPBE is shown to improve the atomic total energies even by factor of 10. Furthermore, test calculations have shown that the mean absolute error of molecular atomization energies relative to the experimental results is 5 kcal/mol for revPBE whereas the error of PBE is around 8 kcal/mol [97]. However, the enhancement factor for exchange,  $F_X(s)$ , of revPBE does not satisfy the so-called Lieb-Oxford bound [98, 99, 100] by construction. The Lieb-Oxford bound is a theoretical lower bound for the non-classical part of the interaction energy of electron density. Although, in practice revPBE seems to fulfill the Lieb-Oxford bound, it is not guaranteed for an arbitrary density, if  $F_X(s) \leq 1.804$  is not valid for all  $s$ . Hammer, Hansen and Nørskov cured this problem by changing the functional form of PBE  $F_X(s)$  so that it gives the same improvements over PBE as revPBE, but still fulfills all the same physical boundaries as the original PBE. Their functional is known as RPBE [93]. The  $F_X(s)$ s of PBE, revPBE and RPBE are plotted to fig. 2.3. Note that RPBE follows the revPBE but levels off before breaking the condition for the Lieb-Oxford bound.

In addition to improved atomization energies, revPBE and RPBE are shown to overbind O, CO and NO adsorption on metal surfaces only by ca. 0.3 eV [93]. This is already almost within the error bars of the corresponding experimental results, 0.1 - 0.2 eV [93]. However, PBE seems to give slightly more accurate lattice constants for bulk metals than revPBE or RPBE. For example, the lattice constant of 3.99 Å is obtained for Pd with PBE whereas revPBE gives 4.01 Å and RPBE 4.02 Å [93]. The experimental value is 3.89 Å [101].

As PBE and RPBE are based on entirely same physical boundaries, their differences come from the arbitrariness within these limits. Technically, the reason for the difference in the adsorption energies of RPBE and PBE have been addressed to the different energetic description of volumes with high  $s$  (see eq. (2.45)), *i.e.*, with low electron densities having large density gradients [93]. This kind of volume exists on the areas where wave functions decay to the vacuum, *i.e.*, on extended surfaces, or on the surfaces of molecules. Upon adsorption, such a surface area is decreased and thus, its energetic price is important in determining the adsorption energy.

In the papers [I-VI], PBE and RPBE were applied self-consistently, whereas some non-self-consistent PW91 results have been given for easier literature comparison. Note that here the adsorption energies are calculated for bulk oxide and metal supported oxide thin-film surfaces and the accuracy of PBE or RPBE is not necessarily the same as for metal surfaces.

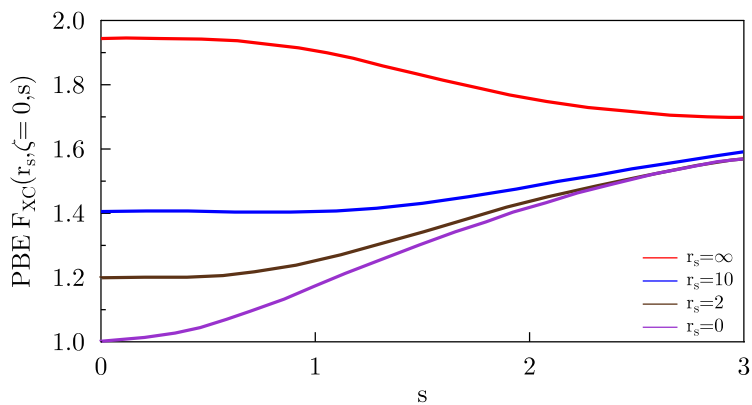


**Figure 2.1:** The exchange-correlation enhancement factor of PBE functional with different densities for relative spin polarization  $\zeta = 0$ . Reproduced from the data given in [96].

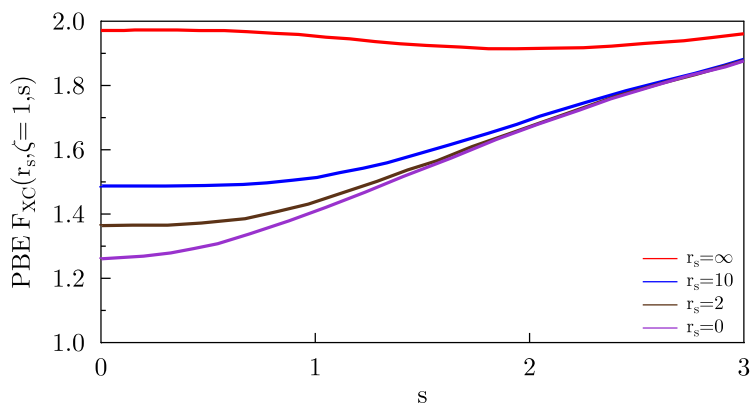


**Figure 2.2:** The exchange-correlation enhancement factor of PBE functional with different densities for relative spin polarization  $\zeta = 1$ . Reproduced from the data given in [96].

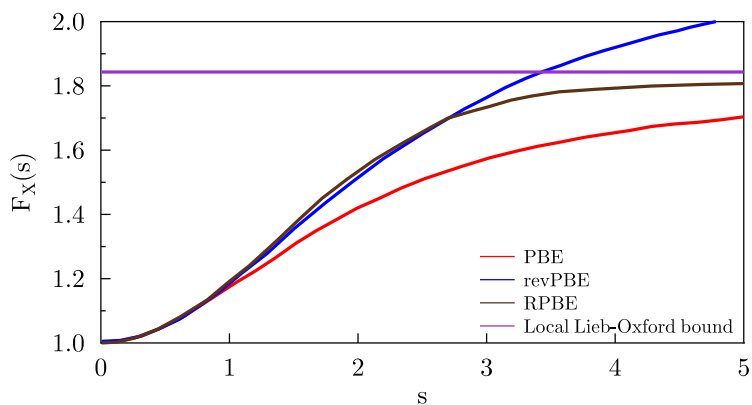


**Figure 2.3:** The exchange enhancement factor of PBE, revPBE and RPBE functionals and the limit for fulfillment of the Lieb-Oxford bound by construction. Reproduced from the data given in [93].



## 3 Issues in practical implementations of density functional theory

### 3.1 Periodic systems

In practice, many large but finite systems are reasonable to model as infinite or semi-infinite periodic systems. For example, ordered bulk materials can be typically described with a few atoms in a unit cell, which is extended to the limit of an infinite material with the periodic boundary conditions in three dimensions. A surface can be modeled with a thick material slab having periodic boundary conditions in the surface plane. Depending on the DFT implementation, it is also possible to have the periodicity in three dimensions as long as the surface slabs are separated by an appropriate amount of vacuum. In surface systems, the size of the periodic cell also determines the distance between the possible adsorbates, *i.e.*, their coverage.

From the Bloch's theorem, one knows that the solutions of the Schrödinger equation in a periodic potential with period  $T$  can be written in the form

$$\phi_{\mathbf{k},i}(\mathbf{r}) = u_i(\mathbf{r})\exp(i\mathbf{k} \cdot \mathbf{r}), \quad (3.1)$$

in which the  $u_i(\mathbf{r})$  is a function having the same periodicity with the potential and modulates the plane wave (PW) solution of a free electron. For a solution of this form, the Bloch's boundary conditions hold

$$\phi_{\mathbf{k},i}(\mathbf{r} + \mathbf{T}) = \exp(i\mathbf{k} \cdot \mathbf{T})\phi_{\mathbf{k},i}(\mathbf{r}). \quad (3.2)$$

In a periodic DFT calculation, solutions of this form are applied to the KS equations. This divides the problem to a separate set of KS equations for each  $\mathbf{k}$ -vector, or  $\mathbf{k}$ -point, as they are often called. Thus, also the solutions and eigenvalues become  $\mathbf{k}$ -point dependent. The space of the  $\mathbf{k}$ -vectors is called reciprocal space.

In this kind of a scheme, the exact overall density is calculated as an average over the first Brillouin zone (BZ) in the reciprocal space as follows

$$n(\mathbf{r}) = \sum_{i=1}^N \frac{1}{\Omega_{\text{BZ}}} \int_{\Omega_{\text{BZ}}} |\phi_{\mathbf{k},i}(\mathbf{r})|^2 d\mathbf{k} \quad (3.3)$$

and, for example, the total energy of the KS non-interacting particles is

$$E_{\text{KS}} = \sum_{i=1}^N \frac{1}{\Omega_{\text{BZ}}} \int_{\Omega_{\text{BZ}}} f_{i,\mathbf{k}} \varepsilon_i(\mathbf{k}) d\mathbf{k}. \quad (3.4)$$

Here,  $\Omega_{\text{BZ}}$  is the volume of the 1<sup>st</sup> Brillouin zone in the reciprocal space and  $f_{i,\mathbf{k}}$  is the occupation of the state  $i$  at point  $\mathbf{k}$  with eigen energy  $\varepsilon_i(\mathbf{k})$ . However, in practice, it is impossible to converge an infinite number of KS equation sets. Thus, the integral operation is replaced with a finite summation

$$\frac{1}{\Omega_{\text{BZ}}} \int_{\omega_{\text{BZ}}} d\mathbf{k} \sim \frac{1}{N_k} \sum_{\mathbf{k}}, \quad (3.5)$$

in which the set of  $\mathbf{k}$ -points is selected so that the sum approaches the integral as fast as possible when the number of  $\mathbf{k}$ -points,  $N_k$ , is increased. Within this thesis, the Monkhorst-Pack  $\mathbf{k}$ -point sampling [102] has been used.

## 3.2 Basis sets and grids

In practice, the Kohn-Sham orbitals are either expanded in terms of some basis function set or described with the help of a real space grid. One possible basis set is the localized atomic orbital basis [78]. In this approach, a set of atomic orbital-like functions is localized to each atom, which matches well to the chemical intuition of single particle orbitals around each nucleus. However, one drawback of using localized functions is that the overall basis set becomes dependent on the number of atoms and their coordinates. This causes error in the relative energies between different systems, which must be corrected. Another widely used basis set is the plane-wave basis [78]. In such a set, each basis function is a spatially delocalized plane-wave and thus the basis is independent of the atomic coordinates. Thus, plane-wave calculations do not need basis set related error corrections. However, one drawback of this approach is the fact that as the form of the basis functions is very general, in principle a larger basis set is needed than in the atomic orbital based calculations. The real-space grid methods [76, 78, 103] are based on different approach. In those, no basis functions are used. Instead, the functions are directly represented on a real-space grid and the



computational accuracy is governed by the grid spacing. In this thesis, all the Dacapo calculations have been carried out by applying plane-wave basis whereas, in the GPAW calculations, real-space grids have been used. Both these methods are discussed in more detail in the next sections.

### 3.2.1 Plane-wave basis

Plane waves [78] provide a complete and orthogonal basis set with which the KS orbitals can be written in the form

$$\phi_i(\mathbf{r}) = \sum_q c_{iq} \frac{1}{\sqrt{\Omega}} \exp(i\mathbf{q} \cdot \mathbf{r}) =: \sum_q c_{iq} |\mathbf{q}\rangle, \quad (3.6)$$

in which the  $c_{iq}$  is a complex coefficient of the plane wave with the wave vector  $\mathbf{q}$  in the expansion of the KS orbital  $i$ . The  $\Omega$  is the volume of the unit cell and exists in the equation (3.6) due to normalization in the unit cell. Plane waves are periodic and thus the problem divides very naturally into k-points by using the Bloch's theorem (3.1). This can be done by expanding the function  $u_i(\mathbf{r})$  in the eq. (3.1) into Fourier series, which gives

$$u_i(\mathbf{r}) = \sum_G c_{iG} \exp(i\mathbf{G} \cdot \mathbf{r}). \quad (3.7)$$

By substituting this to eq. (3.1), one immediately gets eq. (3.6) with  $\mathbf{q} = \mathbf{G} + \mathbf{k}$ .

By plugging these plane-wave expanded KS orbitals to the KS single particle equations and operating with  $\langle \mathbf{G}' + \mathbf{k} |$  from the left yields

$$\sum_G \langle \mathbf{G}' + \mathbf{k} | -\frac{1}{2} \nabla^2 + V_s(\mathbf{r}) | \mathbf{G} + \mathbf{k} \rangle c_{i\mathbf{G}+\mathbf{k}} = \varepsilon_i(\mathbf{k}) c_{i\mathbf{G}'+\mathbf{k}}, \quad (3.8)$$

in which  $-\frac{1}{2} \nabla^2$  is the single particle kinetic energy operator and  $V_s(\mathbf{r})$  is the effective single particle potential. By directly evaluating the kinetic energy term and by plane-wave expanding the effective potential as

$$V_s(\mathbf{r}) = \sum_{\mathbf{G}} \tilde{V}_s(\mathbf{G}) \exp(i\mathbf{G} \cdot \mathbf{r}), \quad (3.9)$$

one finally arrives to the effective single-particle Schrödinger equation (3.8) in the form

$$\sum_{\mathbf{G}'} \left( \frac{1}{2} |\mathbf{G} + \mathbf{k}|^2 \delta_{\mathbf{G}'+\mathbf{k}, \mathbf{G}+\mathbf{k}} + \tilde{V}_s(\mathbf{G} - \mathbf{G}') \right) c_{i, \mathbf{G}'}(\mathbf{k}) = \varepsilon_i(\mathbf{k}) c_{i, \mathbf{G}}(\mathbf{k}), \quad (3.10)$$

in which  $\tilde{V}_s$  is the Fourier transform of the effective potential. Note that there is a separate equation for every  $\mathbf{k}$ -point and the amount of terms on the left hand side depends on the number of terms in the expansion of (3.7).

Now, the real space density is available via eqs. (3.3) and (3.5). However, in a practical calculation, the total energy can be calculated directly from the Fourier transformed quantities by the expression

$$\begin{aligned} \tilde{E} = & \frac{1}{N_k} \sum_{\mathbf{k}, i} w_{k,i} \varepsilon_i(\mathbf{k}) + \sum_{\mathbf{G}} [\epsilon_{\text{XC}}(\mathbf{G}) - V_{\text{XC}}(\mathbf{G})] n(\mathbf{G}) \\ & + [\gamma_{\text{Ewald}} - \frac{1}{2} 4\pi e^2 \sum_{G \neq 0} \frac{n(\mathbf{G})^2}{G^2}] + (\sum_{\kappa} \alpha_{\kappa}) \frac{N_e}{\Omega}. \end{aligned} \quad (3.11)$$

Here,  $N_k$  is the number of  $\mathbf{k}$ -points,  $w_{k,i}$  is the  $\mathbf{k}$ -point weight related to KS state  $i$  with eigen energy  $\varepsilon_i(\mathbf{k})$ . In the second term,  $n(\mathbf{G})$  and  $\epsilon_{\text{XC}}(\mathbf{G})$  are the Fourier transforms of density and the spatial XC-energy per electron, respectively. The next two terms include the Coulomb interactions whereas the last term comes from non-Coulomb contributions in a local pseudopotential calculation, with which the plane waves are typically used. In the work presented in this thesis, Vanderbilt ultrasoft pseudopotentials [104] have been used in the plane-wave calculations carried out with the Dacapo code. The pseudopotentials in general are discussed further in section 3.3.1.

### 3.2.2 Real space grids

Real space grids [76, 78, 103] are an alternative for basis functions, such as plane waves. When real space grids are used, the KS states are not expanded with help of any functions but are represented with a fine discrete 3D grid of numerical values. In fact, the entire KS Hamiltonian is applied on the grid. Thus, also the potentials and density are discretized on the grid. In practical calculations, the grid spacing is typically around 0.2 Å.

In such a calculation, the integrals become point by point summations on the grid. For example, for a local potential operator

$$\int V(\mathbf{r})n(\mathbf{r})d\mathbf{r} \sim \Omega_G \sum_{\mathbf{G}} V(\mathbf{G})n(\mathbf{G}), \quad (3.12)$$

in which  $V(\mathbf{r})$  and  $\psi_i(\mathbf{r})$  are the continuous potential and wave function in real space whereas  $V(\mathbf{G})$  and  $\psi_i(\mathbf{G})$  are the corresponding quantities discretized on a real space grid defined by a discrete set of  $\mathbf{G} = (G_x, G_y, G_z)$  vectors, and  $\Omega_G$  is the volume per grid point. Note that here the  $\mathbf{G}$  vectors have nothing to do with the similarly denoted vectors in the context of plane wave basis (see eqs. (3.7-3.10)). However, this notation is used as it is the usual convention in the literature.

In the grid formalism, the Laplacian in the Hamiltonian is usually represented as an  $m^{th}$  order finite difference approximation

$$\left[ \frac{\partial^2 \psi_i(\mathbf{r})}{\partial x^2} \right]_{x,y,z} \sim \sum_{-m}^m C_m \psi(G_x + mh, G_y, G_z). \quad (3.13)$$

In this example, the  $2^{nd}$  order partial derivative is taken with respect to  $x$  component of  $\mathbf{r} = (x, y, z)$  only. The  $\mathbf{G} = (G_x, G_y, G_z)$  is the corresponding point on the real space grid and  $h$  is the grid spacing. The  $m$  is an integer, which determines how many grid points are used for the approximation and  $C_m$  are grid dependent coefficients.

In principle, the total energy of a DFT calculation in the grid formalism can be written as follows

$$\begin{aligned} E = & \sum_n f_n \Omega_G \sum_{\mathbf{G}} \psi_n^*(\mathbf{G}) \sum_{\mathbf{G}'} \left( -\frac{1}{2} L_{\mathbf{G}\mathbf{G}'} \right) \psi_n(\mathbf{G}') \\ & + \frac{1}{2} \Omega_G \sum_{\mathbf{G}} V_H(\mathbf{G})n(\mathbf{G}) + E_{XC}[n(\mathbf{G}), \Omega_G] + E_{II}, \end{aligned} \quad (3.14)$$

where  $f_n$  is the occupation of the state  $\psi_n$ ,  $L_{\mathbf{G}\mathbf{G}'}$  is the finite difference presentation of the Laplacian on the grid and  $E_{XC}[n(\mathbf{G}), \Omega_G]$  is a grid implementation of the exchange and correlation energy functional. The last term,  $E_{II}$ , is the interaction energy of the nuclei.

In contrast to the plane wave basis calculations, a real space grid calculation does not need to be periodic. However, when describing surfaces, this is very often desirable -

at least, in the surface plane. In such a case, the Bloch's theorem is not used in its form (3.1). Instead, the Bloch's boundary conditions (3.2) are applied to the states in the KS equations. Thus, a separate set of KS equations is obtained for every k-point, but they differ from each other only by their boundary conditions [76].

### 3.3 Towards smoother valence states

The Kohn Sham single particle states have fast varying nodal structure near the nuclei. Thus, a large number of planewaves or a very finely discretized real space grid is needed to describe the states properly. This, in turn, leads to high computational cost. Fortunately, this problem can be avoided by applying pseudopotential (PP) or projector augmented wave formalism (PAW), which are described in the following sections. The aim of the both methods is to reconstruct the problem so that the KS equations can be solved with smoother states, which can be represented with smaller number of plane waves or coarser real space grids than the original states. In this thesis, the calculations carried out with the Dacapo code [75] have been done by applying the Vanderbilt ultrasoft pseudopotentials (USPP) and plane wave basis whereas the calculations done with GPAW [76] are based on PAW formalism and real space grids.

#### 3.3.1 Pseudopotentials

The pseudopotential formalism [78, 104, 105, 106] is based on the knowledge that in practice, the most strongly bound states, *i.e.* the core states, do not interact much with the weaker bound valence states, although the valence states must be orthogonal to the core states. Furthermore, the core states stay essentially unchanged in the different chemical environments and the valence electrons are behind the chemistry. This physical fact gives a possibility to combine the effect of the nuclei and core electrons to element dependent pseudopotentials experienced by the valence electrons. Pseudopotentials are not unique and thus there exists freedom to select them so that the size of the plane wave basis can be minimized.

Traditionally, the pseudopotentials should fulfill the following properties [78, 106]:

- i) A pseudo wave function must be equal to a single particle wave function from an all-electron calculation beyond a chosen cut off radius.
- ii) The charge enclosed by a sphere with the radius equal to the cut off must be same with the pseudo and all-electron calculation single particle wave functions. This is also-called the norm conservation.

iii) The eigenvalues of the pseudo and all-electron calculation single particle wave functions must be the same.

iv) The scattering properties of the potentials should be equal.

In practice, the pseudopotentials are created with a selected scheme with the help of an all-electron Kohn Sham calculation. The all-electron calculation provides the all-electron single particle wave functions. For example, in the scheme of Troullier and Martins [106], first, the pseudo wave functions are created from the full wave functions by replacing the region inside the cut off radius by a parametrized analytical function. The parameters are optimized so that the conditions above are fulfilled and the wave functions are as smooth as possible. Then, the pseudopotentials can be solved from the known pseudo wave functions by inversion of the Schrödinger equation. This leads to a potential which depends on the angular momentum character of the pseudo-wavefunction and is thus non-local in its nature.

However, in this approach, the norm-conservation requirement (ii) has caused difficulties in creating smoother pseudopotential than the original effective single particle potential for the elements having valence states in the beginning of an atomic shell. One example is oxygen and its 2p states. To solve this problem, Vanderbilt created a scheme in which the norm-conservation is not required. This leads to the so-called Vanderbilt ultra-soft pseudo potentials [104, 105] where also the problematic cases, such as oxygen, can be described with a reasonable small plane-wave basis. In this thesis, all the Dacapo calculations are carried out by using the Vanderbilt ultra-soft pseudopotentials.

In this formalism, the pseudopotential can be written as a sum of the local and non-local parts as follows

$$\hat{V}_{\text{USPP}} = V_L + \sum_{i,j} V_{i,j} |\beta_j\rangle \langle \beta_i|, \quad (3.15)$$

in which  $V_L$  is the local part and the latter term is the non-local part including the  $\beta_i$  projectors localized to the core regions of atoms. The  $V_{i,j}$  is defined as

$$V_{i,j} = \langle \tilde{\psi}_i | \chi_j \rangle + \varepsilon_j \Delta Q_{i,j}, \quad (3.16)$$

where  $\Delta Q_{i,j}$  is the difference in the charge between the ultra-soft pseudo and norm-conserving wave function within the cut-off radius, and the functions  $\chi_i$  are defined as

$$\chi_i(\mathbf{r}) = \left\{ \varepsilon_i - \left[ -\frac{1}{2} \nabla^2 + V_L(\mathbf{r}) \right] \right\} \tilde{\psi}_i(\mathbf{r}). \quad (3.17)$$

The  $\beta_i$  projectors probe the angular momentum character of the states. Thus, the states with different angular momentum character experience different potentials. The projectors are of the form

$$\beta_i = \sum_j \langle \tilde{\psi}_i | \chi_j \rangle^{-1} \chi_j. \quad (3.18)$$

In this formalism, the KS equations are written for the smooth pseudo wave functions in the form

$$\hat{H}|\tilde{\psi}_n\rangle = \varepsilon_n \hat{S}|\tilde{\psi}_n\rangle, \quad (3.19)$$

in which the Hamiltonian includes the ultrasoft pseudopotential operator (3.15) and  $\hat{S}$  is an overlap operator of the form

$$\hat{S} = \hat{1} + \sum_{i,j} \Delta Q_{i,j} |\beta_i\rangle \langle \beta_j|. \quad (3.20)$$

The valence density is of the form

$$n_v(\mathbf{r}) = \sum_i^{\text{occ}} \tilde{\psi}_i^*(\mathbf{r}) \tilde{\psi}_i(\mathbf{r}) + \sum_{i,j} \rho_{i,j} \Delta Q_{i,j}(\mathbf{r}), \quad (3.21)$$

where

$$\rho_{i,j} = \sum_i^{\text{occ}} \langle \tilde{\psi}_i | \beta_j \rangle \langle \beta_i | \tilde{\psi}_i \rangle. \quad (3.22)$$

The total energy is obtained via

$$E = \sum_i^{\text{occ}} \langle \tilde{\psi}_i | -\frac{1}{2} \nabla^2 + \hat{V}_{\text{USPP}} | \tilde{\psi}_i \rangle + V_H[n_v] + E_{II} + E_{\text{XC}}[n_v], \quad (3.23)$$

where the ordinary functionals have been applied only to valence density and the kinetic energy and pseudopotential operators operate to the smooth valence states. Note that this energy is only a pseudo energy of the valence electrons experiencing the pseudopotential and does not have physical meaning as such. However, the energy differences have the same physical meaning as in the all-electron calculations.

### 3.3.2 Projector augmented wave method

Here, some main ideas of the PAW formalism are given. For further details, I recommend to read the original papers [105, 107, 108] and material provided by the GPAW developers [76, 109].

In the USPP method, the smoother states were obtained by searching a smoother potential which gives the desired properties for the states. In contrast, PAW formalism does not approach the problem via direct modification of the potential. Instead, the projector augmented wave method (PAW) relies on the existence of linear transformation  $\hat{T}$  from an auxiliary smooth wave function  $|\tilde{\psi}_n\rangle$  to the true all-electron Kohn-Sham single particle wave function  $|\psi_n\rangle$

$$|\psi_n\rangle = \hat{T}|\tilde{\psi}_n\rangle. \quad (3.24)$$

In this formalism, the KS equations transform formally to

$$\hat{T}^\dagger \hat{H} \hat{T} |\tilde{\psi}_n\rangle = \varepsilon_n \hat{T}^\dagger \hat{T} |\tilde{\psi}_n\rangle. \quad (3.25)$$

The transformation  $\hat{T}$  must be defined in a way that it gives as smooth  $|\tilde{\psi}_n\rangle$  as possible. In this, one can take advantage of the fact that the true KS states  $|\psi_n\rangle$  are smooth beyond a certain radius from the nuclei. Thus, the transformation  $\hat{T}$  should affect the  $|\tilde{\psi}_n\rangle$  only within this cut-off radius. This can be done by writing

$$\hat{T} = 1 + \sum_a \hat{T}^a, \quad (3.26)$$

in which the transformation  $\hat{T}^a$  is centered to nucleus with index  $a$  and is effective only within a so-called augmentation sphere with a cut-off radius  $r_c^a$  around the nucleus  $a$ .

Inside the augmentation spheres, the wave functions can be expanded in partial waves  $\varphi_i^a$ . Also for those, the corresponding smooth functions  $\tilde{\varphi}_i^a$  can be defined so that

$$|\varphi_i^a\rangle = (1 + \hat{T}^a)|\tilde{\varphi}_i^a\rangle \Leftrightarrow \hat{T}^a|\tilde{\varphi}_i^a\rangle = |\varphi_i^a\rangle - |\tilde{\varphi}_i^a\rangle, \forall i, a. \quad (3.27)$$

If the full and smooth partial waves are known, the latter form defines the operator  $\hat{T}^a$ .

Inside an augmentation sphere  $a$ , the smooth wave function  $\tilde{\psi}$ , and thus the non-smooth  $\psi$ , can be expanded with the help of the smooth and non-smooth partial waves, respectively

$$|\tilde{\psi}_n\rangle = \sum_i P_{ni}^a |\tilde{\varphi}_i^a\rangle, \quad (3.28)$$

$$|\psi_n\rangle = \hat{T}|\tilde{\psi}_n\rangle = \sum_i P_{ni}^a |\varphi_i^a\rangle, \quad (3.29)$$

as far as the smooth partial waves form a complete set inside the selected augmentation sphere. The expansion coefficients  $P_{ni}^a$  can be written with the help of the so-called smooth projector functions  $|\tilde{p}_i^a\rangle$  as follows

$$P_{ni}^a = \langle \tilde{p}_i^a | \tilde{\psi}_n \rangle. \quad (3.30)$$

If the augmentation spheres do no overlap, the expansion of a smooth wave  $\tilde{\psi}_n$  by using the partial waves centered to one augmentation sphere only should be equal to the smooth wave function itself inside this sphere. This simple condition reveals an important property of the projector functions,

$$|\tilde{\psi}_n\rangle = \sum_i |\tilde{\varphi}_i^a\rangle \langle \tilde{p}_i^a | \tilde{\psi}_n \rangle \Leftrightarrow \sum_i |\tilde{\varphi}_i^a\rangle \langle \tilde{p}_i^a | = 1, \quad (3.31)$$

which they must satisfy inside all the augmentation spheres.

By adding a unity operator written with the help of (3.31) to the definition of the atom-centered transformation operator (3.27), one ends up with

$$\hat{T}^a = \sum_i \hat{T}^a |\tilde{\varphi}_i^a\rangle \langle \tilde{p}_i^a | = \sum_i (|\varphi_i^a\rangle - |\tilde{\varphi}_i^a\rangle) \langle \tilde{p}_i^a | \quad (3.32)$$

and thus the full operator is



$$\hat{T} = 1 + \sum_a \sum_i (|\varphi_i^a\rangle - |\tilde{\varphi}_i^a\rangle) \langle \tilde{p}_i^a|. \quad (3.33)$$

In principle, defining a PAW transformation means choosing the sets of partial waves, smooth partial waves and the projector functions. These should be chosen so that the solutions of the transformed eigenvalue equation (3.25) are as smooth as possible. On the other hand, as few as possible terms should be needed in the partial wave expansions. In other words, the problem should be made as numerically convenient as possible. Note that, the condition of eq. (3.31) must hold anyway. The partial waves and projectors are system independent and can be stored in a database for the elements of the periodic table.

In the GPAW code, the partial waves are solutions of the Schrödinger equation of the corresponding spin-paired separated atoms. The smooth partial waves are equal to those outside the augmentation spheres, whereas inside the spheres, they are 6th order polynomial continuations for the atomic solutions. The projectors are calculated from the smooth partial waves as follows

$$|\tilde{p}_i^a\rangle = (-\frac{1}{2}\nabla^2 + \tilde{v}_s - \varepsilon_i) |\tilde{\varphi}_i^a\rangle, \quad (3.34)$$

in which the  $\tilde{v}_s$  is the so-called smooth KS potential.

In the previous formulation, all the electrons are still explicitly included in the calculation. To reduce the computational cost further, the states of the chemically inactive core electrons can be considered unchanged upon the interactions between the valence electrons. This is called the frozen core approximation. In the PAW formalism, this is done simply by taking the core states to be the atomic KS states localized to the augmentation spheres. Furthermore, these states are excluded from the partial wave expansions of  $|\psi_n\rangle$  and  $|\tilde{\psi}_n\rangle$ .

Formally, the density is given in this formalism by

$$n(\mathbf{r}) = \sum_n^{\text{val}} f_n |\tilde{\psi}_n|^2 + \sum_a \sum_{i_1 i_2} (\varphi_{i_1}^a \varphi_{i_2}^a - \tilde{\varphi}_{i_1}^a \tilde{\varphi}_{i_2}^a) D_{i_1 i_2}^a + \sum_a \sum_{\alpha}^{\text{core}} |\varphi_{\alpha}^{a, \text{core}}|^2, \quad (3.35)$$

in which

$$D_{i_1 i_2}^a = \sum_n f_n P_{ni_1}^{a*} P_{ni_2}^a \quad (3.36)$$

is Hermitian one-center density matrix.

The first term of eq. (3.35) includes the density carried by the smooth eigen states of the transformed KS equations (3.25), whereas the second one brings in the non-smooth valence contribution localized to the augmentation spheres. The third term adds the density of the frozen core electrons. Note that, the second term can be calculated from the smooth states by using the pre-defined partial waves and projector functions. The third term needs only the atomic solutions for the core states.

Finally, the total energy of the system can be written as a sum of the contributions of the smooth quantities and the non smooth parts located to the augmentation spheres as follows

$$E = \tilde{E} + \sum_a \Delta E^a, \quad (3.37)$$

where

$$\tilde{E} = T_s[\{\tilde{\psi}\}] + V_H[\tilde{\rho}] + E_{XC}[\tilde{n}], \quad (3.38)$$

in which  $\tilde{n}$  is the smooth part of the density and  $\tilde{\rho}$  is a smooth density neutralized with compensation charges, and

$$\begin{aligned} \Delta E^a = & \Delta T_c^a + \Delta C^a + \sum_{i_1 i_2} (\Delta T_{i_1 i_2}^a + \Delta C_{i_1 i_2}^a) \\ & + \sum_{i_1 i_2 i_3 i_4} D_{i_1 i_2}^{a*} \Delta C_{i_1 i_2 i_3 i_4}^a D_{i_3 i_4}^a + \Delta E_{XC}^a[\{D_{i_1 i_2}^a\}]. \end{aligned} \quad (3.39)$$

Here,  $D_{i_1 i_2}^a$  is the one density matrix of eq. (3.36) carrying information of the density inside the augmentation spheres as transformed from the smooth states whereas  $T_c^a$ ,  $\Delta T_{i_1 i_2}^a$ ,  $\Delta C_{i_1 i_2}^a$  and  $\Delta C_{i_1 i_2 i_3 i_4}^a$  are system independent tensors. The tensors need to be calculated only once and stored for every element of the periodic table to the PAW setup files.

## 4 The methods of analysis

The two main quantities provided by a DFT calculation are the total ground state energy of the system and the corresponding ground state electron density. These would be exact quantum mechanical many body solutions if one had the exact XC functional. The same is true with all the quantities derived directly from those, *i.e.*, adsorption energies, reaction barriers, reaction induced density differences *etc.* In addition, in the usual BO approximation, DFT gives also the ground state atomic structures. Accuracy of those is determined by the quality of the XC functional and the applicability of the BO approximation itself. Furthermore, the KS approach gives a possibility to use the KS single particle states in semi quantitative or qualitative analysis of the system. In a weakly correlated system, the many electron wave function is well described by a single Slater determinant consisting of single particle states, like in the HF approximation. The KS wave functions, as well as their energies and state densities, can often be used similarly to HF states when analyzing the chemistry. However, it should be kept in mind that KS wave functions are the states of an auxiliary non-interacting system in an effective potential. Thus, even if the XC functional was exact, the KS states would not be equal to the HF states of the system. Typically, the energy range of the KS states is narrower than the one of the HF states, although their symmetry and nodal character is similar [83, 110, 111, 112]. In the following sections, the analysis methods used in this thesis are discussed in more detail.

### 4.1 Changes in the total energy

The energy differences upon structure changes have often important physical meaning. In general, they are calculated in the form

$$E_{\text{change}} = E(\text{final}) - E(\text{initial}). \quad (4.1)$$

For example, adsorption energy,  $E_{\text{ads}}$ , is a measure of the adsorption strength. It tells how much the total energy of a system is changed when an isolated gas-phase species is adsorbed on a surface. In such a case,  $E(\text{final})$  is the energy of a system in which the adsorbate is on the surface,  $E(\text{ads/surface})$ , whereas  $E(\text{initial})$  is the sum of the total energies of the separate surface,  $E(\text{surface})$ , and adsorbate,  $E(\text{ads})$ , systems. The equation becomes into the form

$$E_{\text{ads}} = E(\text{ads/surface}) - E(\text{ads}) - E(\text{surface}). \quad (4.2)$$

In this definition, negative sign means exothermic reaction and thus favorable adsorption. Note that an opposite sign convention is some times used in literature (for example in paper [IV]).

Another yet informative quantity is the formation energy,  $E_{\text{for}}$ . It shows how much the total energy of a system is changed, if a species is formed from isolated gas-phase atoms. For example, the formation energy of  $N$  atom Au cluster in gas-phase can be written as follows,

$$E_{\text{for}}^{\text{gas}}(N) = E(\text{Au}_N) - N * E(\text{Au}), \quad (4.3)$$

where  $E(\text{Au}_N)$  is the total energy of  $N$  atom Au cluster whereas  $E(\text{Au})$  is the energy of a Au atom. This is a measure of the stability of the cluster, which often depends on its size. The stability of the species on a surface can be calculated in a similar way. The surface formation energy of  $N$  atom Au cluster from separated gas-phase atoms is

$$E_{\text{for}}^{\text{surf}}(N) = E(\text{Au}_N/\text{surface}) - N * E(\text{Au}) - E(\text{surface}), \quad (4.4)$$

where  $E(\text{Au}_N/\text{surface})$  is the energy of the system in which the cluster is on the surface. Formation energies are often normalized with the cluster size  $N$ , when the stabilities of different sized species can be directly compared, either in gas-phase or on a surface.

Of course, the energy change does not need to be related solely to structural changes. An important and often quite characteristic quantity associated to a certain metal cluster size is its electron affinity. The  $n^{\text{th}}$  adiabatic electron affinity of  $N$  atom gold cluster can be defined as

$$E_{\text{aff}}^{n^{\text{th}}}(N) = E(\text{Au}_N^{(n-1)-}) - E(\text{Au}_N^{n-}), \quad (4.5)$$

where  $E(\text{Au}_N^{(n-1)-})$  is the energy of  $N$  atom Au cluster with net charge  $n - 1$   $|e|$  and  $E(\text{Au}_N^{n-})$  is the energy of the same species with one electron more. Electron affinity measures how favorable it is to attach an extra electron to a neutral or an already charged species. Note that the charging can be accompanied by structural changes, the energetic contributions of which are included in the adiabatic electron affinity. The sign convention of electron affinity is selected so that a positive value corresponds to favorable electron attachment.

## 4.2 Density difference due to adsorption

Density difference analysis provides one way to visualize the redistribution of electrons due to adsorption. The density difference would be an exact difference in the quantum mechanical many body density if the XC functional was exact. A density difference array is obtained by calculating

$$n_{\text{diff}} = n(\text{species/surface}) - (n(\text{species}) + n(\text{surface})). \quad (4.6)$$

In this  $n(\text{species})$  is the electron density of the isolated species to be adsorbed,  $n(\text{surface})$  is the ground state electron density of the surface without adsorbate and  $n(\text{species/surface})$  is the ground state density of the combined system. Both the isolated subsystems are calculated in the interaction geometry of the combined system. The geometric shape of the electron difference can give a hint from which to which states the electrons are transferred upon the adsorption. Often, the density difference is integrated over the (x,y) plane parallel to surface and thus given as a function of the (z) coordinate perpendicular to the surface.

$$n_{\text{diff}}(z) = \int_x \int_y n_{\text{diff}} dx dy. \quad (4.7)$$

In this thesis, such a function has been used to show the polarization and charge transfer phenomena in layered adsorbate and surface structures (see fig. 6.6).

## 4.3 Bader charge analysis

The traditional chemical picture relies often to the concepts of charge donation and acception between the species forming a bond. The extreme case is the ionic bond, in which electrons are considered to swap the nucleus so that both the species reach the octet, if possible. A DFT calculation provides the electron density, which would be exact density of the quantum mechanical many body system if the XC functional was exact. Thus, in principle, electron transfer phenomena could be detected by analyzing the density from a DFT calculation.

However, there is no unambiguous way to define, which electron belongs to which nuclei in a quantum mechanical many body system. For example, in the Voronoi method, the density is simply assigned to a nearest nucleus in space. In the Mulliken population analysis, the density is shared according to the weights of atom centered

basis functions. In the electrostatic potential (ESP) methods, a group of point charges, located to nuclei, is searched, which gives the same electrostatic potential with the original electron density.

Probably the method, which fits best to the chemical intuition, is the Bader charge analysis. In this method, the so-called zero flux surfaces of the density are searched. These are the surfaces in space on which the gradient of the density does not have component along the surface normal, *i.e.*, all the surface points satisfy the condition

$$\nabla n(\mathbf{r}) \cdot \mathbf{u}_n(\mathbf{r}) = 0, \quad (4.8)$$

in which  $\mathbf{u}_n(\mathbf{r})$  is the unit vector along the surface normal at point  $\mathbf{r}$ . In other words, these are surfaces consisting of local density minima around nuclei. The volume enclosed by such a surface is called a Bader region. A Bader charge of an atom is the charge integrated over the Bader region in which the corresponding nucleus is located. The main strengths of the Bader method are its adaptivity to the exact topology of the density and its independentness of the basis set used.

Within the work presented in this thesis, the Bader method has been used mainly to determine the charge states of surface adsorbates. The analysis has been carried out as implemented in the refs. [113, 114, 115]. In selected cases, it has been compared to the Voronoi method and found to be superior to that. In GPAW calculations, the full electron density (see eq. (3.35)) is used as an input for the analysis. In Dacapo calculations, only the pseudodensity (see eq. (3.21)) is analyzed. The results are still very comparable. For example, the difference in the charge state of Au<sub>6</sub> cluster on 3 layer MgO film on Mo metal between GPAW and Dacapo calculations is only 0.03 electrons. All the charges presented in this thesis are calculated with Bader analysis.

## 4.4 Kohn-Sham states and their density

In the HF method, the many-body wave function of the system is approximated with a Slater determinant consisting of single particle wave functions. These are the HF orbitals that quantum chemists typically use for making chemical interpretations of the systems. In contrast, DFT does not provide these orbitals as output. Instead, the KS orbitals are obtained from the calculation. These are the orbitals of the auxiliary single particles reproducing the density of the many-body system in the effective potential. Thus, even if the XC functional was exact, the KS orbitals are not an approximation for the HF orbitals. This, however, does not mean that they would be useless. In fact, whereas the Slater determinant of the HF states is just a well defined single particle *approximation* for the full many-body wavefunction, the ideal KS states

are an *exact* mapping from a true quantum mechanical many body system to a single particle system and *vice versa*. Typically the KS states show the similar intuitive chemistry than the HF states, although they lie in a narrower energy window. For example, in this thesis, the properties of O<sub>2</sub> molecule on a thin-film is analyzed with the help of KS orbitals (see fig. 6.7).

Often, the density of KS states is used for analysis. The density of states (DOS) in a system with eigenstates  $\psi_n$  and corresponding energies  $\varepsilon_n$  is defined as

$$\rho(\varepsilon) = \sum_n \langle \psi_n | \psi_n \rangle \delta(\varepsilon - \varepsilon_n). \quad (4.9)$$

It is a measure of number of states having the energy  $\varepsilon$ . Thus, by integrating it, one gets the number of particles in a chosen energy range  $[\varepsilon_1, \varepsilon_2]$  as follows

$$N(\varepsilon_1, \varepsilon_2) = \int_{\varepsilon_1}^{\varepsilon_2} d\varepsilon n_F(\varepsilon) \rho(\varepsilon). \quad (4.10)$$

Often, more informative quantities are the projected and local density of states (PDOS and LDOS). In PDOS, the states are projected to a some selected complete and orthogonal set of states, like atomic orbitals. Thus, the spectral contribution of a selected state  $|i\rangle$  to the total density of states can be written as

$$\rho_i(\varepsilon) = \sum_n \langle \psi_n | i \rangle \langle i | \psi_n \rangle \delta(\varepsilon - \varepsilon_n). \quad (4.11)$$

In LDOS, this basis is selected to be the spatial basis. Formally in the very similar way one gets

$$\rho(\mathbf{r}, \varepsilon) = \sum_n \langle \psi_n | r \rangle \langle r | \psi_n \rangle \delta(\varepsilon - \varepsilon_n). \quad (4.12)$$

In the DFT calculations the states  $\psi_n$  are always the KS states  $\phi_n$  and thus the DOS analysis is done for the auxiliary single electron system. As a consequence, even if one had an exact XC functional, a PDOS spectrum from DFT should not be rigorously considered as a single electron approximation of the state density, as it is in the HF method. However, for example, comparison of Au cluster PDOSes to experimental photo electron spectra (PES), show that they are qualitatively very similar [4]. In this thesis, PDOS analyses have been used for example to analyze the O<sub>2</sub> interaction with gold clusters (see fig. 6.27).





# 5 Simulating STM

## 5.1 The Tersoff-Hamann approach

Probably the most used method to simulate STM images is the Tersoff-Hamann approach [116, 117, 118, 119]. It is based on the tunneling model by Bardeen [120], in which the solution for the Schrödinger equation is assumed to be known for two separate subsystems, the tip and the sample. The tunneling through a potential barrier between the known tip ( $\psi_T$ ) and the sample state ( $\psi_S$ ), with energies  $E_{\psi_T}$  and  $E_{\psi_S}$ , is treated with the time dependent perturbation theory leading to a tunneling probability of the form

$$P = \frac{2\pi}{\hbar} |M|^2 \delta(E_{\psi_S} - E_{\psi_T}), \quad (5.1)$$

in which the tunneling matrix element is

$$M = \frac{\hbar}{2\pi} \int_{z=z_0} (\psi_T^* \frac{\partial \psi_S}{\partial z} - \psi_S^* \frac{\partial \psi_T}{\partial z}) dS, \quad (5.2)$$

where the surface integral is carried out on a plane ( $z = z_0$ ) inside the barrier region (see fig. 5.1).

Tersoff and Hamann made a further approximation in which the tip is modeled as a spherical potential well. In their original work, only the s-wave solution of the tip was considered as important [116, 117]. Under such a condition, if a low bias voltage  $V_{\text{bias}}$  is assumed, the tunneling current at the tip apex located to point  $\mathbf{r}$  gets a simple form

$$I(\mathbf{r}, V_{\text{bias}}) \propto \int_{E_F - |eV_{\text{bias}}|}^{E_F} |\psi_S(\mathbf{r}, E_n)|^2 dE_n =: n(\mathbf{r}, V_{\text{bias}}), \quad (5.3)$$

where  $\psi_S(\mathbf{r}, E_n)$  is the sample state with energy  $E_n$  and  $E_F$  is the Fermi energy up to which the states are occupied. In other words, the STM signal is proportional to the local density of states integrated over the narrow energy window determined by the bias voltage  $V_{\text{bias}}$ . Eq. (5.3) holds for occupied states as only the wave functions with

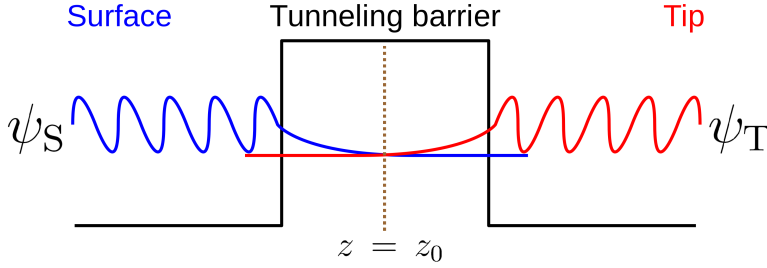


**Figure 5.1:** The setup of the Bardeen tunneling model. The surface state is visualized with a blue wave whereas the tip state is the red one. The potential barrier for tunneling is drawn in black. The integral plane for the Bardeen integral of eq. (5.2) at  $z=z_0$  is marked with the dashed line.

energies lower than the Fermi energy,  $E_F$ , are included to the integral. For unoccupied states, the integral is taken from  $E_F$  to  $E_F + |eV_{\text{bias}}|$ . In the usual convention, the Fermi energy is taken at zero and the negative bias corresponds to positive tip and thus probing of the occupied states of the sample. Similarly, positive bias corresponds to negative tip and probing of the unoccupied sample states.

## 5.2 Connecting the density and the current

However, in ref. [118], even a simpler approximation has been done. If one assumes roughly that i) both, the tip and surface states decay like the states of a metal surface with a work function  $\Phi$ , ii) the first term in the Bardeen integral (5.2) is of the same magnitude as the difference of the two terms and iii) in the first term, the surface and tip states can be roughly approximated to be similar, *i.e.*,  $\psi_T \approx \psi_S$ , the tunneling current reduces to a Tersoff-Hamann-like form, which relates the current and the density in the bias window by

$$I(\mathbf{r}, V_{\text{bias}}) \propto \Delta S^2 k^2 n(\mathbf{r}, V_{\text{bias}})^2, \quad (5.4)$$

in which  $\Delta S$  is the area of the wave function overlap and  $k = \sqrt{2\Phi}$  is the decay length of the states. If one further approximates that iv) the tunneling cross section is about 2 Å and the work function  $\phi$  is around 4 eV, and an appropriate factor of proportionality is added, one ends up to an equation connecting the state density in the bias window and the corresponding tunneling current as follows

$$n(\mathbf{r}, V_{\text{bias}}) \approx 2 \times 10^{-4} \sqrt{I(\mathbf{r}, V_{\text{bias}})}, \quad (5.5)$$

in which the unit of density is  $\text{\AA}^{-3}$  and the current is in  $nA$ .

### 5.3 Constant-current mode

STM measurements are typically carried out in the constant-current mode. This means, that the tip scans the surface (x,y-coordinates) and adjusts the surface-tip distance (z-coordinate) so that the tunneling current retains a constant value for every (x,y) with the applied bias voltage. From the surface-tip distance,  $\Delta z$ , one can draw a map as a function of x and y, which is the topographic STM image. A schematic two dimensional presentation of the process is given in fig. 5.2. In the Tersoff-Hamann formalism, this corresponds to a mapping of a constant local density of states surface with given density and bias voltage values. When comparing to experimental images, a rough connection between the current and density can be done by applying eq. (5.5).

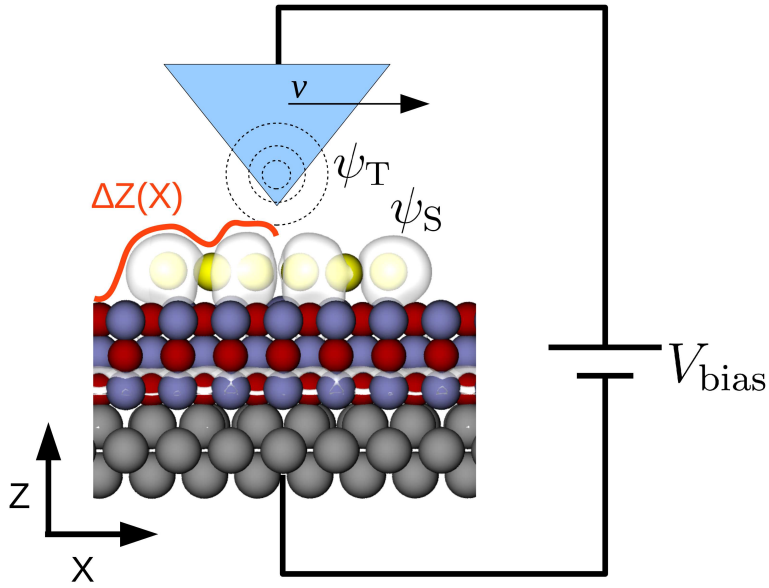


**Figure 5.2:** A two dimensional schematic presentation of STM operating in constant-current mode. Here, the image is taken of a gold cluster (yellow spheres) on MgO/Mo. The Mg atoms are blue, O atoms red and Mo atoms grey. One constant density surface of the (KS) electron state of the cluster is drawn with translucent grey color. The tip moves along the x-direction and follows the (orange) constant-current contour  $Z(X)$ , as the surface state (translucent grey) and the tip state (dashed circles) interacts. The bias voltage determines whether the tunneling takes place from occupied surface states to the tip states, or from tip states to the empty surface states.

## 5.4 Applying to periodic DFT calculations

When applied to DFT calculations, the single particle wave functions are taken to be the KS states [118]. Furthermore, in the Dacapo and GPAW surface calculations presented in this thesis, periodic boundary conditions have been applied. Thus, the relation for  $n(\mathbf{r}, V_{\text{bias}})$  obtains a form

$$n(\mathbf{r}, V_{\text{bias}}) = \frac{1}{N_k} \sum_{\mathbf{k}, i}^{\varepsilon_i \in \text{bias}} f(\varepsilon_i(\mathbf{k})) n_{i,\mathbf{k}}(\mathbf{r}) \quad (5.6)$$

for occupied states and

$$n(\mathbf{r}, V_{\text{bias}}) = \frac{1}{N_k} \sum_{\mathbf{k}, i}^{\varepsilon_i \in \text{bias}} (1 - f(\varepsilon_i(\mathbf{k}))) n_{i,\mathbf{k}}(\mathbf{r}) \quad (5.7)$$

for unoccupied states, in both of which

$$n_{i,\mathbf{k}}(\mathbf{r}) = |\phi_{i,\mathbf{k}}(\mathbf{r})|^2 \quad (5.8)$$

is the part-density carried by the KS state  $i$  at  $\mathbf{k}$ -point  $\mathbf{k}$ .

## 5.5 Applying to USPP and PAW formalisms

In the Dacapo calculations, Vanderbilt ultrasoft pseudopotentials have been applied. In the STM images simulated from these calculations, the density has been approximated with the pseudo valence states only, *i.e.*,

$$n_{i,\mathbf{k}}(\mathbf{r}) \approx |\tilde{\phi}_{i,\mathbf{k}}(\mathbf{r})|^2 \quad (5.9)$$

has been applied. In the GPAW calculations, PAW formalism has been used. In the STM images based on those calculations, a similar approximation has been made by using the smooth waves instead of the all-electron single particle states. In both cases, the approximations are valid: The pseudopotentials are constructed so that the pseudo wave functions and the all-electron single particle KS states are identical beyond a certain cut-off radius (1.21 Å for Au in the used setup) from the nucleus.

This is exactly valid in the atomic systems in which the potentials are constructed and approximately valid in any other systems. In the PAW formalism, the smooth wave functions are by definition identical to the full single particle wave functions beyond a certain cut-off radius (1.32 Å for Au in the used setup). The isovalue contours with low densities, *i.e.*, with low simulated STM currents, lie beyond this radius from the nuclei.

## 5.6 Scanning tunneling spectroscopy

In addition to the topographic constant-current imaging, scanning tunneling spectroscopy (STS) measurements are often carried out. In such a measurement, the tunneling conductance is measured as a function of the bias voltage from a selected point in space. In the experiments, the point is selected from the constant-current surface determined by a chosen tunneling current  $I$  and bias voltage  $V_{\text{bias}}$ . Then, the position of the tip is locked and the voltage is ramped. During the ramping, the voltage is modulated with a high frequency but small amplitude. This leads to modulation in the tunneling current, the amplitude of which is proportional to the tunneling conductance  $dI/dV$ . Thus, the derivative of the tunneling current  $I$  can be recorded as a function of the bias voltage  $V_{\text{bias}}$ . This quantity is proportional to the local state density of the sample and thus reveals, on which energies the electron states of the system are weighted.

A measured  $dI/dV$ -spectrum could be compared to simulated LDOS (eq. (4.12)) in the corresponding point in space. However, a different approach has been taken within this thesis: First, the point for the simulated STS has been selected by comparing the simulated and experimental constant-current images with the same appearance so that the STS point on the simulated surface looks qualitatively the same as the experimental STS point on the measured surface. Then, the simulated tunneling current is recorded from this point as a function of the bias voltage  $V_{\text{bias}}$ . From this, the  $dI/dV$ -spectrum is evaluated by taking a numerical derivative of the form

$$\frac{dI}{dV} = \frac{I(V_{\text{bias}} + \Delta V) - I(V_{\text{bias}} - \Delta V)}{2\Delta V}, \quad (5.10)$$

where  $\Delta V$  is the discrete step for the numerical derivation.

It is also possible to measure conductance- or  $dI/dV$ -maps. In those, the  $dI/dV$  is measured in all the points of the selected constant-current surface with the given bias voltage. Typically, the bias voltage is selected to match the peaks of the  $dI/dV$ -spectra of the sample. The actual tunneling conductance image consists of the  $dI/dV$  values

of the constant current surface mapped as a function of  $x$  and  $y$ . It reveals the spatial appearance of the states corresponding the peaks of the  $dI/dV$ -spectra. This can be simulated by calculating the numerical derivative of eq. (5.10) in all the points of the simulated constant-current surface.

Note that if the bias window  $[0, V_{\text{bias}}]$  (or  $[V_{\text{bias}}, 0]$ ) includes several states, the constant-current surface follows some density of their superposition. Thus, as the  $dI/dV$ -map is measured from this superposition surface, it is possible that some of the features of the state emerging at  $V_{\text{bias}}$  can not be seen in the map. Some parts of the state may be spatially weighted to regions far from the constant current surface. Even if the  $dI/dV$  value would be high in those regions, it is not seen in the values probed elsewhere, *i.e.*, on the constant current surface. Consequently, when occupied states are probed with  $dI/dV$ -mapping, the states higher in energy may distort those. Similarly, when the unoccupied states are  $dI/dV$ -mapped, the states lower in energy can distort those. Fortunately, the same phenomena exist both in the measurements and simulations, and thus, they are comparable to each other also with respect to this aspect.

## 6 Results

The main result in this thesis is the fact that the properties of small molecules, metal atoms and clusters can be different on thin oxide films supported by a carrier metal than on single crystal oxide surfaces. The adsorption energies, geometrical structures and charge states of the adsorbates depend on the substrate. These thin-film effects can be relatively long ranged: The calculations show that the adsorbates on a 10 monolayer (ML) thick film can still have different properties than on a single-crystal surface. The changes in the ground states of the adsorbates are likely to lead to different surface chemistry.

In the following sections, the main results of the publications (I-VI) are briefly discussed together with key results from literature. First, the physics behind the adsorbate charging induced by the metallic support and the followed stabilization of the adsorbate are discussed. At the beginning of the discussion, a brief summary of relevant results published before this thesis work is given. Second, the thin-film effects to Au clusters, their structures, energetics and charge states are discussed. The measurable consequences of thin-film effects in the STM images and STS spectra will be presented and rationalized with the help of a simple harmonic oscillator model. Third, the O<sub>2</sub> adsorption on thin-films and thin-film supported Au clusters is discussed. This is relevant as it is considered an important step in the catalytic CO oxidation, which itself is a relevant benchmark reaction with practical importance.

### 6.1 Thin-film effects on atoms and small molecules

#### 6.1.1 Early results

When the work presented in this thesis begun in 2006, already a few publications considering thin-film effects on metal atoms and small molecules were available in the literature, and more was coming soon. The first theoretical results [41, 42, 44] on thin-film effects on single atom adsorbates show that Au atoms with high electron affinity adsorb strongly on the MgO/Mo surface and become negatively charged. For a supported 3 ML MgO film, the adsorption energy is around -1.87 eV ([41] PW91, PWs, USPP) or -1.99 eV ([44] RPBE, PWs, USPP). This is a surprising result as on a bulk like single crystal MgO substrate, Au adsorbs weakly and is essentially

neutral [41, 42, 44, 45, 46, 47, 48, 49, 50, 51]. On an unsupported MgO film, the Au adsorption energy of -1.01 eV ([42], PW91, PWs, USPP) and -0.66 eV ([44], RPBE, PWs, USPP) have been reported. Metal atoms with lower electron affinity, like Pd, adsorb relatively weakly and stay neutral also on thin films [42]. In addition, the DFT calculations predicted that the adsorption site of the Au atom is O top on a single crystal surface whereas on a thin film, it is Mg top or a hollow site depending on the oxide film thickness [42, 44]. The hollow site seems to be the most favorable for the thinnest films of 1-4 ML [44]. Soon after the theoretical predictions, STM experiments [52] confirmed that the favored adsorption sites of Au atoms depend on the thickness of the MgO film deposited on Ag carrier metal.

Originally, the changes in the adsorption properties, and especially the charging, was analyzed with the help of spin-polarized PDOS: On a bulk like surface the Au 6s state is singly occupied by the majority spin whereas on a thin film the 6s is below the Fermi level for both spins [41, 42]. Later [44], Bader analysis was applied to confirm the charge transfer showing the anionic charge state of -0.82 |e| for Au on MgO(3ML)/Mo. In the same paper [44], it was pointed out that the charging of the adsorbate is accompanied with a polarization pattern ranging through the oxide film. The experimental support for charging has been obtained mainly via STM measurements: The pair distribution function of the Au atoms on MgO/Ag show long-range order which is a sign of lateral Coulomb interactions and thus implicates charging [53]. The distribution of Pd atoms is random, and therefore they are most likely neutral [53]. Another measurable sign of charging is that the STM images display a dark ring around an anionic atom. This was found in ref. [72] in which Au atoms on 2ML NaCl(100) supported by Cu(111) were charged by applying voltage pulses with a STM tip. After applying the pulse, STM showed a dark ring around the investigated atom. In the case of MgO/Ag substrate, the STM images display these rings around Au atoms already without any voltage pulses, which implicates that the atoms become spontaneously anionic upon adsorption [53]. In contrast, the images of Pd atoms do not have the ring. These, and some other measurable consequences of the thin-film induced changes in the adsorbate properties, as predicted by DFT, are discussed in ref. [121]. For example, work function changes, CO vibrational frequency, electric field effects and core level shifts should, in principle, carry observable information related to the adsorbate charge state on a thin film.

The first explanation for the strong adsorption on thin films was that the charged adsorbate creates an image charge to the supporting metal. The attractive interaction between the charged adsorbate and its image makes the electron transfer favorable. It was also pointed out that in the cases of MgO/Mo and MgO/Ag substrates, the work functions of the systems are lower than those of the corresponding bare metals. This also lowers the energetic price of the adsorbate charging. On the other hand, this price is also dependent on the electron affinity of the adsorbate. The high electron affinity adsorbates, like Au and Ag, become anionic whereas Pd stays essentially neutral.



### 6.1.2 A systematic study

In the work presented in this thesis, the factors behind thin-film effects have been put under a systematic study and the generality of the phenomenon has been investigated. The test adsorbates have been Au<sub>1</sub> [I, II, IV], Au<sub>3</sub> [I, II, VI], O<sub>2</sub> [VI] and NO<sub>2</sub> [IV]. As far as the substrates are concerned, the Mo, Ag, Pd, Au, and Pt carrier metals and MgO and Al<sub>2</sub>O<sub>3</sub> films of different thicknesses have been considered [IV]. In all the studied cases, the adsorption is stronger on thin-film than on single crystal. Furthermore, all these adsorbates become spontaneously charged on thin films whereas they are neutral on single crystals. The charging is shown by Bader, PDOS and KS orbital analyses. The adsorption energies and charges of the studied species, both on MgO and MgO/Mo substrates, have been collected to table 6.1.

**Table 6.1:** The adsorption energies ( $E_{\text{ads}}$ ) and Bader charges ( $q$ ) of Au<sub>1</sub>, Au<sub>3</sub>, O<sub>2</sub> and NO<sub>2</sub> on MgO and MgO/Mo. The results for Au<sub>1</sub>, Au<sub>3</sub> are obtained with Dacapo using RPBE [I,II]. The results for NO<sub>2</sub> are calculated with Dacapo using PBE [IV]. The energetics and charging for O<sub>2</sub> have been obtained with GPAW applying RPBE [VI].

Adsorbate	$E_{\text{ads}}$ MgO	$E_{\text{ads}}$ MgO/Mo	$q$ MgO	$q$ MgO/Mo
Au <sub>1</sub>	-0.66	-1.99	-0.3	-0.8
Au <sub>3</sub>	-1.15	-2.27	-0.4	-1.0
O <sub>2</sub>	-0.01	-1.51	-0.1	-1.0
NO <sub>2</sub>	-0.36	-1.68	-0.3	-0.9

In a simplified picture, the adsorption energies of these thin-film supported spontaneously charged species should depend on the following factors:

- i) Image charge and polarization interaction between the charged adsorbate and the substrate
- ii) Coulombic lateral repulsion between charged adsorbates
- iii) Work function of the substrate
- iv) Electron affinity of the adsorbate
- v) Direct bonding between the adsorbate and the oxide
- vi) Adsorption induced changes in the oxide-metal-interface

The role of the factor i), the image charge interaction and oxide polarization, have been tried to estimate with the classical continuum model by Stoneham and Tasker [40]. In their model, the classical interaction energy of a point charge  $Q$  in a system with two boundaries of three materials with dielectric constants  $\varepsilon_1$ ,  $\varepsilon_2$  and  $\varepsilon_3$  is

$$E = \frac{Q^2}{2\varepsilon_1} \int_0^\infty dk A(k) \quad (6.1)$$

when the point charge is located in the material having dielectric constant  $\varepsilon_1$  and

$$A(k) = \left( \frac{\varepsilon_1 - \varepsilon_2}{\varepsilon_1 + \varepsilon_2} \right) \exp(-2kz) + \left( \frac{2\varepsilon_1\varepsilon_2}{\varepsilon_1 + \varepsilon_2} \right) \left\{ \frac{2(\varepsilon_2 - \varepsilon_3)\exp(-2kz)}{(\varepsilon_1 + \varepsilon_2)(\varepsilon_2 + \varepsilon_3)\exp(2kL) + (\varepsilon_1 - \varepsilon_2)(\varepsilon_2 - \varepsilon_3)} \right\}, \quad (6.2)$$

in which  $L$  is the thickness of the material slab with dielectric constant  $\varepsilon_2$  and  $z$  is the distance of charge  $Q$  from the slab. Here, one is interested in the case, where the charge  $Q$  is in the vacuum, *i.e.*  $\varepsilon_1=1$ , the slab of thickness  $L$  is oxide,  $\varepsilon_2 \sim 10$ , and the underlying material is metal, for which  $\varepsilon_3 \sim 100$ . Fig. 6.1 should clarify the setup. Stoneham and Tasker (ST) developed the model in the context of metal oxidation, and indeed found that a metal support below an oxide film can increase the attraction between a point charge and the oxide film by 1.55 eV, when their distance is 2 Å.

The classical model has two important features: First, although not very transparent, the  $z$ -dependence in eqs. (6.1) and (6.2) is long ranged and thus the metal should have effect to the adsorbate properties through relatively thick films. Second, the only material parameters in the model are the dielectric constants. For metal oxides, they are typically around 10, and thus there should not be significant difference between different oxides. An exception is the  $\text{TiO}_2$ , which can be modeled with a dielectric constant around 100.

### The effect of the oxide film thickness

The effect of the oxide film thickness has been tested by calculating the DFT adsorption energy and the charge of Au atom on MgO/Mo for oxide films of different number of layers. The strength of the image charge and polarization interaction for the same film thicknesses and adsorbate charges have also been calculated with the ST model. The DFT and ST results are shown in fig. 6.2. The DFT values are given at Au coverages of 0.11 ML [44] and 0.25 ML [IV] for hollow and O-top sites. The plot shows that both the negative charging and adsorption energy of Au is stronger on thin films than on thick films. For example, at Au coverage 0.25 ML, the adsorption energy of the atom is -1.26 eV on three-layer film, whereas it is only -0.64 eV on 20 layer film. This is accompanied by the change of the charge from -0.65 |e| to -0.28 |e|. Note that the latter is already the same charge state as calculated for Au atom on

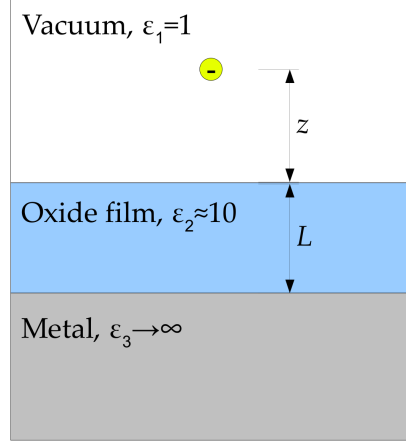


**Figure 6.1:** A schematic representation of the setup of the ST model [40] of classical electrostatics as applied in this thesis. The negative point charge (yellow circle) is in the semi-infinite vacuum with dielectric constant equal to unity. It is placed at height  $z$  above the oxide film (light blue area) of thickness  $L$  and dielectric constant  $\sim 10$ . The oxide film is on semi-infinite metal carrier (grey area), which can be described with dielectric constant approaching infinity. In practical calculations, a value around 100 is enough to capture the metallicity.

a MgO slab without any carrier metal. The energy trend predicted by the ST model is very similar to the DFT results and thus the long-ranged character of thin-film effects could be addressed to image charge and polarization interactions. Note that the results at  $\theta=0.25$  ML show that the favored adsorption site of Au changes from hollow to O-top site when the thickness of the film is increased over 10 ML (1.8 Å). The change of the adsorption site is also observed experimentally for Au on MgO/Ag. According to the STM images the change takes place between 3 to 8 oxide layers [53].

### The effect of the different oxides

According to the ST model, the image charge and polarization interactions between the charged adsorbate and the thin-film substrate should be essentially independent of the oxide type. To see, whether this is the case also in the DFT model, the adsorption energy of NO<sub>2</sub> on MgO/Mo and Al<sub>2</sub>O<sub>3</sub>/Mo have been calculated as a function of the oxide thickness. This has been compared to the adsorption energy on unsupported oxides. The difference between the adsorption energies measures the stabilization energy due to the metal support. The stabilization predicted, both, with DFT and ST

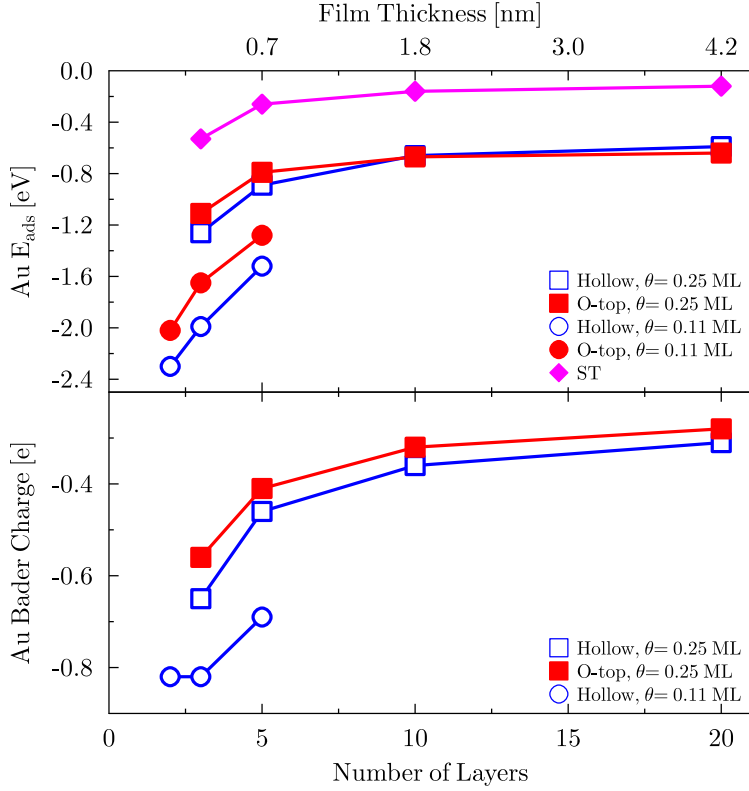


**Figure 6.2:** The adsorption energy and Bader charge of Au atom on MgO/Mo as a function of the oxide film thickness. The filled and hollow symbols denote adsorption on O-top and hollow sites, respectively. The circles and squares denote the adsorbate coverages of 0.11 ML and 0.25 ML, respectively. The magenta diamonds correspond to the classical image charge and polarization interaction energy between a point charge and oxide/metal system according to the ST model parametrized with the DFT optimized distances and Bader charging. The 0.25 ML results are from [IV] whereas the 0.11 ML results are from [44].

model, is plotted into fig. 6.3 as a function of oxide thickness. The DFT results show that the stabilization effect is very similar for both, MgO/Mo and  $\text{Al}_2\text{O}_3/\text{Mo}$ , even if the oxides and their structures are different. This further supports that the long ranged character of the stabilization due to the metal could be qualitatively explained by the classical image charge and polarization interactions. However, the ST model parametrized with the DFT distances and Bader charges seems to predict weaker stabilization than DFT, though.

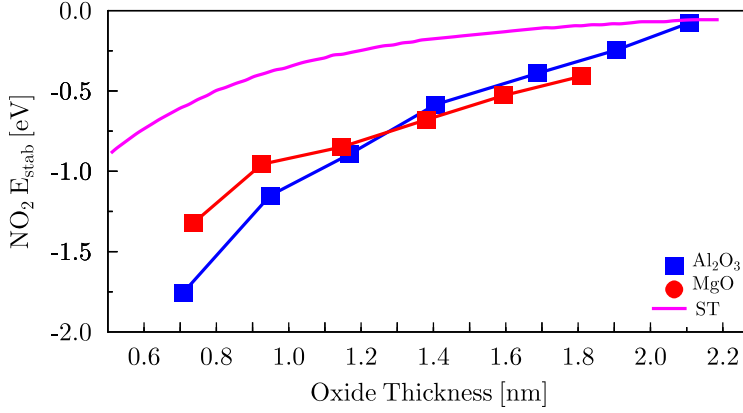


**Figure 6.3:** The energetic stabilization of the  $\text{NO}_2$  adsorbate due to the Mo metal under the MgO (blue squares) and  $\text{Al}_2\text{O}_3$  (red squares) oxide films. The magenta graph shows the stabilization predicted by the ST model when parametrized with DFT distances and Bader charges interpolated with an exponential fit. Adapted from [IV].

### The effect of the adsorbate coverage

The factor ii) Coulombic lateral repulsion between the adsorbates, has been tested by calculating the adsorption energy and charge of Au atom on hollow site of  $\text{MgO}(3\text{L})/\text{Mo}$  at coverages ranging from 0.04 to 0.25 ML. This corresponds to decrease of the nearest neighbor Au-Au distance from 15.9 Å to 6.38 Å. The adsorption energy is plotted as a function of coverage in fig. 6.4, which clearly shows that adsorption becomes stronger as the coverage decreases. At 0.04 ML coverage, Au adsorption energy is -1.97 eV whereas at 0.25 ML it is only -1.26 eV. The weaker adsorption at higher coverages is a sign of increased Coulombic repulsion. However, the increasing repulsion is compensated by the spontaneous decrease of the adsorbate charging, as shown in the lower panel of fig. 6.4. At 0.04 ML coverage, the Au charge is -0.83 |e| whereas at 0.25 ML it is -0.65 |e|.

### The effect of the different metals via work function

The effect of the factor iii), work function of the substrate, has been investigated by calculating the adsorption properties of Au atom and  $\text{NO}_2$  on  $\text{MgO}(2\text{L})$  film supported by Mo, Ag, Pd, Au, and Pt metals [IV]. For these systems, the adsorbate coverage has been 0.25 ML. Furthermore, the adsorption energies of an  $\text{O}_2$  molecule and a  $\text{Au}_3$  cluster have been calculated on  $\text{MgO}(3\text{L})/\text{Mo}$  and  $\text{MgO}(3\text{L})/\text{Ag}$  [VI]. For these, the

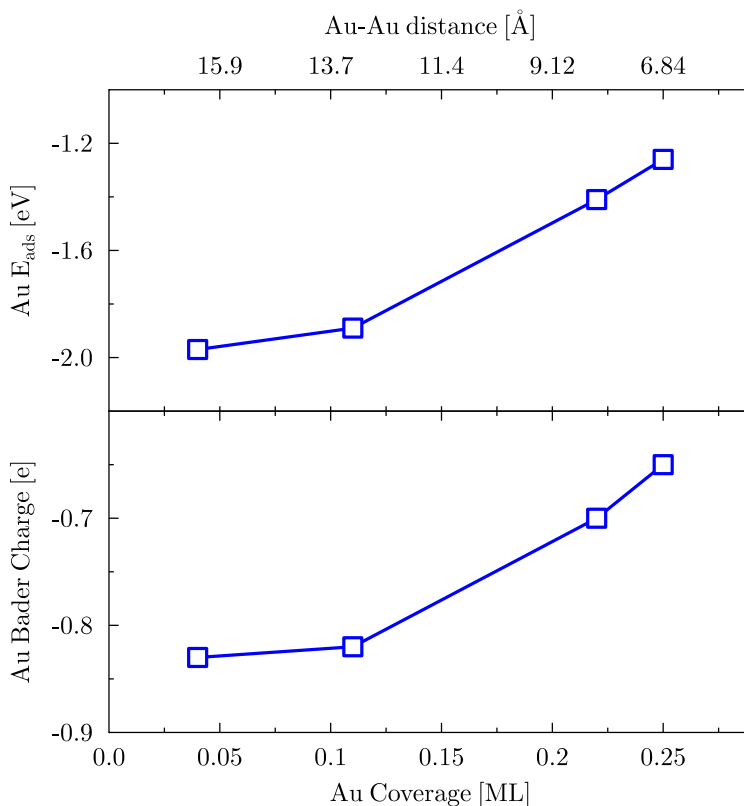


**Figure 6.4:** The adsorption energy and Bader charge of a Au atom on MgO(3L)/Mo as a function of the adsorbate coverage and the shortest adsorbate-adsorbate distance. Adapted from [IV].

coverage has been ca. 0.04 ML. In such systems, the work function of the substrate is determined by the selected carrier metal and its cut plane facing the oxide. Here, MgO is on the (100) face of every considered carrier. The work functions of the bare metals range from 4.1 eV (Mo) to 5.6 eV (Pt). The Madelung field of the MgO polarizes the electrons of the metal-oxide-interface and thus the work functions of thin-film systems are  $\sim 2$  eV lower [IV]. By keeping the oxide and the adsorbate unchanged and by changing the carrier metal, the adsorption energy of Au<sub>1</sub>, Au<sub>3</sub>, O<sub>2</sub> and NO<sub>2</sub> can be evaluated as a function of work function. This is plotted to fig. 6.5. The plot is somewhat scattered but still shows the tendency that lower substrate work function leads to stronger adsorption for all the studied adsorbates.

Further analysis shows that the charges of the adsorbed species are essentially inde-

pendent of the substrate work function. The charges of  $\text{NO}_2$  and Au are  $-0.9 |e|$  and  $-0.8 |e|$ , respectively. The only clear exception is that Au on  $\text{MgO}(2\text{L})/\text{Au}$  is charged only by  $-0.6 |e|$ . These results support the idea that the work function determines the energetic price for electron detachment from the substrate and consequently tunes the energetics of adsorption with charge transfer. Note, however, that the lowering of work function is not necessarily needed for the charge transfer. For example, the work function of  $\text{Al}_2\text{O}_3/\text{Ag}(111)$  is higher than that of bare  $\text{Ag}(111)$ . Still,  $\text{NO}_2$  is charged on  $\text{Al}_2\text{O}_3/\text{Ag}(111)$ . Thus, one can conclude that the absolute final value of the substrate work function is more important for the charge transfer than the magnitude of its change upon thin-film formation. The mechanisms determining the work functions of thin films, and tuning of them with alkali atoms, have been discussed in more detail in the recent works [55, 65].

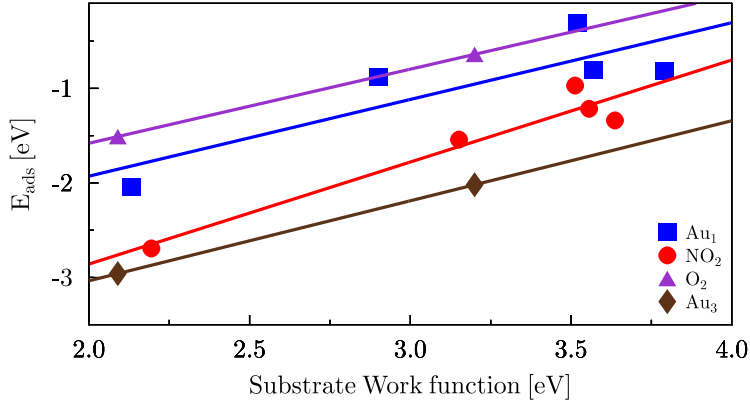


**Figure 6.5:** The adsorption energy of  $\text{O}_2$  [VI] and  $\text{NO}_2$  [IV] molecules, Au atom [IV] and  $\text{Au}_3$  cluster [VI] as a function of the thin-film substrate work function. The linear fits for each adsorbate are mainly to guide the eye. The  $\text{NO}_2$  adsorption energies and the corresponding substrate work functions are calculated with Dacapo code using PBE functional. The Au atom results are obtained with Dacapo and RPBE. The adsorption energies for  $\text{O}_2$  and  $\text{Au}_3$  are calculated with GPAW and RPBE whereas the corresponding substrate work functions are calculated with Dacapo and RPBE.

### The effect of the adsorbate via electron affinity

It is well known that gold clusters have very high electron affinities which depend on the cluster size. The extensive studies on  $\text{MgO}(3\text{L})/\text{Mo}$  supported gold clusters have shown that they become singly or doubly charged depending on their structures [I, II, VI]. The adsorption energies of singly charged clusters correlate with the electron affinities of the gas-phase clusters of the same sizes [II]. Furthermore, if the substrate

donates two electrons to the cluster, the adsorption energy correlates to the sum of the first and second electron affinities of the cluster [VI]. These findings are discussed in more detail in section 6.2.

### Direct bonding between the adsorbate and the oxide

The factor v), direct bonding between the adsorbate and the oxide, is maybe the least studied contributor to the adsorption energetics on thin films. It is well known that the interaction between a gold atom and a regular single crystal MgO terrace is mainly of weak polarization type. The Madelung field of the MgO polarizes the electron cloud of Au atom. On MgO thin film, Au is charged and thus favors positions near to surface cations with positive net charge, *i.e.*, hollow sites or Mg-top sites. The adsorption and charging is accompanied by surface rumbling, which further decreases the distance between the anionic Au and cationic Mg. Thus, most likely, the amount of covalent character of the direct binding is low like on a single crystal and the bonding has mainly ionic character, which reduces the discussion back to factor i) image charge and polarization interaction between the charged adsorbate and the substrate.

### Adsorption induced changes in the oxide-metal-interface

The adsorption induces a polarization pattern to the oxide, as shown with the help of a density difference plot for Au adsorption on MgO(3L)/Ag in fig. 6.6. From this plot, one can see that there is a clear adsorption induced dipole on the metal-surface-interface (IF1). This dipole is accompanied with structural changes. The distance between the oxide and the underlying metal is decreased upon adsorption. For NO<sub>2</sub>, the change is 0.2-0.3 Å whereas for Au atom it is around 0.1 Å. This is a signature of adsorption enhanced adhesion between the metal support and the thin film as earlier discussed in refs. [43, 56]. If one calculates the adsorption energy of a Au atom on MgO(3L)/Ag without allowing the substrate to relax upon adsorption, the adsorption energy is only -0.43 eV whereas it is -1.11 eV for the fully relaxed support with the same adsorbate coverage, 0.25 ML. However, this energy difference can not solely be addressed to the structural changes. The charge of Au on frozen MgO(3L)/Ag is -0.31 |e| whereas on the fully relaxed substrate it is -0.81 |e|. Thus, the energetic contribution of structural changes is difficult to distinguish from charge transfer and polarization effects.



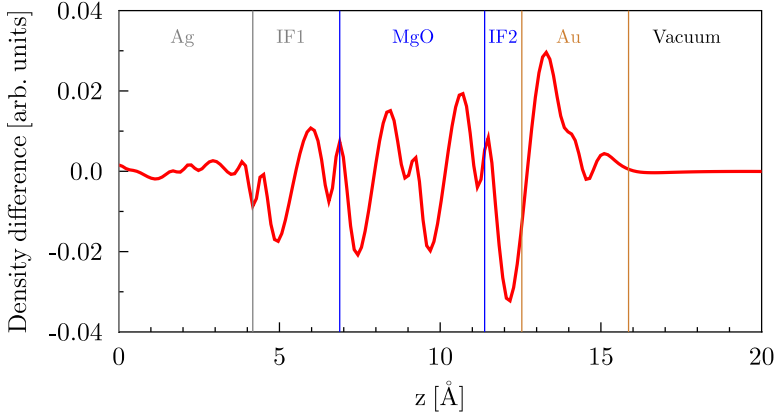


**Figure 6.6:** The xy-plane integrated density difference induced by Au adsorption on MgO(3L)/Ag (red graph) as a function of the  $z$  coordinate. Positive value corresponds to accumulation of charge whereas negative corresponds to depletion. The vertical grey bars denote the  $z$ -coordinates of the top and bottom atom layers of Ag. Similarly, the blue bars show the boundaries for MgO. The orange bars are drawn to both sides of the  $z$  coordinate of the Au nucleus at the Wan der Waals radius 1.66 Å [122]. The Ag-MgO interface region (IF1) as well as the MgO-Au interface (IF2) are marked to the figure.

### The PDOS and KS states of charged adsorbates

In addition to Bader charge analysis, the charging of the thin-film supported adsorbates is shown also by their KS states. For a Au atom, the spin-polarized PDOS projected onto 6s state shows that on single crystal MgO, the state is occupied only by the majority spin. On MgO(3L)/Mo, the state is occupied by both the spins. In a non-spin-polarized calculation this is seen as the half filled two-electron 6s state of single crystal adsorbed Au becomes fully occupied on MgO/Mo. Similar effect is seen also for  $O_2$  and  $NO_2$ .

Fig. 6.7 shows the Kohn-Sham state density projected onto atomic p orbitals of the  $O_2$  adsorbate. The shapes of the corresponding Kohn-Sham orbitals show the bonding  $\sigma_p$ ,  $2\pi_{\perp}$  and  $2\pi_{\parallel}$  as well as the antibonding  $2\pi_{\perp}^*$  and  $2\pi_{\parallel}^*$ . The subscripts  $\parallel$  and  $\perp$  denote the mutual orthogonality of the orbitals. The PDOS analysis shows that the antibonding  $2\pi_{\perp}^*$  is occupied by two electrons with different spins whereas  $2\pi_{\parallel}^*$  is singly occupied. The occupation of the antibonding orbital leads to the elongation of the O-O bond up to 1.37 Å. For comparison, the bond length of a neutral species is 1.24 Å. Thus, in agreement with the Bader charge of -0.97  $|e|$  and magnetic moment of 0.92  $\mu_B$ , PDOS analysis suggests that, on MgO(3L)/Mo,  $O_2$  is singly charged and has clear superoxo character.

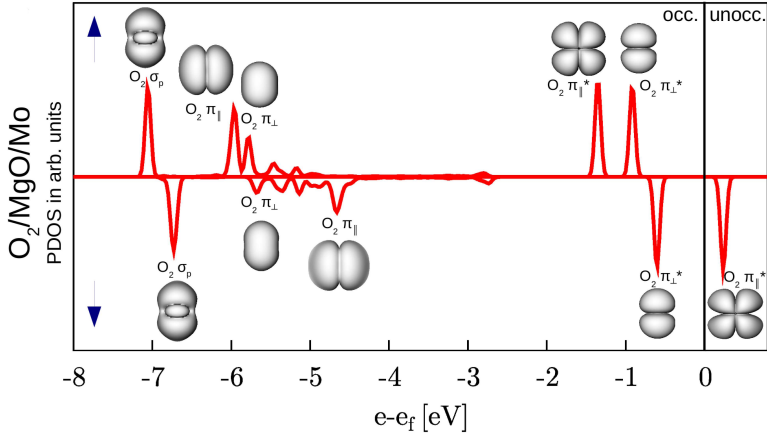


**Figure 6.7:** The PDOS projected onto atomic p orbitals of  $O_2$  molecule on  $MgO(2L)/Ag$ . The shapes of the KS orbitals and their types are given next to the corresponding PDOS peaks. Adapted from [V].

## 6.2 Thin-film effects on metallic clusters

The thin-film effects do not only affect atoms and small molecules but also metallic clusters of various sizes. Their structures, adsorption energies and charge states can be different on a thin film than on a single crystal oxide surface. The electronic states of the clusters can be described with simple potential well models. The possible extra charge transferred from the substrate must be taken into account in the occupations of the model states.

### 6.2.1 Thin-film effects on the Au clusters of 2-6 atoms

Small Au clusters consisting of two to six atoms adsorbed on  $MgO(3L)/Mo$  have been studied in papers [I,II,VI] with Dacapo and GPAW codes applying RPBE functional self consistently. The focus has been on both planar and chain geometries. For  $Au_{1-3}$ , only chain isomers (see panels (a-c) of fig. 6.8) are stable and their adsorption energies vary from -1.26 to -2.77 eV. The adsorption energies of planar  $Au_{4-6}$  clusters (see fig. 6.9) range from -1.14 eV to -2.12 eV, whereas the chain clusters (see panels (d-f) in fig. 6.8) of the same size bind 1.2 - 1.5 eV stronger. Thus, on  $MgO(3L)/Mo$ , the energetically most favorable  $Au_{1-6}$  clusters are chains (see fig. 6.8). Note that the structures tend to maximize their surface contact. Similar optimal geometries have been reported also for Au clusters on  $MgO(2L)/Ag$  [60] and  $Al_2O_3/NiAl$  [59]. On single

crystal MgO, the structures of  $\text{Au}_{1-6}$  clusters are entirely different: The clusters with 3 atoms or more favor planar structures and have only few atoms in contact with the surface (see fig. 6.10). Furthermore, the adsorption is relatively weak with adsorption energies from -0.66 to -1.45 eV [I, II].

The charge analysis shows that the structures and adsorption energies of the clusters depend on their charge states. The linear  $\text{Au}_{1-3}$  and planar  $\text{Au}_{4-6}$  are approximately singly charged whereas the  $\text{Au}_{4-6}$  chains are doubly charged. The singly charged isomers are structurally similar to the anionic gas-phase clusters of the same size and charge [I, II]. However, the doubly charged species are chain-like as they can better accommodate the 2nd electron [VI]. On single crystal MgO, the clusters stay essentially neutral [I, II], and due to the weak interaction with the surface, their structures resemble neutral gas-phase clusters. The adsorption energies of  $\text{Au}_{1-6}$  have been collected to table 6.2 and classified according to substrate and charge state. The table shows clearly that on MgO/Mo, the most charged isomers are the stablest ones. Note, however, that the smallest species,  $\text{Au}_{1-3}$ , do not accommodate more than one electron on MgO/Mo. Similar charging behavior is reported also for  $\text{Au}_{1-6}$  chains on MgO(3L)/Ag [60] and  $\text{Al}_2\text{O}_3(2\text{L})/\text{NiAl}$  [59]. Their charges are plotted in fig. 6.11 together with the values for MgO(3L)/Mo supported clusters [VI]. The plot shows that the charging trends are very similar for MgO(3L)/Mo and MgO(2L)/Ag. However, on MgO(2L)/Ag, the neutral dimer is the most favorable one whereas on MgO(3L)/Mo it is essentially isoenergetic with the singly charged one. On  $\text{Al}_2\text{O}_3(2\text{L})/\text{NiAl}$ , the charging seems to be somewhat stronger:  $\text{Au}_3$  is already doubly charged and  $\text{Au}_{5-6}$  are even triply charged.

**Table 6.2:** The adsorption energies ( $E_{\text{ads}}$ ) of  $\text{Au}_{1-6}$  on single crystal MgO and MgO/Mo for different isomers having variety of spontaneous charges. Note that only neutral species exist on single crystal MgO whereas anions and dianions exist on MgO/Mo. The values in parentheses have been obtained with GPAW [VI] whereas all the others are calculated with Dacapo. The Dacapo results for neutral and singly charged species are from [I,II].

$n$	$\text{Au}_n/\text{MgO}$	$\text{Au}_n^{-1}/\text{MgO}/\text{Mo}$	$\text{Au}_n^{-2}/\text{MgO}/\text{Mo}$
1	-0.66	-1.99 (-2.09)	-
2	-1.12	-1.26 (-1.67)	-
3	-1.15	-2.77 (-2.96)	-
4	-1.45	-1.75	-3.20 (-3.24)
5	-0.92	-2.12	-3.30 (-3.44)
6	-0.71	-1.14	-2.56 (-2.79)

In the case of the singly charged  $\text{Au}_{1-3}$  isomers on MgO(3L)/Mo, the energetic stabilization due to the metal support correlates with the electron affinity of the cluster [II, VI]. The electron affinity oscillates as a function of the cluster size and so does the adsorption energy. However, as the  $\text{Au}_{4-6}$  are doubly charged, their adsorption energies correlate with the sum of the 1st and 2nd electron affinities of the cluster [VI].

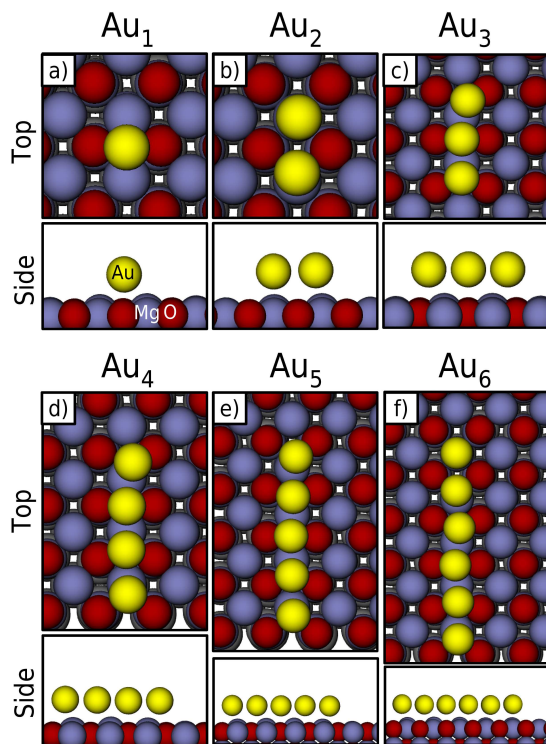


**Figure 6.8:** The top and side views to the optimal geometries of the  $\text{Au}_{1-6}$  clusters on  $\text{MgO}(3\text{L})/\text{Mo}$ . The color code of the atoms is given in the side view of panel (a).

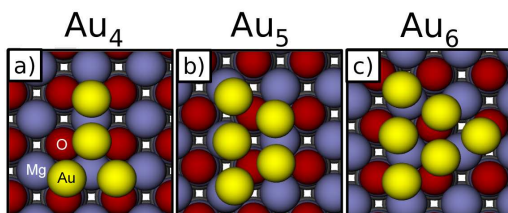


**Figure 6.9:** The top views of the approximately singly charged planar  $\text{Au}_{4-6}$  clusters on  $\text{MgO}(3\text{L})/\text{Mo}$ . The color code of the atoms is given in the panel (a). The geometries are from [II].

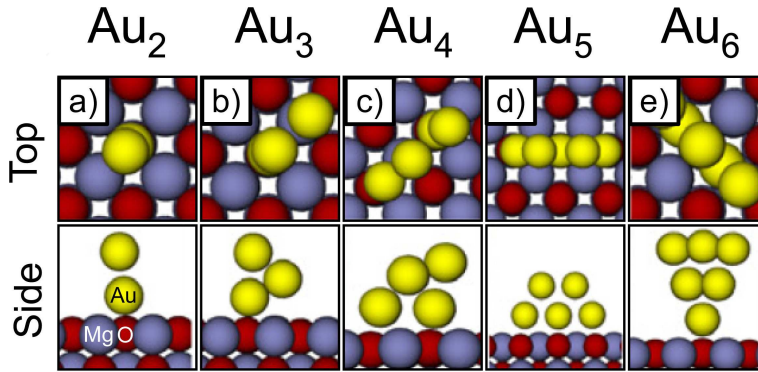


**Figure 6.10:** The top and side views to the optimal geometries of the  $\text{Au}_{2-6}$  clusters on single crystal MgO. The color code of the atoms is given in the side view of panel (a). Adapted from [II].

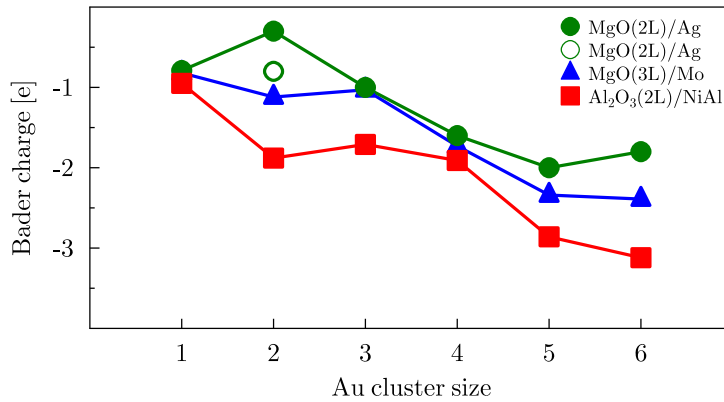


**Figure 6.11:** The Bader charges of  $\text{Au}_{1-6}$  on  $\text{MgO}(3\text{L})/\text{Mo}$  (blue triangles),  $\text{MgO}(2\text{L})/\text{Ag}$  (green circles) and  $\text{Al}_2\text{O}_3(2\text{L})/\text{NiAl}$  (red squares). The hollow green circle denotes the charged dimer isomer on  $\text{MgO}(2\text{L})/\text{Ag}$ , whereas the neutral isomer is lower in energy. Taken from paper [VI].

This is natural, as the energetics are now governed by the attachment of 2 electrons to the adsorbate. To emphasize the correlation trends, the 1st electron affinity and the sum of the 1st and 2nd electron affinities are plotted in the fig. 6.12 with the adsorption energies.

The electronic states of Au chains can be modeled with the help of a one dimensional quantum well model. In such a model, the cluster can be described by a potential well

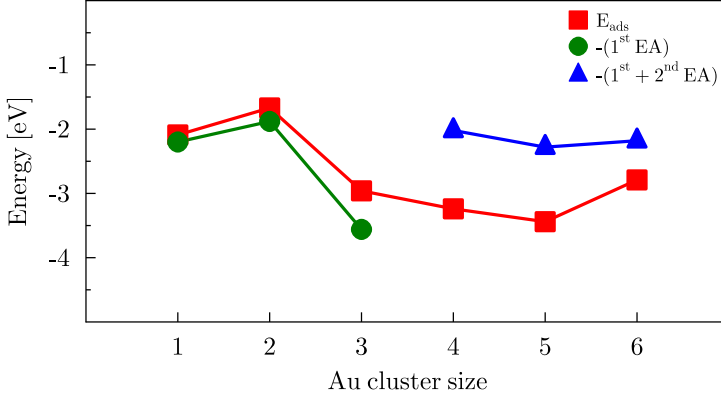


**Figure 6.12:** The adsorption energies of the energetically most favored  $\text{Au}_{1-6}$  on  $\text{MgO}(3\text{L})/\text{Mo}$  (red squares) as well as the 1st (green circles) and the sum of 1st and 2nd (blue triangles) electron affinities of  $\text{Au}_{1-3}$  and  $\text{Au}_{4-6}$ , respectively. Taken from paper [VI].

to which the  $6s^1$  valence electrons of each individual Au atom have been delocalized and confined. For example, a one dimensional harmonic oscillator (1D HO) model gives a good description of the Au chains [VI], although the exact shape of the potential is not important. If the cluster is on a thin film such as  $\text{MgO}(3\text{L})/\text{Mo}$ , also the charge transferred from the substrate is confined into the same potential. Thus, the cluster charging is also shown by the occupation of the quantum well states. In ref. [59], it has been shown via DFT calculations and STM images that the highest occupied molecular orbital (HOMO) states of the chain Au clusters on  $\text{Al}_2\text{O}_3(2\text{L})/\text{NiAl}$  can be described with a similar model.

Fig. 6.13 shows the HOMO and the lowest unoccupied molecular orbital (LUMO) states of  $\text{Au}_3$  and  $\text{Au}_6$  clusters on  $\text{MgO}(3\text{L})/\text{Mo}$ . It also includes a schematic diagram of 1D HO potential and the probability density of the corresponding 1D eigenstates. The LUMO state of  $\text{Au}_3$  has three lobes and two nodes whereas the HOMO has two lobes and one node. These correspond to the HOMO and LUMO of a 1D HO with 4 electrons. Three of those are the atomic  $6s$  derived states (marked with blue arrows in fig. 6.13) whereas one electron must originate from the substrate (marked with red arrow in fig. 6.13). This agrees with the Bader charge  $-1.03$  e of the adsorbed cluster. The LUMO state of  $\text{Au}_6$  has 5 lobes and 4 nodes. The HOMO of the cluster has 4 lobes and 3 nodes. This corresponds to 1D HO with 8 electrons. Now, there are 6 atomic  $6s$  derived electrons in the system and two of them must originate from the substrate. Again, this is in agreement with the Bader charge  $-2.39$  e of the  $\text{Au}_6$ .

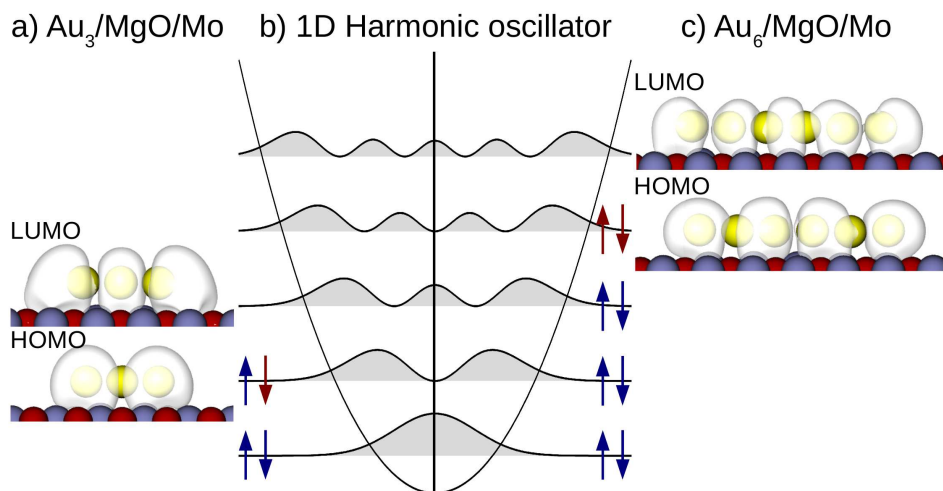


**Figure 6.13:** The spatial appearance of the HOMO and LUMO states of  $\text{Au}_3$  and  $\text{Au}_6$  on  $\text{MgO(3L)/Mo}$  and their connection to a 1 dimensional quantum well model. The blue arrows denote valence electrons from the atomic Au  $6s^1$  states and the red arrows denote charge donated by the substrate. Taken from [VI].

### 6.2.2 Thin-film effects on the Au clusters of 6-20 atoms

The slightly larger Au clusters of 6-20 atoms have been studied on  $\text{MgO(2L)/Ag}$  [V]. In these calculations, GPAW and PBE functional have been applied. The main motivation for studying this cluster size regime is the recent STM experiments. In the experiments, atomic gold has been deposited on the surface, which leads to diffusion and cluster formation. However, in these experiments, it is not possible to probe the clusters in atomic resolution and thus the exact atomic structure of the species and the number of atoms in them remains unknown.

Fig. 6.14 A) shows measured constant-current-mode topographic STM images of a selected Au cluster. With low bias voltages, an image with no details appears as the tunneling is not resonant with any state of the cluster. However, as the bias is adjusted to appropriate values, flower-like shapes appear, which are the HOMO and LUMO states of the cluster. In paper [III], it has been predicted that these flower like states are typical for symmetric and planar Au clusters and the number of atoms in such species could be identified by shape recognition of these states.

Where the states of the linear Au chains resemble the states of a 1D quantum well, the states of symmetric planar clusters are similar to two dimensional (2D) quantum well states [III, V]. In other words, a 2D planar cluster can be modeled with a two

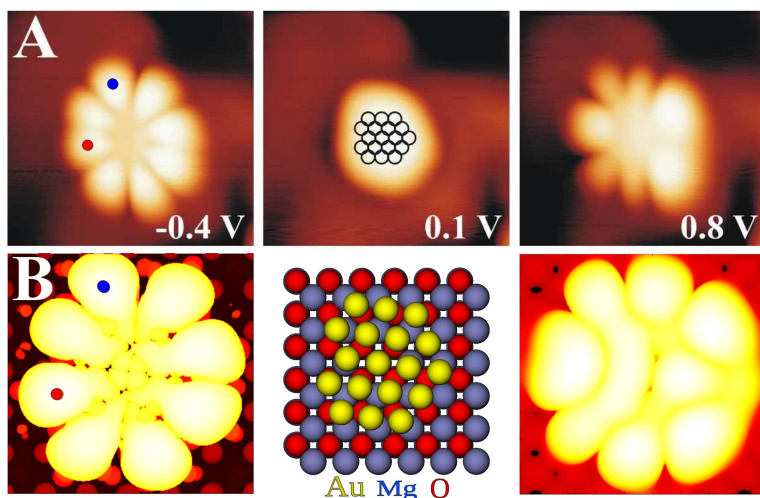


**Figure 6.14:** A) Measured STM images of a selected cluster with bias voltages -0.4 V (HOMO), -0.1 V and +0.8 V (LUMO). B) The simulated STM images of HOMO (leftmost) and LUMO (rightmost) states of  $\text{Au}_{18}/\text{MgO}(2\text{L})/\text{Ag}$ , the structure of which is shown in the middle. Clearly, the measured and computational images match to each other and the cluster in the experiments can be identified as  $\text{Au}_{18}$ . The blue and red dots denote the points from which the  $dI/dV$ -spectra of fig. 6.19 have been taken. Adapted from [V].

dimensional harmonic oscillator (2D HO) potential which confines the atomic 6s valence electrons. If non-interacting fermions are confined into a 2D harmonic potential well, they exhibit states where the number of angular and radial nodes depend on the principal ( $n$ ) and magnetic ( $m$ ) quantum numbers, respectively. The states have  $n-1$  radial nodes and  $|m|$  angular nodes. The schematic energy diagram of such a system is shown in fig. 6.15. Here, the atomic nomenclature of the states have been adopted as defined in the same figure. Thus, for example, 2P state has one radial node as  $n=2$  and two angular nodes as P equals  $|m| = 2$ . The states with higher  $m$ , such as 1F or 1G, are thus very flower like in their appearance. The planar and symmetric clusters exhibit similar states. As every atom brings one 6s electron to the confinement, the atoms can be counted by analyzing the nodal structure of its frontier orbitals in the light of the 2D HO model.

To identify the unknown clusters of the experiment, an extensive DFT search of cluster structures for  $\text{Au}_6$ - $\text{Au}_{20}$  has been carried out. The aim has been to find the clusters having the HOMO and LUMO states which match best with the measured STM images of unknown species. The candidate clusters have been chosen so that their geometries are nearly symmetric and the 2D HO model predicts that they have the same HOMO and LUMO states as seen for the unknown species in the experiments.



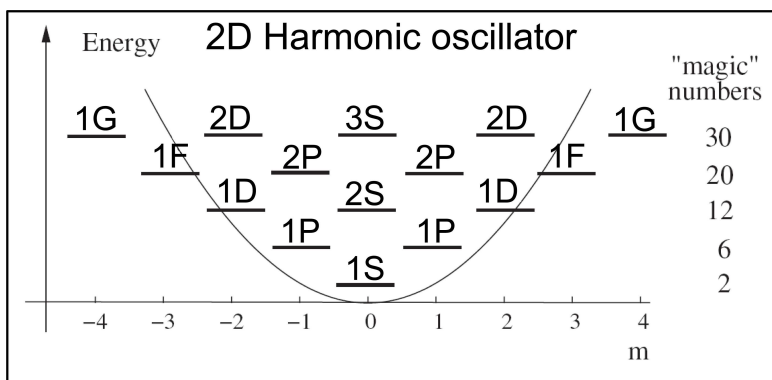


**Figure 6.15:** The energy level diagram of non-interacting fermions confined in a two dimensional harmonic oscillator potential. The states are denoted in analogy to atomic nomenclature  $nm$  such that  $n=1,2,3,\dots$  and  $|m|=0,1,2,3,4$  is denoted with S, P, D, F and G. The shell closing numbers are called magic numbers as these correspond to extremely stable confinements. Adapted from [III].

As the substrate induced charging is possible on thin films, it has been taken into account that there might be more 2D HO states occupied than there are atomic 6s valence electrons. However, as the charge has not been known before the post analysis of DFT results, the procedure has included iterations with trial and error.

In fig. 6.16, a few candidate structures are shown. The calculations predict that also Au clusters of around 10-20 atoms experience thin-film effects, *i.e.*, on MgO(2L)/Ag, their geometries are flat and they have low formation energies from -2.1 eV/atom to -2.5 eV/atom. According to charge analysis, the smallest species of this size range are doubly charged whereas the largest clusters can accommodate even 3 to 4 electrons originating from the substrate. This relatively high charge state is in agreement with the average charging of -0.20  $|e|$ /atom calculated for a Au monolayer on a 2ML MgO/Ag.

Fig. 6.17 shows the frontier orbitals of  $\text{Au}_{14}$ ,  $\text{Au}_{18}$  and  $\text{Au}_{19}$  candidate clusters on a MgO(2L)/Ag surface. The atomic structures are given in panels (c-e) in fig. 6.16. As predicted already in paper [III], the spatial appearance of the frontier orbitals resemble the states of a 2D HO. Thus, these quantum well states have been labeled according to the 2D HO states. The labeling is shown in the left most column of fig. 6.17. The subscripts  $\perp$  and  $\parallel$  refer to the different orientations of the states with the same angular momentum character.

The HOMO of  $\text{Au}_{14}$  has six lobes and no radial nodes and is thus of  $1F_{\perp}$  type. As far as the LUMO is concerned, it has two angular lobes and one radial node. Hence, it is of  $2P_{\parallel}$  type. According to the filling of the 2D HO occupation diagram (see panel

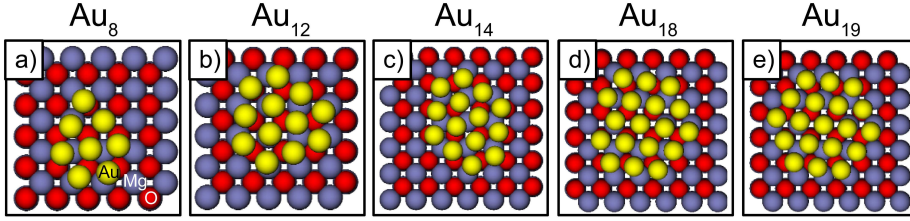


**Figure 6.16:** Selected candidate structures for  $\text{Au}_{8-20}$  clusters used in the search process when identifying atomic structures from measured STM images.

(B) in fig. 6.18), this corresponds to a quantum well with 16 electrons, 14 of which are the atomic 6s derived electrons, whereas 2 originate from the substrate. This is supported by the Bader charge of -2.27 e. The LUMO+1 has also 2P character but is rotated  $90^\circ$  relative to LUMO and it is thus labeled as  $2P_\perp$  type. The LUMO+2 has 8 lobes and no radial nodes, which makes it 1G type.

The HOMO and LUMO of  $\text{Au}_{18}$  have both 1G character similar to the  $\text{Au}_{14}$  LUMO+2, which suggests that it can be described with a quantum well having at least 5 electrons more than the  $\text{Au}_{14}$ . As 18 of the electrons are the atomic 6s derived ones, 3 to 5 must originate from the substrate. In agreement with this, the Bader charge of  $\text{Au}_{18}$  is -3.54 [e]. For example, a 2D HO model filled with 18 electrons from the atomic 6s states and 4 from the substrate is shown in the panel (A) of fig. 6.18. In addition, the same  $\text{Au}_{18}$  geometry has been calculated in gas-phase with 3 and 4 extra electrons. Both these species show similar HOMO and LUMO states, and thus it is not possible to distinguish  $\text{Au}_{18}^{3-}$  and  $\text{Au}_{18}^{4-}$  with the help of these states.

In fig. 6.14, the simulated STM images of the  $\text{Au}_{18}$  HOMO and LUMO states (panel B) are compared to the measured HOMO and LUMO of the unknown cluster (panel A). Clearly, the match between the experimental and computational HOMO and LUMO states is almost perfect. This suggests that the species in the experiments is  $\text{Au}_{18}$ , and furthermore, it is charged by 3 or 4 electrons. However, other than HOMO and LUMO states can not be directly imaged in the topographic constant-current-mode of STM. Instead, conductance imaging is needed to analyze those.

In the panel A of fig. 6.19, the measured and simulated  $dI/dV$ -spectra taken from the blue and red points marked to the STM images of fig. 6.14 [V] are shown. The measured and simulated  $dI/dV$ -maps corresponding to the peaks of the spectra are given in the panels B and C of fig. 6.19, respectively. Both  $dI/dV$ -spectra show similar features and even the relative intensities of the peaks agree very well. Note anyway that the widths of the peaks can not be compared between the spectra as the simu-

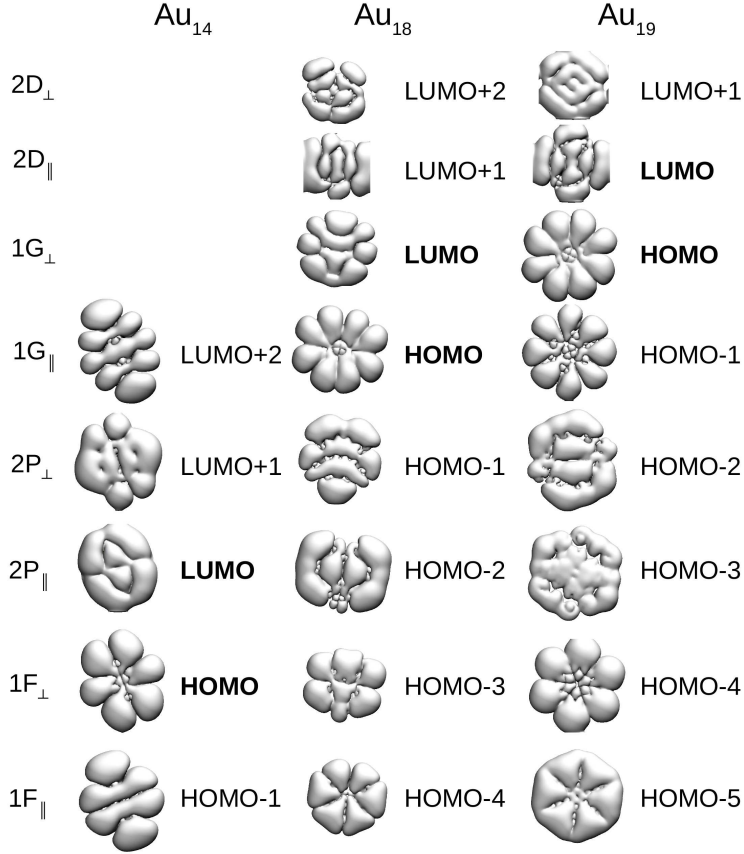


**Figure 6.17:** The shapes of the Kohn-Sham states localized to Au<sub>14</sub>, Au<sub>18</sub> and Au<sub>19</sub> clusters on MgO(2L)/Ag. The states are labeled after their similarity to two dimensional harmonic oscillator states by counting their radial and angular nodes.

lated peaks are artificially broadened. The energy scale of the simulated spectrum is narrower than that of the measured one. However, this is in agreement with the fact that the KS states, on which the simulations are based on, lie typically in a narrower energy window than the real many body states. The similar appearance of the measured and simulated  $dI/dV$ -maps corresponding the spectral peaks further supports that the cluster is Au<sub>18</sub> which acts as a quantum dot of 21 or 22 delocalized valence electrons, and is thus charged by 3 to 4 electrons.

However, there are many open questions such as, how sensitive the spatial appearance of the states is for the exact atomic structure? Or, is the identified cluster really Au<sub>18</sub>

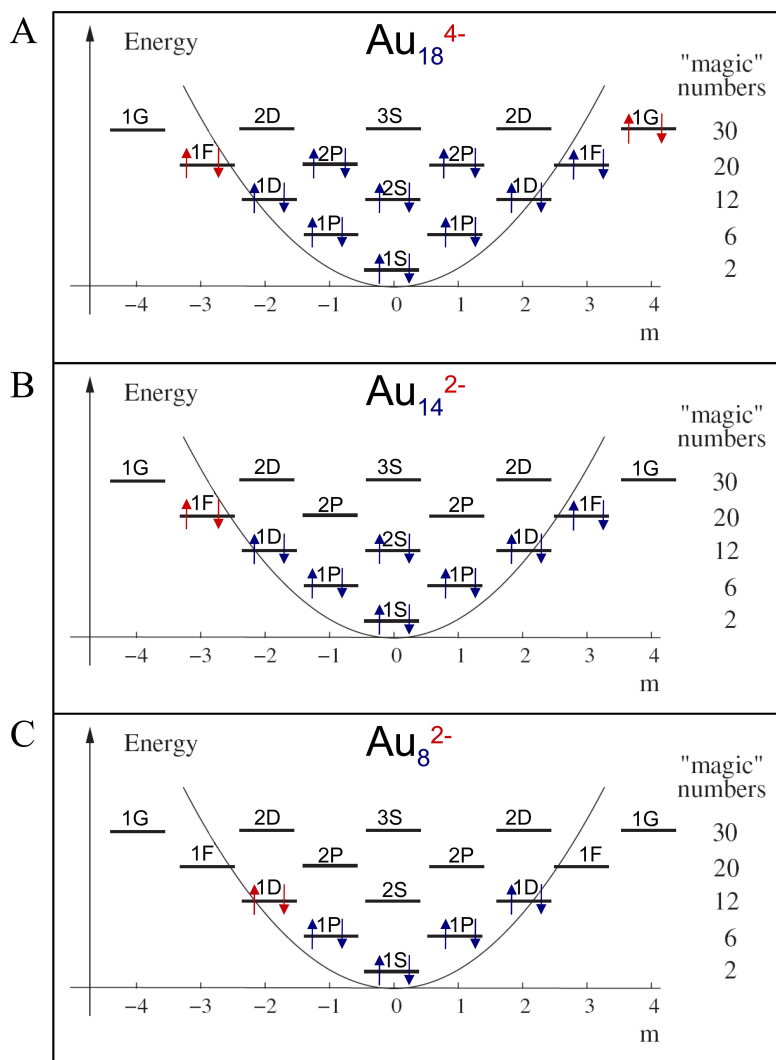


**Figure 6.18:** The two dimensional harmonic oscillator modeling of  $\text{Au}_8$ ,  $\text{Au}_{14}$  and  $\text{Au}_{18}$  clusters adsorbed on  $\text{MgO}(2\text{L})/\text{Ag}$ . The blue arrows denote the delocalized atomic 6s electrons the number of which is the same as the one of gold atoms. The red arrows denote electrons transferred from the substrate. Adapted from [III, V].

with 3 or 4 extra electrons as, for example,  $\text{Au}_{20}^{2-}$  should have similar states according to the 2D HO model? The following examples will answer to these questions.

Fig. 6.20 compares the simulated STM image of the LUMO state of two different

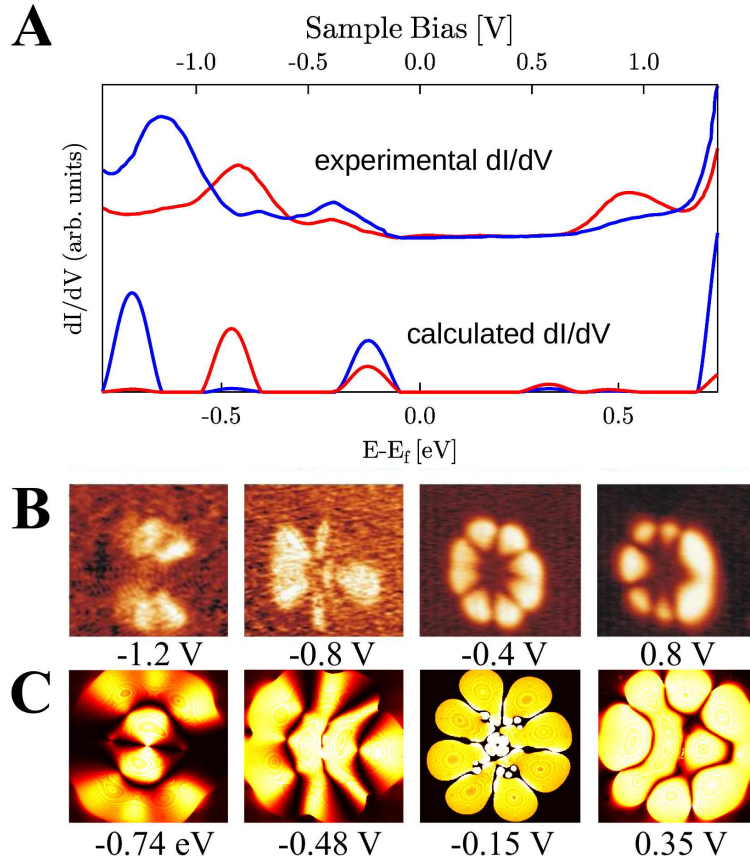


**Figure 6.19:** A) The measured and calculated  $dI/dV$ -spectra for  $\text{Au}_{18}/\text{MgO}(2\text{L})/\text{Ag}$  shown in fig. 6.14. The blue and red spectra are taken from the points marked with the same colors to the simulated and measured STM images in fig. 6.14. B) The measured  $dI/dV$ -maps corresponding to the peaks in the measured  $dI/dV$ -spectrum. C) The simulated  $dI/dV$ -maps corresponding to the peaks of the simulated  $dI/dV$ -spectrum. Note that the match between the experiments and the simulation is almost perfect. Adapted from [V].

atomic structures of  $\text{Au}_{10}$  clusters on  $\text{MgO}(2\text{L})/\text{Ag}$ . The structures are nearly isoenergetic as their formation energies are -2.23 eV/atom and -2.29 eV/atom. Clearly, for both the structures, the LUMO state has 1F character. Note, however, that their exact shapes are different. As the HOMO states (not shown) have 1D character, the appearance of the simulated STM image corresponds to a 2D HO with 12 electrons. As 10 of them are atomic 6s derived states, 2 of them are from the substrate. This is supported by the charges of both the geometries, -2.08 |e| and -1.98 |e|. This shows

the typical feature that the orbital 2D HO character is determined by the number of atoms and amount of charge transferred to the cluster although the exact shapes of the orbitals are sensitive to the atomic positions. This is reasonable, as the atomic positions control the shape of the effective quantum well. States similar to 2D HO occur if the well is symmetric enough. From this, it follows that the structures and charge states of the clusters can be identified from measured STM images with the help of simulated STM images obtained from DFT calculations.

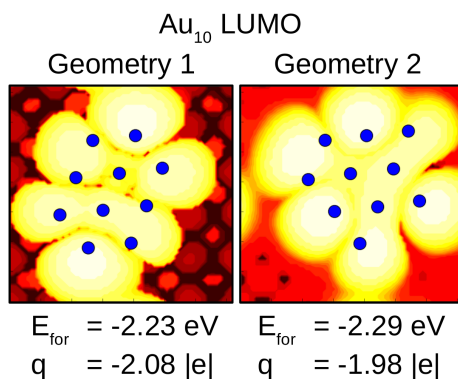


**Figure 6.20:** The LUMO states of two  $\text{Au}_{10}$  clusters with different atomic structures as seen in the simulated STM. The blue dots correspond to the coordinates of the atoms. The formation energies are given per atom and the charges are obtained with the Bader analysis. Note that whereas both the states are of 1F type, as also suggested by their charges, the exact shape of the orbitals depends on the exact atomic positions.

For final check, the  $\text{Au}_{20}^{2-}$  was calculated in gas-phase, as it should have 1G HOMO and LUMO states similar to  $\text{Au}_{18}^{3-}$  or  $\text{Au}_{18}^{4-}$  according to the 2D HO model. Indeed, this is the case, but, again, due to the different number of atoms and due to differences in their positions, the exact shapes of the orbitals are different (see fig. 6.21). Furthermore, calculations suggest that  $\text{Au}_{20}$  is charged by 4 electrons on the surface, and thus, in principle,  $\text{Au}_{20}^{2-}$  should not be even observed in the experiments (see fig. 6.21). This further supports the conclusion that the originally unknown surface species in fig. 6.14 is really  $\text{Au}_{18}$ .

In addition to  $\text{Au}_{18}$ , it was possible to identify also few other species from the measured STM images. Fig. 6.22 gives both the simulated and measured HOMO and LUMO states of  $\text{Au}_8$  and  $\text{Au}_{14}$ . The atomic structures of both the clusters are shown in fig. 6.16 and the shapes of the KS states of the  $\text{Au}_{14}$  are given in fig. 6.17. The appearance of the measured and simulated STM images suggest that they both are charged by 2 electrons, which is supported by their Bader charges  $-1.90 |e|$  and  $-2.27 |e|$ , respectively. The corresponding 2D HO model occupations are shown in fig. 6.18.

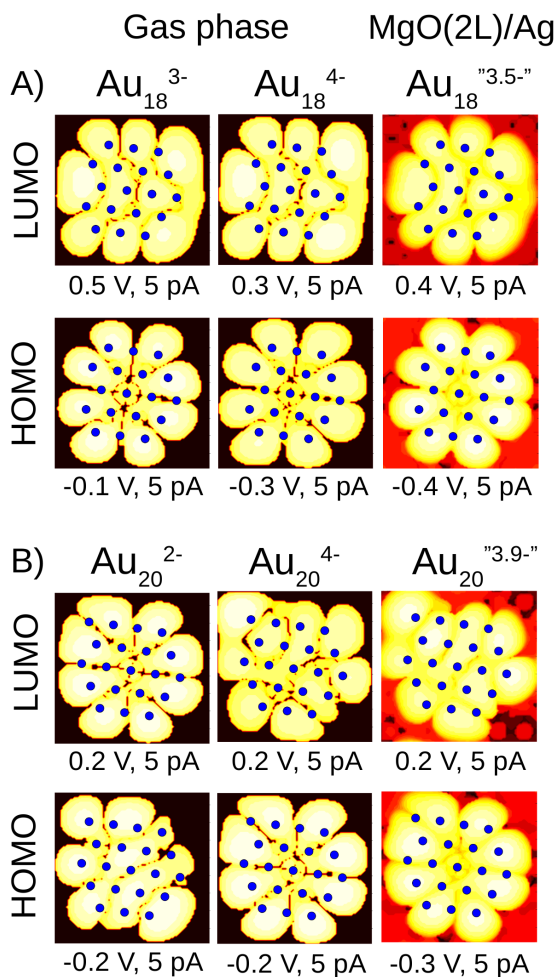


**Figure 6.21:** The HOMO and LUMO states of A)  $\text{Au}_{18}$  and B)  $\text{Au}_{20}$  clusters in gas phase and on MgO(2L)/Ag for different charge states of the species. The blue dots correspond to the coordinates of the atoms. Note that the charging is spontaneous on thin film and the value given in the superscript is obtained with the Bader method.

To sum up, both the experiments and calculations show that the MgO(2L)/Ag supported Au clusters are flat and charged. The charging is not only accumulation of electrons to the cluster-substrate interface but this transferred charge really occupies the electronic states of the cluster. The clusters can be identified with the help of DFT/STM/STS study which combines the state of the art measurements and calcu-

lations. The states of nearly symmetric clusters can be rationalized with the help of the 2D HO model.

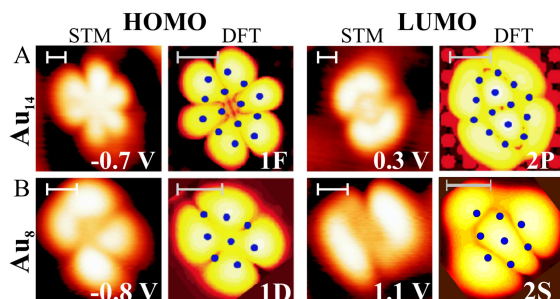


**Figure 6.22:** The simulated and measured STM images of A)  $\text{Au}_{14}$  and B)  $\text{Au}_8$  HOMO and LUMO states. The corresponding bias voltages are marked to the measured images whereas the symmetry labels of the states are in the simulated images. The blue dots correspond to the coordinates of the atoms. The scale bars are 2 Å in all the images.

## 6.3 Towards chemistry of Au clusters

To probe the catalytic properties of  $\text{Au}_{1-6}$  chains on  $\text{MgO}/\text{Mo}$ , the  $\text{O}_2$  adsorption properties have been calculated on each cluster.  $\text{O}_2$  adsorption and activation are necessary to oxidation reactions catalyzed by metal particles.

### 6.3.1 The $\text{O}_2/\text{Au}_{1-6}/\text{MgO}(3\text{L})/\text{Mo}$ structures and their energetics

Fig. 6.23 presents the optimal geometries of  $\text{O}_2/\text{Au}_{1-6}$  complexes on a  $\text{MgO}(3\text{L})/\text{Mo}$  substrate. The  $\text{O}_2$  adsorption energies are plotted in fig. 6.24 and tabulated together with O-O,  $\text{O}_2\text{-Au}$  and  $\text{O}_2\text{-Mg}$  bond lengths in table 6.3. The oxygen molecule favors adsorption at the end of the  $\text{Au}_{2-6}$  chains, bridging simultaneously two Mg cations (see fig. 6.23 (b-f)), whereas the adsorption on top of a cluster is unstable. The bridge position is the optimal adsorption site also on bare  $\text{MgO}/\text{Mo}$ . According to calculations, the energetically most favorable  $\text{O}_2/\text{Au}_{2-6}$  complexes obey the following structure motifs: i) The Au clusters are chains as it is the most optimal geometry to accommodate the extra charge originating from the support [60]. ii) The negatively charged Au atoms are on positive  $\text{Mg}^+$  cations or in the hollow sites which are also favorable sites for a single Au atom on a thin film [41, 44]. iii) The oxygen molecule favors the



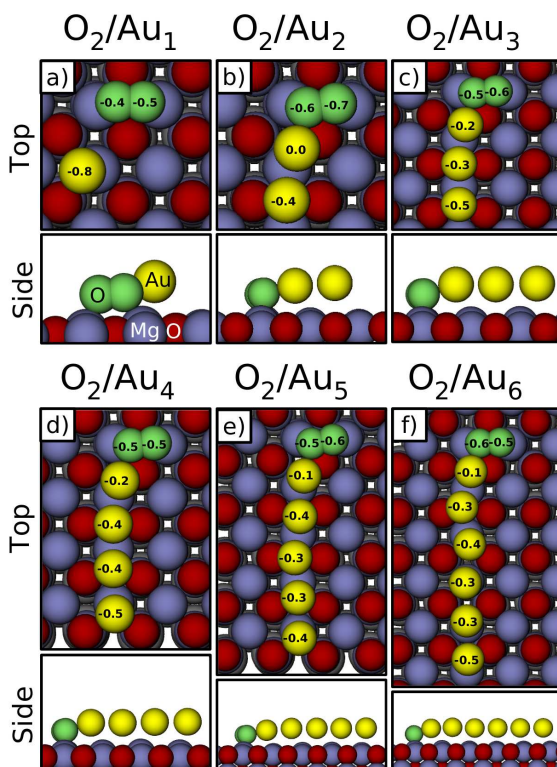


**Figure 6.23:** The top and side views of the optimal geometries for  $O_2/Au_{1-6}$  complexes on  $MgO(3L)/Mo$ . The color code of atoms is given in the side view of panel (a). The Bader charges of the atoms have been marked to the corresponding atoms. Taken from [VI].

bridge site between surface Mgs as it does on a bare  $MgO/Mo$ . iv) There is an angle between an  $O_2$  and a Au chain so that the degeneracy of the  $2\pi^*$  is broken and the spatial overlap is maximized with the cluster HOMO. In gas-phase, the angle is ca.  $130^\circ$  [21, 28, 31], whereas the surface forces it to be closer to  $90^\circ$ .

Fig. 6.24 shows that the  $O_2$  adsorption is strongest on  $Au_2$  and  $Au_3$  with the adsorption energies of -1.48 eV and -1.33 eV, respectively. On  $Au_4$ , the binding is weakest, -0.68 eV and the  $O_2/Au_1$  complex is unstable. Fig. 6.24 also compares the adsorption on thin-film supported and gas-phase clusters. In gas-phase, the  $O_2$  adsorption energy oscillates as a function of cluster size. Similar oscillations have also been reported for  $O_2$  adsorption on Au clusters on an oxygen vacancy of bulk  $MgO$  surface [123]. However, on  $MgO/Mo$ , the oscillation trend is absent.

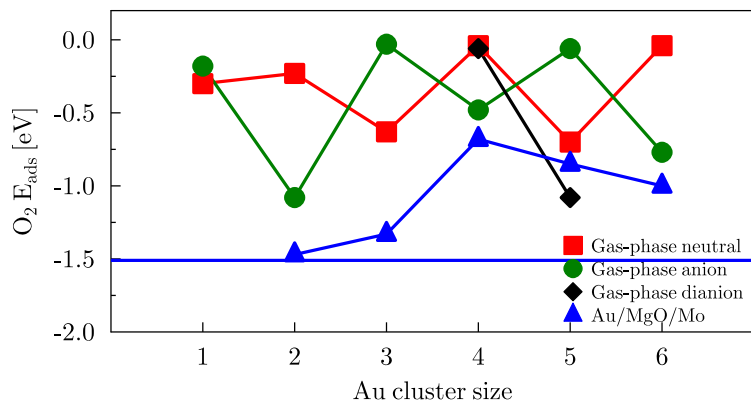


**Figure 6.24:** The adsorption energy of molecular  $O_2$  on chain-like clusters on  $MgO(3L)/Mo$  (present study) as well as on selected neutral [123], anionic [123] and dianionic (present study) gas-phase clusters. The horizontal (blue) line gives the  $O_2$  adsorption energy to bare  $MgO(3L)/Mo$ . Taken from [VI].

Interestingly, on bare  $MgO(3L)/Mo$ , the adsorption energy of  $O_2$  is -1.51 eV, being 0.03 to 0.83 eV stronger than on the studied clusters. The lowest value, 0.03 eV, is well below the computational accuracy and not much can be deduced from that. However, the larger values suggest that there exists a thermodynamic driving force which separates the molecule from the clusters. Note anyway that this is not a universal phenomenon of thin films. For example, on  $MgO(2L)/Ag$ , the  $O_2$  adsorption on  $Au_3$  cluster is 0.1 eV stronger than on the bare terrace. This indicates that the direction of the thermodynamic force depends on the metal below  $MgO$ . In general, the metal seems to determine the adsorption energy range. It is interesting to note that the adsorption energy of  $O_2$  on  $Au_3/MgO(2L)/Ag$  is only -0.75 eV whereas on  $Au_3/MgO(3L)/Mo$ , it is -1.33 eV. This qualitatively agrees with the lower work function of  $MgO(3L)/Mo$  and exemplifies that the choice of the supporting metal determines the  $O_2$  adsorption energy both on a clean surface and on the thin-film supported clusters.

### 6.3.2 The charging of the optimal geometries

In fig. 6.25, the Bader charges of the  $O_2/Au_{2-6}$  complexes have been plotted as a function of the cluster size. Furthermore, the charging is divided into separate, partial, contributions from the  $O_2$  and  $Au_{2-6}$ . Fig. 6.23 gives the Bader charges for individual atoms of the adsorbates and the partial charge of  $O_2$  is also given in table 6.3 for each cluster size. Here, the concept of *partial charge* is used instead of *charge state* as the

**Table 6.3:** The  $O_2$  adsorption energy ( $E_{\text{ads}}$ ) to  $Au_{2-6}$  on  $MgO(3L)/Mo$  and  $O_2$  Bader charge ( $q$ ) in the formed complexes. The last three columns contain the  $O_2$  ( $d_{O-O}$ ),  $O_2$ -cluster ( $d_{O_2-Au}$ ) and  $O_2$ -surface  $Mg$  ( $d_{O_2-Mg}$ ) bond lengths in the  $O_2/Au_{1-6}$  complexes on  $MgO(3L)/Mo$ . The first row gives the properties of  $O_2$  on bare  $MgO(3L)/Mo$ . The energies, bond lengths and charges are in eV, Å and |e|, respectively. Taken from paper [VI].

Size	$E_{\text{ads}}$	$q(O_2)$	$d_{O-O}$	$d_{O_2-Au}$	$d_{O_2-Mg}$
-	-1.51	-0.97	1.37	-	2.12
1	-	-0.88	1.35	3.85	2.12
2	-1.48	-1.25	1.46	2.14	2.04
3	-1.33	-1.08	1.41	2.26	2.09
4	-0.68	-1.00	1.39	2.28	2.10
5	-0.85	-1.12	1.42	2.22	2.08
6	-1.00	-1.12	1.43	2.17	2.07

Au and  $O_2$  have formed a complex with common charge.

The negative charge of the complex increases as the aggregate gets larger whereas the partial charge of  $O_2$  stays nearly constant. The most interesting observation is that the simple picture, in which the charged gold cluster shares its extra electron(s) with the  $O_2$  upon complex formation, is not valid on thin films. For example, the  $MgO(3L)/Mo$  supported  $Au_4$  is spontaneously charged by -1.7 |e|. When  $O_2$  adsorbs on this system, the total charge of the formed complex is ca. -2.5 |e|. This means that the  $O_2$  adsorption induces extra charge transfer from the substrate showing the active role of the thin-film support. For  $O_2$  adsorption on  $Au_{2-6}/MgO(3L)/Mo$ , the average extra charge transfer is 0.72 |e|.

The Bader charge of  $O_2$  seems to be a good measure for the antibonding character of the molecule and the bond length of  $O_2$  correlates linearly to the charge of the molecule as shown in fig. 6.26. Upon adsorption on  $Au_{2-6}$ , the oxygen bond length ( $d_{O-O}$ ) elongates to 1.39 Å - 1.47 Å which is 0.02 Å - 0.09 Å longer than on a clean  $MgO/Mo$  terrace (see table 6.3) and 0.16 Å - 0.23 Å compared to neutral gas-phase  $O_2$ .

### 6.3.3 The projected density of states analysis of the bonding

To get more insight to the  $O_2$  bonding with Au chains on  $MgO/Mo$ , the KS densities of states (DOS) of the systems have been analyzed. Fig. 6.27 shows the density of states for both spins projected to atomic orbitals of the adsorbate atoms (PDOS) in  $O_2/Au_2/MgO(3L)/Mo$  (panel a) and  $O_2/Au_4/MgO(3L)/Mo$  (panel b) systems. The shapes of the Kohn-Sham orbitals are given next to the corresponding PDOS peaks. From fig. 6.27 a), one can see that the HOMO of the  $Au_2O_2$  surface complex has

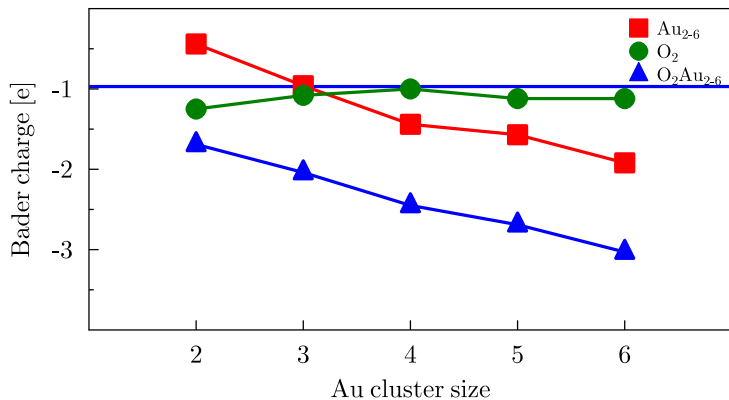


**Figure 6.25:** The Bader charge of O<sub>2</sub>/Au<sub>2-6</sub> on MgO(3L)/Mo. The charge is also divided into contributions from O<sub>2</sub> and Au<sub>2-6</sub>. The horizontal line shows the O<sub>2</sub> charge on bare MgO(3L)/Mo. Taken from [VI].

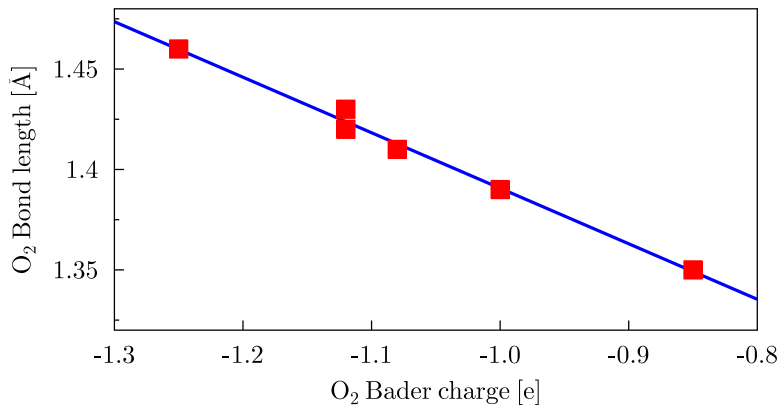


**Figure 6.26:** The O<sub>2</sub> bond length as a function of the O<sub>2</sub> Bader charge for O<sub>2</sub>/Au<sub>1-6</sub>/MgO/Mo systems (red squares) as well as the corresponding linear regression (blue line). Taken from [VI].

significant antibonding Au<sub>2</sub>  $\sigma_s^*$  character. Obviously, this is due to the charge transfer from the support. Clearly, this  $\sigma_s^*$  is hybridized with the antibonding O<sub>2</sub>  $2\pi_{||}^*$  and  $2\pi_{\perp}^*$  orbitals. Both of these are below the Fermi level, which suggests that the molecular oxygen has significant peroxo character in a thin-film supported Au<sub>2</sub>O<sub>2</sub> complex. This is in agreement with the long O-O bond length of 1.47 Å and the zero total magnetic

moment of the the complex given by the Bader analysis.

When  $O_2$  adsorbs on thin-film supported  $Au_4$ , the  $O_2$   $2\pi^*$  states split in energy and hybridize with the quantum well states of the cluster, which can be seen from fig. 6.27 b). The splitting complicates the analysis of the  $O_2$  character to some extent. However, comparison of the  $O_2/MgO(3L)/Mo$  (fig. 6.7) and  $O_2/Au_4/MgO(3L)/Mo$  (panel (b) in fig. 6.27), suggests that the molecule can be considered as a superoxo like species in both cases. In agreement with this, the oxygen bond length is 1.39 Å and the total magnetic moment of the complex is  $0.85 \mu_B$ . One can conclude that where the bare  $MgO/Mo$  substrate already activates the  $O_2$  to its superoxo-like state, the hybridization with the cluster states can further increase the antibonding character of  $O_2$ .

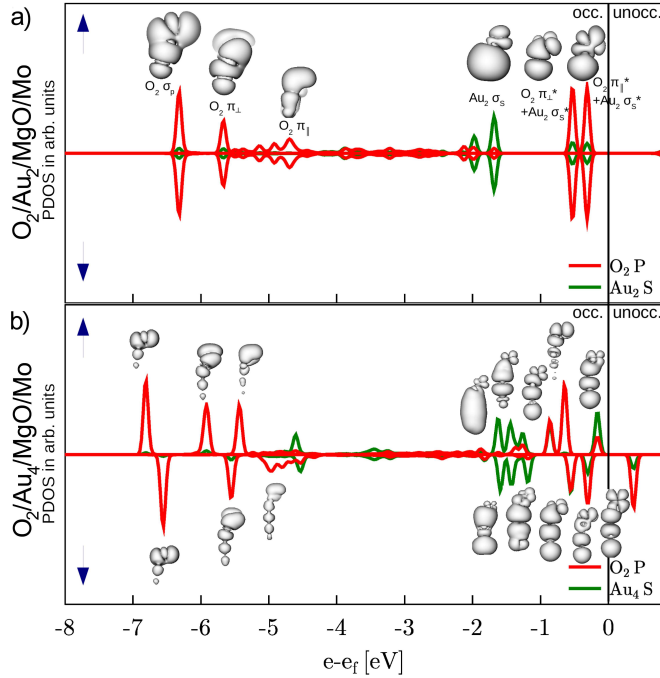


**Figure 6.27:** The spin-polarized PDOS of (a)  $O_2/Au_2$  and (b)  $O_2/Au_4$  on  $MgO(3L)/Mo$ . The projections are onto O p (red) and Au s (green) states. The shapes of the Kohn-Sham orbitals are drawn next to the corresponding PDOS peaks. The Fermi-level is at zero. Adapted from [VI].

### 6.3.4 One possible scenario of cluster catalysis

The activation of  $O_2$  without clusters and the slight metastability of the supported  $O_2/Au_{2-6}$  complexes raise the question whether these small cluster chains have any role in catalyzing oxidation reactions on  $MgO(3L)/Mo$ . However, the following reaction mechanism is proposed. It is already known [57] that CO binds to thin-film supported clusters stronger than to the clean thin-film terrace. Furthermore, a relatively low diffusion barrier,  $\sim 0.5$  eV, has been calculated for the  $O_2$  molecule on  $MgO(3L)/Mo$ . Thus, the reaction might proceed so that the clusters trap CO whereas the bare surface traps and charges the  $O_2$ . As the diffusion barrier of  $O_2$  is low, it can occasionally reach a cluster with adsorbed CO and form  $CO_2$  at the cluster/surface interface, which is able to activate  $O_2$  further. A schematic view of this process is given in fig. 6.28. The process could be tuned by adjusting the adsorption energies of the involved species by selecting the support metal with an appropriate work function and by depositing an oxide film with optimal thickness on it.

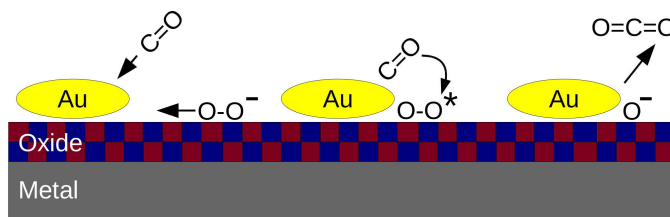


**Figure 6.28:** A schematic presentation of CO oxidation scheme, in which the small Au clusters trap the CO whereas the oxide thin-film adsorbs and activates the  $O_2$ . The activated  $O_2$  can diffuse to the oxide-cluster-interface where it is activated further and where it reacts with CO. Consequently,  $CO_2$  is released to the gas phase. Taken from [VI].

On  $MgO(3L)/Mo$ , the  $O_2$  molecule is activated most by  $Au_2$ , which makes it the best candidate for a model catalyst found in this study. The anionic  $Au_2$  has been earlier found to be an active catalyst in gas phase [21, 28]. However, on a thin film, the activation of  $O_2$  is not only due to the interaction with the spontaneously charged Au cluster because the substrate provides extra charge upon the formation of  $O_2/Au_{2-6}$  complex. Consequently, whereas in gas phase, the  $O_2$  activation is very much dependent on how easily the cluster shares its charge, on a thin film, the charge donated by the substrate reduces the differences between the clusters.

## 7 Summary and outlook

In the work presented in this thesis, it has been shown that the properties of small molecules, such as  $O_2$  and  $NO_2$ , and gold clusters of  $\sim 1$ -20 atoms are different on metal supported oxide thin-films compared to single-crystal oxide adsorbed species. The emphasis has been on MgO/Mo and MgO/Ag thin-film substrates, although some other metal carriers, such as Pd, Pt and Au, and  $Al_2O_3$  oxide, have been considered to gain more general insight to the phenomenon. The differences in the adsorption properties and chemistry between the thin-film and single crystal supported species have been called thin-film effects. The studies for Au atom adsorption on MgO film of 2-20 layers thickness suggest that the thin-film effects are significant for films below  $\sim 1$ -2 nm for their thickness.

It has been found that the adsorption of  $O_2$ ,  $NO_2$  and  $Au_{1-6}$  is strong on thin MgO/Mo film, whereas it is relatively weak on MgO single crystal. The enhanced binding is accompanied with spontaneous charging of the species upon adsorption. On single crystal MgO, these adsorbates stay neutral. The charging leads to changes in the structural and electronic properties of the adsorbates. For example, on MgO/Mo,  $O_2$  molecule is elongated and activated to its superoxo-like state, whereas it interacts very weakly with single crystal MgO. As far as the  $Au_{1-6}$  clusters are considered, they favor 1D chain like structures lying on MgO/Mo, whereas on single crystal, they are small 2D flakes standing perpendicularly to the surface. The chains can be spontaneously charged by upto 2 electrons depending on their length. The HOMO and LUMO states of the thin-film supported chains can be described with 1D harmonic oscillator potential, to which the 6s valence electrons of each atom and the extra charge transferred from the support have been confined altogether.

The larger Au clusters of ca. 7-20 atoms, have been studied on different substrate, namely on MgO(2L)/Ag. Also they become charged, by upto 3 or 4 electrons, and tend to maximize their surface contact area. The electronic states of these nearly symmetric planar clusters can be rationalized with the help of 2D harmonic oscillator model, which shows easily recognizable flower-like states. In the case of clusters, the shapes of these states are sensitive for the exact positions of the atoms as well as for the charge state of the species. Thus, in collaboration with the STM experimentalists, it has been possible to identify real clusters on MgO/Ag with the help of simulated STM and STS. This, both showed the power of combined STM/DFT study and gave further experimental proof for the quantum dot nature and charging of thin-film supported clusters.

The primary scope of the work presented in this thesis has been to characterize thin-film based cluster catalytic model systems. Although the emphasis has been more in the electronic and structural properties of the potentially catalytic systems than in the actual catalytic reactions, one step towards chemistry has been taken by modeling the  $O_2$  adsorption on  $Au_{1-6}$  on  $MgO(3L)/Mo$ . The results show that  $O_2$  adsorbs at the end of the Au chains and the adsorption is exothermic. However, adsorption on the bare thin-film terrace is slightly more favorable. In all the studied cases,  $O_2$  is charged and activated to its peroxo or superoxo-like state, which should facilitate its reactions with other molecules like CO. The diffusion barrier of  $O_2$  is low and thus it is likely that the molecules occasionally reach a cluster with pre-adsorbed CO, and the oxidation reaction can take place near the end of the cluster.

The next step would be to calculate the reaction barriers for the CO oxidation at the oxide cluster interface. Possibly, it could be wise to choose  $MgO/Ag$  substrate as on  $MgO/Mo$ , there exists a slight thermodynamic driving force separating the clusters and  $O_2$  molecule. Furthermore, it would be interesting to consider also the possibility of dissociative  $O_2$  adsorption on thin-film supported chains and the CO oxidation reaction pathways in such cases.

It is also possible that the slightly larger, flat and planar clusters have different CO oxidation abilities than the tiny chains. Indeed, in an ongoing study [124], it has been found that a planar  $Au_{14}$  can bind up to 10  $O_2$  molecules on  $MgO(2L)/Ag$  and the dissociation barrier of  $O_2$  is low. This opens entirely different possibilities for the reaction pathways than the scenario suggested in this thesis.

A third, very interesting and yet entirely unexplored, topic is the thin-film effects on nanoparticles which are larger than the sub-nanometer clusters studied in this thesis. As discussed in the introduction, experiments show that Au nanoparticles of 4-5 nm are catalytically very active. It is proposed that the activity depends on the number of under-coordinated sites, which in turn is controlled by the particle size and shape. However, it is not reasonable to model these particles of hundreds or thousands of atoms explicitly with DFT. Instead, one could estimate their shapes with Wulff construction. According to the work presented in this thesis, it is known that the adhesion energy between the oxide and the cluster is increased significantly due to the carrier metal below. This should lead to flattened particle shapes also for large clusters of several nanometers. Due to this, the cluster-oxide interface sites and the number of low-coordinated sites on the cluster edges could be different on thin films than on bulk like oxide supports. These, in turn, could have an effect on catalytic reactions in these systems. The number of low-coordinated active sites on different thin-film substrates could be estimated with Wulff constructions parametrized with DFT adhesion and surface energies.

On the other hand, boundary regimes of thin-film supported large clusters could be



modeled with periodic rods in the spirit of the work of Molina and Hammer [36, 48]. Their work deals with Au clusters on bulk like oxide surfaces only, but could be extended to thin-film surfaces. The activity of the boundary sites could be estimated with reaction barrier calculations. As the yet unpublished results [124] show that O<sub>2</sub> adsorbates can decorate the whole rim of Au<sub>14</sub> on MgO(2L)/Ag, it is likely that the boundaries of large clusters can trap quite a large amount of O<sub>2</sub>. Furthermore, as the dissociation of O<sub>2</sub> has a low barrier, it is possible that finally the cluster rims are decorated by atomic oxygen, which is likely to react easily with CO.

The work presented in this thesis has contributed to the knowledge concerning thin-film effects on adsorbates and their chemical reactions. This study has helped to characterize thin-film based cluster catalytic model systems and opened new questions related to oxidation reaction pathways in heterogeneous catalysis. It is likely that the catalysis by gold and the thin-film effects continue to be hot topics of experimental and computational studies as there still are a lot of details to be unraveled. The active development of both the hardware and software of computational surface science will guarantee that the computational modeling studies will be able to provide understanding for more and more realistic catalytic systems in the future.



# References

- [1] W.A. de Heer. *The physics of simple metal clusters: experimental aspects and simple models*. Rev. Mod. Phys. **65**, 611 (1993).
- [2] R. L. Johnston. *Atomic and molecular clusters*. Taylor Francis, USA, Canada (2002).
- [3] T. Ellis. *The future of gold in electronics*. Gold bulletin **37**, 66 (2004).
- [4] B. Yoon, P. Koskinen, B. Huber, O. Kostko, B. von Issendorff, H. Häkkinen, M. Moseler and U. Landman. *Size-dependent structural evolution and chemical reactivity of gold clusters*. Chem. Phys. Chem. **8**, 157 (2007).
- [5] K.J. Taylor, C.L. Pettiette-Hall, O. Cheshnovsky and R.E. Smalley. *Ultraviolet photoelectron spectra of coinage metal clusters*. J. Chem. Phys. **96**, 3319 (1992).
- [6] H. Häkkinen, M. Moseler and U. Landman. *Bonding in Cu, Ag, and Au clusters: Relativistic effects, trends, and surprises*. Phys. Rev. Lett. **89**, 033401 (2002).
- [7] G. J. Hutchings. *Vapor-phase hydrochlorination of acetylene - correlation of catalytic activity of supported metal chloride catalysts*. J. Catal. **96**, 292 (1985).
- [8] B. Nkosi, N. J. Coville and G. J. Hutchings. *Reactivation of a supported gold catalyst for acetylene hydrochlorination*. J. Chem. Soc., Chem. Commun. 71 (1988).
- [9] B. Nkosi, N. J. Coville, G. J. Hutchings, M. D. Adams, J. Friedl and F. Wagner. *Hydrochlorination of acetylene using gold catalysts - A study of catalyst deactivation*. J. Catal. **128**, 366 (1991).
- [10] G. J. Hutchings and M. Haruta. *A golden age of catalysis: A perspective*. Appl. Cat. A **291**, 2 (2005).
- [11] M. Haruta, T. Kobayashi, H. Sano and N. Yamada. *Novel gold catalysts for the oxidation of carbon monoxide at a temperature far below 0°C*. Chem. Lett. **16**, 405 (1987).
- [12] T. Hayashi, K. Tanaka and M. Haruta. *Selective vapor-phase epoxidation of propylene over Au/TiO<sub>2</sub> catalysts in the presence of oxygen and hydrogen*. J. Catal. **178**, 566 (1998).

- [13] A. Ueda and M. Haruta. *Nitric oxide reduction with hydrogen, carbon monoxide, and hydrocarbons over gold catalysts*. Gold Bull. **32**, 3 (1999).
- [14] M. Haruta. *Catalysis of gold nanoparticles deposited on metal oxides*. Cattech **6**, 102 (2002). See also the references therein.
- [15] A. Corma and P. Serna. *Chemoselective hydrogenation of nitro compounds with supported gold catalyst*. Science **313**, 332 (2006).
- [16] D. Andreeva. *Low temperature water gas shift over gold catalysts*. Gold Bull. **35**, 82 (2002).
- [17] L. Prati and M. Rossi. *Gold on carbon as new catalyst for selective liquid phase oxidation of diols*. J. Catal. **176**, 552 (1998).
- [18] D.M. Cox, R. Brickman, K. Creegan and A. Kaldor. *Gold clusters: reactions and deuterium uptake*. Z. Phys. D **19**, 353 (1991).
- [19] T.H. Lee and K.M. Ervin. *Reactions of copper group cluster anions with oxygen and carbon monoxide*. J. Phys. Chem. **98**, 10023 (1994).
- [20] B. E. Salisbury, W. T. Wallace and R. L. Whetten. *Low-temperature activation of molecular oxygen by gold clusters: a stoichiometric process correlated to electron affinity*. Chem. Phys. **262**, 131 (2000).
- [21] L. D. Socaciu, J. Hagen, T. M. Bernhardt, L. Wöste, U. Heiz, H. Häkkinen and U. Landman. *Catalytic CO oxidation by free Au<sub>2</sub><sup>-</sup>: Experiment and theory*. Appl. Cat. A **291**, 2 (2005).
- [22] M. Valden, X. Lai and D.W. Goodman. *Onset of catalytic activity of gold clusters on titania with the appearance of nonmetallic properties*. Science **281**, 1647 (1998).
- [23] S. Abbet, K. Judai, L. Klinger and U. Heiz. *Synthesis of monodispersed model catalysts using softlanding cluster deposition*. Pure Appl. Chem. **74**, 1527 (2002).
- [24] A. Sanchez, S. Abbet, U. Heiz, W.D. Schneider, H. Häkkinen, R.N. Barnett and U. Landman. *When gold is not noble: Nanoscale gold catalysts*. J. Phys. Chem. A **103**, 9573 (1999).
- [25] B. Yoon, H. Häkkinen, U. Landman, A.S. Worz, J.M. Antonietti, S. Abbet, K. Judai and U. Heiz. *Charging effects on bonding and catalyzed oxidation of CO on Au<sub>8</sub> clusters on MgO*. Science **307**, 403 (2005).
- [26] H. Häkkinen, S. Abbet, A. Sanchez, U. Heiz and U. Landman. *Structural, electronic, and impurity-doping effects in nanoscale chemistry: Supported gold nanoclusters*. Angew. Chem. Int. Ed. **42**, 1297 (2003).

- [27] M. S. Chen and D. W. Goodman. *Structure-activity relationships in supported Au catalysts*. Cat. Today **111**, 22 (2006).
- [28] H. Häkkinen and U. Landman. *Gas-phase catalytic oxidation of CO by Au<sub>2</sub><sup>-</sup>*. J. Am. Chem. Soc. **123**, 9704 (2001).
- [29] G. Mills, M. S. Gordon and H. Metiu. *The adsorption of molecular oxygen on neutral and negative Au<sub>n</sub> clusters (n=2-5)*. Chem. Phys. Lett. **359**, 493 (2002).
- [30] A. Franceschetti, S. J. Pennycook and S. T. Pantelides. *Oxygen chemisorption on Au nanoparticles*. Chem. Phys. Lett. **374**, 471 (2003).
- [31] B. Yoon, H. Häkkinen and U. Landman. *Interaction of O<sub>2</sub> with gold clusters: Molecular and dissociative adsorption*. J. Phys. Chem. A **107**, 4066 (2003).
- [32] B. Hvolbæk, T. V. W. Janssens, B. S. Clausen, H. Falsig, C. H. Christensen and J. K. Nørskov. *Catalytic activity of Au nanoparticles*. Nano Today **2**, 14 (2007).
- [33] N. Lopez, T. V. W. Janssens, B. S. Clausen, Y. Xu, M. Mavrikakis, T. Bligaard and J.K. Nørskov. *On the origin of the catalytic activity of gold nanoparticles for low-temperature CO oxidation*. J. Cat. **223**, 232 (2004).
- [34] I. N. Remediakis, N. Lopez and J.K. Nørskov. *CO oxidation on gold nanoparticles: Theoretical studies*. Appl. Cat. A **291**, 13 (2005).
- [35] H. Falsig, B. Hvolbæk, I. S. Kristensen, T. Jiang, T. Bligaard, C. H. Christensen and J.K. Nørskov. *Trends in the catalytic CO oxidation activity of nanoparticles*. Angew. Chem. Int. Ed. **47**, 4835 (2008).
- [36] L.M. Molina and B. Hammer. *Some recent theoretical advances in the understanding of the catalytic activity of Au*. Appl. Cat. A **291**, 21 (2005).
- [37] S. Chrétien, S. K. Buratto and H. Metieu. *Catalysis by very small Au clusters*. Cur. Op. in Sol. State Mat. Sci. **11**, 62 (2007).
- [38] M. Mavrikakis, P. Stolze and J.K. Nørskov. *Making gold less noble*. Catal. Lett. **64**, 101 (2000).
- [39] M. M. Schubert, S. Hackenberg, A. C. van Veen, M. Muhler, V. Plzak and R. J. Behm. *CO oxidation over supported gold catalysts- "inert" and "active" support materials and their role for the oxygen supply during reaction*. J. Catal. **197**, 113 (2001).
- [40] A.M. Stoneham and P.W. Tasker. *Image charges and their influence on the growth and nature of thin oxide films*. Phil. Mag. B **55**, 237 (1987).
- [41] G. Pacchioni, L. Giordano and M. Baistrocchi. *Charging of metal atoms on ultrathin MgO/Mo films*. Phys. Rev. Lett. **94**, 226104 (2005).

- [42] L. Giordano, M. Baistrocchi and G. Pacchioni. *Bonding of Pd, Ag, and Au atoms on MgO(100) surfaces and MgO/Mo(100) ultra-thin films: A comparative DFT study*. Phys. Rev. B **72**, 115403 (2005).
- [43] H. Grönbeck. *Mechanism for NO<sub>2</sub> charging on metal supported MgO*. J. Phys. Chem. B **110**, 11977 (2006).
- [44] K. Honkala and H. Häkkinen. *Au adsorption on regular and defected thin MgO(100) films supported by Mo*. J. Phys. Chem. C **111**, 4319 (2007).
- [45] I. Yudanov, G. Pacchioni, K. Neyman and N. Rösch. *Systematic density functional study of the adsorption of transition metal atoms on the MgO(001) surface*. J. Phys. Chem. B **101**, 2786 (1997).
- [46] Z. Yang, R. Wu, Q. Zhang and D. W. Goodman. *Adsorption of Au on an O-deficient MgO(001) surface*. Phys. Rev. B **65**, 155407 (2002).
- [47] A. Bogicevic and D.R. Jennison. *Effect of oxide vacancies on metal island nucleation*. Surf. Sci. **515**, L481 (2002).
- [48] L.M. Molina and B. Hammer. *Theoretical study of CO oxidation on Au nanoparticles supported by MgO(100)*. Phys. Rev. B **69**, 155424 (2004).
- [49] A. Del Vitto, G. Pacchioni, F. Delbecq and P. Sautet. *Au atoms and dimers on the MgO(100) surface: A DFT study of nucleation at defects*. J. Phys. Chem. B **109**, 8040 (2005).
- [50] R. Coquet, G. J. Hutchings, S. H. Taylor and D. J. Willock. *Calculations on the adsorption of Au to MgO surfaces using SIESTA*. J. Mater. Chem. **16**, 1978 (2006).
- [51] G. Barcaro and A. Fortunelli. *Structure and diffusion of small Ag and Au clusters on the regular MgO (100) surface*. New J. Phys. **9**, 22 (2007).
- [52] M. Sterrer, T. Risse, M. Heyde, H.P. Rust and H.J. Freund. *Crossover from three-dimensional to two-dimensional geometries of Au nanostructures on thin MgO(001) films: a conformation of theoretical predictions*. Phys. Rev. Lett. **98**, 206103 (2007).
- [53] M. Sterrer, T. Risse, U. Martinez, L. Giordano, M. Heyde, H.P. Rust, G. Pacchioni and H.J. Freund. *Control of the charge state of metal atoms on thin MgO films*. Phys. Rev. Lett. **98**, 096107 (2007).
- [54] F. Cinquini, L. Giordano and G. Pacchioni. *Adsorption of transition metal atoms on the NiO(100) surface and on NiO/Ag(100) thin films*. Theor. Chem. Acc. **120**, 575 (2008).

- [55] U. Martinez, L. Giordano and G. Pacchioni. *Tuning the work function of ultrathin oxide films on metals by adsorption of alkali atoms*. J. Chem. Phys. **128**, 164707 (2008).
- [56] P. Broqvist and H. Grönbeck. *Effect of the metal in NO<sub>2</sub> adsorption on platinum supported BaO*. Surf. Sci. **600**, L214 (2006).
- [57] S. Siculo, L. Giordano and G. Pacchioni. *CO adsorption on one-, two-, and three-dimensional Au clusters supported on MgO/Ag(001) ultrathin films*. J. Phys. Chem. C **113**, 10256 (2009).
- [58] D. Ricci, A. Bongiorno, G. Pacchioni and U. Landman. *Bonding trends and dimensionality crossover of gold nanoclusters on metal-supported MgO thin films*. Phys. Rev. Lett. **97**, 036106 (2006).
- [59] N. Nilius, M. V. Ganduglia-Pirovano, V. Brázdrová, M. Kulawik, J. Sauer and H.-J. Freund. *Counting electrons transferred through a thin alumina film into Au chains*. Phys. Rev. Lett. **100**, 096802 (2008).
- [60] V. Simic-Milosevic, M. Heyde, X. Lin, T. König, H.-P. Rust, M. Sterrer, T. Risse, N. Nilius, H.-J. Freund, L. Giordano and G. Pacchioni. *Charge-induced formation of linear Au clusters on thin MgO films: Scanning tunneling microscopy and density-functional theory study*. Phys. Rev. B **78**, 235429 (2008).
- [61] A. Hellman and H. Grönbeck. *Activation of Al<sub>2</sub>O<sub>3</sub> by a long-ranged chemical bond mechanism*. Phys. Rev. Lett. **100**, 116801 (2008).
- [62] M. Baron, D. Stacchiola, S. Ulrich, N. Nilius, S. Shaikhutdinov, H. J. Freund, U. Martinez, L. Giordano and G. Pacchioni. *Adsorption of Au and Pd atoms on thin SiO<sub>2</sub> films: The role of atomic structure*. J. Phys. Chem. C **112**, 3405 (2008).
- [63] S. Ulrich, N. Nilius, H. J. Freund, U. Martinez, L. Giordano and G. Pacchioni. *Evidence for a size-selective adsorption mechanism on oxide surfaces: Pd and Au atoms on SiO<sub>2</sub>/Mo(112)*. Chem. Phys. Chem. **9**, 1367 (2008).
- [64] L. Giordano, G. Pacchioni, J. Goniakowski, N. Nilius, E. D. L. Rienks and H. J. Freund. *Charging of metal adatoms on ultrathin oxide films: Au and Pd on FeO/Pt(111)*. Phys. Rev. Lett. **101**, 026102 (2008).
- [65] S. Prada, U. Martinez and G. Pacchioni. *Work function changes induced by deposition of ultrathin dielectric films on metals: A theoretical analysis*. Phys. Rev. B **78**, 235423 (2008).
- [66] U. Martinez, G. Pacchioni and F. Illas. *Enhanced magnetic moments of Fe clusters supported on MgO/Fe(001) ultrathin films*. J. Chem. Phys. **130**, 184711 (2009).

- 
- [67] G. Binnig and H. Rohrer. *Surface studies by scanning tunneling microscopy*. Phys. Rev. Lett. **49**, 57 (1982).
- [68] G. Binnig and H. Rohrer. *Scanning tunneling microscopy - from birth to adolescence (Nobel lecture)*. Angew. Chem. Int. Ed. **26**, 606 (1987).
- [69] P. Hohenberg and W. Kohn. *Inhomogeneous electron gas*. Phys. Rev. **136**, 864 (1964).
- [70] W. Kohn and L.J. Sham. *Self-consistent equations including exchange and correlation effects*. Phys. Rev. **140**, 1133 (1965).
- [71] W. Kohn. *Nobel lecture: Electronic structure of matter - Wave functions and density functionals*. Rev. Mod. Phys. **71**, 1253 (1999).
- [72] J. Repp, G. Meyer, F.E. Olsson and M. Persson. *Controlling the charge state of individual gold adatoms*. Science **305**, 493 (2004).
- [73] J. Repp, G. Meyer, S. Paavilainen, F. E. Olsson and M. Persson. *Imaging bond formation between a gold atom and pentacene on an insulating surface*. Science **312**, 1196 (2006).
- [74] F. E. Olsson, S. Paavilainen, M. Persson, J. Repp and G. Meyer. *Multiple charge states of Ag atoms on ultrathin NaCl films*. Phys. Rev. Lett. **98**, 176803 (2007).
- [75] [Http://dcwww.camd.dtu.dk/campos/Dacapo/](http://dcwww.camd.dtu.dk/campos/Dacapo/).
- [76] J. J. Mortensen, L. B. Hansen and K. W. Jacobsen. *Real-space grid implementation of the projector augmented wave method*. Phys. Rev. B **71**, 035109 (2005). [Https://wiki.fysik.dtu.dk/gpaw/](https://wiki.fysik.dtu.dk/gpaw/).
- [77] A. L. Fetter. *Quantum theory of many-particle systems*. Dover publications inc., Mineola, New York, USA (2003).
- [78] R. M. Martin. *Electronic structure - Basic theory and practical methods*. Cambridge university press, UK (2004).
- [79] R. G. Parr and W. Yang. *Density-functional theory of atoms and molecules*. Oxford university press, New York, USA (1989).
- [80] W. Koch and M. C. Holthausen. *A chemist's guide to density functional theory*. Wiley, Weinheim, Germany (2002).
- [81] R.O. Jones and O. Gunnarsson. *The density functional formalism, its applications and prospects*. Rev. Mod. Phys. **61**, 689 (1989).



- 
- [82] M.C. Payne, M.P. Teter, D.C. Allan, T.A. Arias and J.D. Joannopoulos. *Iterative minimization techniques for abinitio total-energy calculations - Molecular-dynamics and conjugate gradients*. Rev. of Mod. Phys. **64**, 1045 (1992).
- [83] E. J. Baerends and O. V. Gritsenko. *A quantum chemical view of density functional theory*. J. Phys. Chem. A **101**, 5383 (1997).
- [84] J.P. Perdew and S. Kurth. *Density functionals for non-relativistic coulomb systems*. Lect. Notes in Phys., Springer, Germany **500**, 8 (1998).
- [85] U. von Barth. *Basic density-functional theory - an overview*. Physica Scripta **109**, 9 (2004).
- [86] R. van Leeuwen. *Density functional theory and its applications in nanoscience*. Lecture notes, University of Jyväskylä (2008).
- [87] J. Pople. *Nobel lecture: Quantum chemical models*. Rev. Mod. Phys. **71**, 1267 (1999).
- [88] L. Hedin and B. Lundqvist. *Explicit local exchange-correlation potentials*. J. Phys. C **4**, 2064 (1971).
- [89] S.H. Vosko, L. Wilk and M. Nusair. *Accurate spin-dependent electron liquid correlation energies for local spin-density calculations - A critical analysis*. Can. J. Phys. **58**, 1200 (1980).
- [90] J.P. Perdew and A. Zunger. *Self-interaction correction to density-functional approximations for many-electron systems*. Phys. Rev. B **23**, 5048 (1981).
- [91] O. Gunnarsson, M. Jonson and B.I. Lundqvist. *Descriptions of exchange and correlation effects in inhomogenous electron-systems*. Phys. Rev. B **20**, 3136 (1979).
- [92] S. Kurth, J. P. Perdew and P. Blaha. *Molecular and solid-state tests of density functional approximations: LSD, GGAs, and meta-GGAs*. Int. J. of. Q. Chem. **75**, 889 (1999).
- [93] B. Hammer, L. B. Hansen and J. K. Nørskov. *Improved adsorption energetics within density-functional theory using revised Perdew-Burke-Ernzerhof functionals*. Phys. Rev. B. **59**, 7413 (1999).
- [94] K. Burke, J.P. Perdew and Y. Wang. *Derivation of a generalized gradient approximation: The PW91 density functional*. Electronic density functional theory: recent progress and new directions, Plenum, NY 81 (1997).

- 
- [95] J. P. Perdew, J. A. Chevary, S. H. Vosko, K. A. Jackson, M. R. Pederson, D. J. Singh and C. Fiolhais. *Atoms, molecules, solids, and surfaces: Applications of the generalized gradient approximation for exchange and correlation*. Phys. Rev. B **46**, 6671 (1992).
- [96] J.P. Perdew, K. Burke and M. Ernzerhof. *Generalized gradient approximation made simple*. Phys. Rev. Lett. **77**, 3865 (1996).
- [97] Y. Zhang and W. Yang. *Comment on "Generalized gradient approximation made simple"*. Phys. Rev. Lett. **80**, 890 (1998).
- [98] E.H. Lieb and S. Oxford. *Improved lower bound on the indirect coulomb energy*. Int. J. of Quantum Chem. **19**, 427 (1981).
- [99] G.K.-L. Chan and N.C. Handy. *Optimized Lieb-Oxford bound for the exchange-correlation energy*. Phys. Rev. A **59**, 3075 (1999).
- [100] M.M. Odashima and K. Capelle. *Empirical analysis of the Lieb-Oxford bound in ions and molecules*. Int. J. of Quantum Chem. **108**, 2428 (2008).
- [101] R. W. G. Wyckoff. *Crystal structures*. John Wiley and Sons, New York, USA (1963).
- [102] H. J. Monkhorst and J. D. Pack. *Special points for Brillouin-zone integrations*. Phys. Rev. B **13**, 5188 (1976).
- [103] T. L. Beck. *Real-space mesh techniques in density-functional theory*. Rev. Mod. Phys. **72**, 1041 (2008).
- [104] D. Vanderbilt. *Soft self-consistent pseudopotentials in a generalized eigenvalue formalism*. Phys. Rev. B **41**, 7892 (1990).
- [105] G. Kresse and D. Joubert. *From ultrasoft pseudopotentials to the projector augmented-wave method*. Phys. Rev. B **59**, 1758 (1999).
- [106] N. Troullier and J. L. Martins. *Efficient pseudopotentials for plane wave calculations*. Phys. Rev. B **43**, 1993 (1991).
- [107] P. E. Blöchl. *Projector augmented-wave method*. Phys. Rev. B **50**, 17953 (1994).
- [108] P. E. Blöchl, C. J. Först and J. Schimpl. *Projector augmented wave method: ab-initio molecular dynamics with full wave functions*. Bull. Mat. Sci. **26**, 33 (2003).
- [109] C. Rostgaard. *Projector augmented wave method*. Available at [https://wiki.fysik.dtu.dk/gpaw/paw\\_note.pdf](https://wiki.fysik.dtu.dk/gpaw/paw_note.pdf), 29.9.2009 .

- 
- [110] R. Stowasser and R. Hoffman. *What do the Kohn-Sham orbitals and eigenvalues mean?* J. Am. Chem. Soc. **121**, 3414 (1999).
- [111] T. Kar and J. G. Ángyán. *Comparison of ab initio Hartree-Fock and Kohn-Sham orbitals in the calculation of atomic charge, bond index and valence.* J. Phys. Chem. A **104**, 9953 (2000).
- [112] G. Zhang and C. B. Musgrave. *Comparison of DFT methods for molecular orbital eigenvalue calculations.* J. Phys. Chem. A **111**, 1554 (2007).
- [113] G. Henkelman, A. Arnaldsson and H. Jónsson. *A fast and robust algorithm for Bader decomposition of charge density.* Comput. Mater. Sci. **36**, 354 (2006).
- [114] E. Sanville, S. D. Kenny, R. Smith and G. Henkelman. *An improved grid-based algorithm for Bader charge allocation.* J. Comp. Chem. **28**, 899 (2007).
- [115] W. Tang, E. Sanville and G. Henkelman. *A grid-based Bader analysis algorithm without lattice bias.* J. Phys.: Compute Mater. **21**, 084204 (2009).
- [116] J. Tersoff and D. R. Hamann. *Theory and application for the scanning tunneling microscope.* Phys. Rev. Lett. **50**, 1998 (1983).
- [117] J. Tersoff and D. R. Hamann. *Theory of the scanning tunneling microscope.* Phys. Rev. B **31**, 805 (1985).
- [118] W. A. Hofer, A. S. Foster and A. L. Shluger. *Theories of scanning probe microscopes at the atomic scale.* Rev. Mod. Phys. **75**, 1287 (2003).
- [119] C. J. Chen. *Introduction to scanning tunneling microscopy.* Oxford university press, UK, USA (1993).
- [120] J. Bardeen. *Tunneling from a many-particle point of view.* Phys. Rev. Lett. **6**, 57 (1961).
- [121] L. Giordano, U. Martinez, S. Siculo and G. Pacchioni. *Observable consequences of formation of Au anions from deposition of Au atoms on ultrathin oxide films.* J. Chem. Phys. **127**, 144713 (2007).
- [122] A. Bondi. *Van der Waals volumes + radii.* J. Phys. Chem. **68**, 441 (1965).
- [123] L.M. Molina and B. Hammer. *Oxygen adsorption at anionic free and supported Au clusters.* J. Chem. Phys. **123**, 161104 (2005).
- [124] P. Frondelius, H. Häkkinen and K. Honkala. *Paper under preparation.*